

# **NASA CONTRACTOR REPORT 175060**

(NASA-CR-175060) ON 3-D INELASTIC ANALYSIS  
METHODS FOR HOT SECTION COMPONENTS (BASE  
PROGRAM) Annual Status Report (Pratt and  
Whitney Aircraft) 206 p CSCL 29K

N87-12923

Unclas  
G6/39 44657

## **3-D INELASTIC ANALYSIS METHODS FOR HOT SECTION COMPONENTS (BASE PROGRAM)**

**Second Annual Status Report  
For the Period  
February 14, 1984 to February 14, 1985**

**R.B. Wilson, M.J. Bak,  
S. Nakazawa, and P.K. Banerjee**

**Contract NAS3-23697  
February 1986**

**NASA**

**NASA CONTRACTOR REPORT 175060**

**3-D INELASTIC ANALYSIS METHODS  
FOR HOT SECTION COMPONENTS  
(BASE PROGRAM)**

✓  
**Second Annual Status Report**

**R.B. Wilson, M.J. Bak,  
S. Nakazawa, and P.K. Banerjee**

**Prepared for  
NASA - Lewis Research Center  
Under Contract NAS3-23697**

**NASA**

1. REPORT NO. NASA CR-175060	2. GOVERNMENT AGENCY	3. RECIPIENT'S CATALOG NO.	
4. TITLE AND SUBTITLE 3-D INELASTIC ANALYSIS METHODS FOR HOT SECTION COMPONENTS (BASE PROGRAM)		5. REPORT DATE February 1986	6. PERFORMING ORG. CODE
7. AUTHOR(S) R. B. Wilson, M. J. Bak, S. Nakazawa and P. K. Banerjee		8. PERFORMING ORG. REPT. NO. PWA-5940-36	
9. PERFORMING ORG. NAME AND ADDRESS UNITED TECHNOLOGIES CORPORATION Pratt & Whitney, Engineering Division 400 Main St., East Hartford, CT 06108		10. WORK UNIT NO.	11. CONTRACT OR GRANT NO. NAS3-23697
12. SPONSORING AGENCY NAME AND ADDRESS National Aeronautics and Space Administration Lewis Research Center Project Manager, C. C. Chamis, MS 49-6 21000 Brookpark Road, Cleveland, OH 44135		13. TYPE REPT./PERIOD COVERED Second Annual Status Report	
15. SUPPLEMENTARY NOTES		14. SPONSORING AGENCY CODE RTOP 533-04-1A	
16. ABSTRACT A 3-D Inelastic Analysis Methods program is described. This program consists of a series of new computer codes embodying a progression of mathematical models (mechanics of materials, special finite element, boundary element) for streamlined analysis of: (1) combustor liners, (2) turbine blades, and (3) turbine vanes. These models address the effects of high temperatures and thermal/mechanical loadings on the local (stress/strain) and global (dynamics, buckling) structural behavior of the three selected components. Three computer codes, referred to as MOMM (Mechanics of Materials Model), MHOST (MARC-Hot Section Technology), and BEST (Boundary Element Stress Technology), have been developed and are briefly described in this report.			
17. KEY WORDS (SUGGESTED BY AUTHOR(S)) 3-D Inelastic Analysis, Finite Elements, Boundary Elements, High Temperature, Creep, Vibration, Buckling, Solution Methods, Constitutive Modeling		18. DISTRIBUTION STATEMENT Unclassified Unlimited	
19. SECURITY CLASS THIS (REPT) Unclassified	20. SECURITY CLASS THIS (PAGE) Unclassified	21. NO. PGS 194	22. PRICE *

\* For sale by the National Technical Information Service, Springfield, VA 22161

## PREFACE

This Second Annual Status Report describes the results of work performed during the first two years of the NASA Hot Section Technology program, "3-D Inelastic Analysis Methods for Hot Section Components" (contract NAS3-23697). The goal of the program is to develop computer codes which permit more accurate and efficient structural analyses of gas turbine blades, vanes, and combustor liners. The program is being conducted under the direction of Dr. C. C. Chamis of the NASA-Lewis Research Center. Prime contractor activities at United Technologies Corporation are managed by Dr. E. S. Todd. Subcontractor efforts at the United Technologies Research Center, MARC Analysis Research Corporation, and the State University of New York at Buffalo are led by Dr. B. N. Cassenti, Dr. J. C. Nagtegaal, and Dr. P. K. Banerjee, respectively.

## Table of Contents

<u>Section</u>	<u>Page</u>
1.0 INTRODUCTION	1
2.0 SUMMARY	4
2.1 Constitutive Models	4
2.2 Mechanics of Materials Model	5
2.3 Special Finite Element Model	5
2.4 Advanced Formulation (Boundary Element) Model	6
3.0 TECHNICAL PROGRESS	7
3.1 Constitutive Models	7
3.1.1 Simplified Secant Elastic Model	7
3.1.2 Current State-of-the-Art Model	11
3.1.3 Advanced Viscoplastic Model	20
3.1.4 List of Symbols	24
3.1.5 References	26
3.2 Mechanics of Materials Model	27
3.2.1 Computer Program: Formulation/Description	27
3.2.2 Program Validation/Verification	35
3.2.3 List of Symbols	43
3.2.4 Problems That Can Be Solved Using MOMEM	44
3.3 Special Finite Element Model	45
3.3.1 Summary	45
3.3.2 Introduction	45
3.3.3 Literature Survey	46
3.3.4 Formulation Strategy and Development	51
3.3.4.1 The Global Solution Strategy	51
3.3.4.2 Incremental Iterative Solution Algorithms	56
3.3.4.3 Construction of the Stiffness Equations	62
3.3.4.4 Time Integration Algorithm	68
3.3.4.5 Eigenvalue Extraction for Modal and Buckling Analysis	72
3.3.4.6 Subelement Iterations	72
3.3.5 Computer Program Development	82
3.3.5.1 Solution Capabilities	82
3.3.5.2 Data Storage and Control Structure	92
3.3.6 Validation/Verification Analyses	94
3.3.6.1 Analysis of Plate and Shell Structures	94
3.3.6.2 Analyses with Subelement Iterations	105
3.3.7 Three-Dimensional Solid Element Analyses	113
3.3.8 List of Symbols	120
3.3.9 References	124

## Table of Contents (continued)

<u>Section</u>	<u>Page</u>
3.4 Boundary Element Method	128
3.4.1 Overview	128
3.4.2 Literature Survey Update	130
3.4.3 Formulation Development	130
3.4.3.1 Summary	130
3.4.3.2 Linear and Nonlinear Stress Analysis	131
3.4.3.2.1 Review	131
3.4.3.2.2 Redefinition of Plasticity Formulation	132
3.4.3.2.3 Plasticity Solution Sequence	133
3.4.3.2.4 Inelastic Material Models	137
3.4.3.2.5 Multi-GMR Plasticity Algorithm	139
3.4.3.2.6 Embedded Hot Spots and Discontinuities	139
3.4.3.2.7 Anisotropic Elastic Materials	141
3.4.3.3 Transient and Dynamic Stress Analysis	144
3.4.3.3.1 Review	144
3.4.3.3.2 Calculations of Natural Frequencies and Mode Shapes	146
3.4.3.3.3 Time Embedded Transient Dynamic Formulation	148
3.4.4 Computer Program Development	150
3.4.4.1 Introduction	150
3.4.4.2 Global Program Structure	151
3.4.4.3 Program Input	152
3.4.4.4 Surface Integral Calculation	154
3.4.4.4.1 Integration in the Static Case	154
3.4.4.4.2 Surface Integration in the Transient Algorithm	156
3.4.4.5 Volume Integrals	157
3.4.4.6 System Matrix Assembly for Multiregion Plasticity	157
3.4.4.7 System Equation Solution	158
3.4.4.8 Inelastic Solution Process for a Multi-GMR Problem	158
3.4.5 Validation/Verification	158
3.4.5.1 Summary	158
3.4.5.2 Validation of Elastic Capabilities	159
3.4.5.3 Multi-region Nonlinear Analysis	162
3.4.5.4 Application of Exact Initial Strain Solution	167
3.4.5.5 Embedded Time Dynamic Analysis	169
3.4.5.6 Calculation of Natural Frequencies and Mode Shapes	173
3.4.5.7 Inelastic Analysis of the Benchmark Notch Specimen	175
3.4.5.8 Component Analysis	179
3.4.6 List of Symbols	182
3.4.7 References	184
Distribution List	185

## List of Illustrations

<u>Figure Number</u>	<u>Title</u>	<u>Page</u>
3.1-1	Variation in Nu	10
3.1-2	Three Bar Convergence Using Simplified Model	11
3.1-3	Elastic-Plastic Strain Decompositions for Bilinear Stress-Strain Law	14
3.1-4	Elastic-Plastic Iteration Procedure	17
3.1-5	Creep Iteration Procedure	19
3.1-6	Modified Walker's Theory	21
3.2-1	3-D Inelastic Mechanics of Materials Computer Program Flow Chart	28
3.2-2	Schematic of TEST1 Beam	36
3.2-3	Square Plate Approximation Centrally Loaded	37
3.2-4	Schematic of TEST3	38
3.2-5	Stress-Strain Response for TEST3	38
3.2-6	Schematic of TEST4 and TEST5	39
3.2-7	Displacement History for TEST4 and TEST5	39
3.2-8	Schematic of Crack Simulation in Beam	40
3.2-9	Schematic of TEST6 Beam	41
3.2-10	Schematic of TEST7 Beam	42
3.3-1	The Arc-Length Method for the Mixed Iterative Solution	60
3.3-2	The Inverse BFGS Update for the Mixed Iterative Solution	61
3.3-3	Local-Global Representation of an Embedded Singularity	75
3.3-4	Multiple Isoparametric Mapping for an Element with an Embedded Hole	78
3.3-5	Clamped Square Plate	95

## List of Illustrations

<u>Figure Number</u>	<u>Title</u>	<u>Page</u>
3.3-6	Corner Supported Plate with Central Concentrated Load	96
3.3-7	Lateral Displacement with Hourglass Control	96
3.3-8	Lateral Displacement without Hourglass Control	97
3.3-9	Simplified Vane Model	98
3.3-10	Convergence of Residual Forces	100
3.3-11	Model and Dynamic Loads for Pinned Beam	101
3.3-12	Pinned Beam: Mid-Span Deflection	102
3.3-13	Models of Lindberg and Olson Fan Blade	103
3.3-14	Comparisons Between MHOST and Experimental Mode Shapes	104
3.3-15	Cantilever Beam Validation Problem	105
3.3-16	Problem Statement for Plane Stress Deformation of a Domain with a Singularity to Prescribed Displacement	107
3.3-17	Stress Distribution ( $\sigma_x$ ) for L-Shape Domain with Continuous Stress Field	108
3.3-18	Distribution of $\sigma_x$ , $\tau_{xy}$ , and Equivalent Stress Along Line Connecting Nodes 21 and 45	109
3.3-19	Distribution of $\sigma_x$ , $\tau_{xy}$ , and Equivalent Stress Along Line Connecting Nodes 5 and 65	109
3.3-20	Stress Distribution ( $\sigma_x$ ) for L-Shape Domain with Discontinuous Stress Field	110
3.3-21	Stress Distribution ( $\sigma_x$ ) for L-Shape Domain with Discontinuous Stress Field and Subelement Mesh	110
3.3-22	Finite Element Model of a Plate with a Circular Hole	111
3.3-23	Deformation After One Increment	112
3.3-24	Burner Blister Specimen Model In-Plane General Breakup (Three-Dimensional)	114
3.3-25	Burner Blister Specimen Model In-Plane Local Vertex-Neighborhood Breakup (Three-Dimensional)	114

## List of Illustrations

<u>Figure Number</u>	<u>Title</u>	<u>Page</u>
3.3-26	Hot Spot Temperature Distribution (Mid-Plane) for Burner Blister Specimen Model	115
3.3-27	Axisymmetric Burner Blister Model for MARC-Breakup Near Vertex	116
3.3-28	Mises Plastic Strain at Mid-Plane Vertex Node	117
3.3-29	Computer Running Times for 100 Percent Load in One Step (Three-Dimensional Model)	119
3.4-1	Plasticity Solution Sequence	136
3.4-2	BEST3D - Overall Program Structure	153
3.4-3	Subdivision Strategy for Nonsingular Surface Integration	156
3.4-4	Test Geometry for Surface Integration Algorithm	160
3.4-5	Solution Error Vs. Integration Tolerance	161
3.4-6	Computational Effort Vs. Integration Tolerance	162
3.4-7	BEST3D Models for Thick Cylinder	163
3.4-8	Normalized Radial Expansion at Outer Radius of Cylinder	164
3.4-9	Radial Variation of Hoop Stress in Thick Cylinder	164
3.4-10	BEST3D Models for Inelastic Analysis of Disk	165
3.4-11	Load - Deflection Response for Disk	166
3.4-12	Elastic Hoop Stress Vs. Radius	167
3.4-13	Constant Thickness Plate with Through Thickness Slot	168
3.4-14	Stress Variation in Plate with Slot	169
3.4-15	BEST3D Models for Spherical Cavity	170
3.4-16	Explosion in Spherical Cavity - Mesh 1	171
3.4-17	Explosion in Spherical Cavity - Dynamic Magnification	171

## List of Illustrations

<u>Figure Number</u>	<u>Title</u>	<u>Page</u>
3.4-18	Explosion in Spherical Cavity - Mesh 3	172
3.4-19	Comparison of Finite Element and Boundary Element Mode Shapes	174
3.4-20	Double Edge Notch Specimen Used in Contract NAS3-22522	176
3.4-21	Boundary Element Models for Benchmark Notch Analysis	177
3.4-22	Finite Element Models for Benchmark Notch Analysis	177
3.4-23	Benchmark Notch - BEST3D Vs. Measured Strains	178
3.4-24	Benchmark Notch - MHOST Vs. Measured Strains	178
3.4-25	Benchmark Notch - First Cycle Response	179
3.4-26	BEST3D Model of Cooled High-Pressure Turbine Blade	180
3.4-27	Extent of Quadratic Variation Used in BEST3D Turbine Blade Analysis	181

## List of Tables

<u>Table Number</u>	<u>Title</u>	<u>Page</u>
3.3-I	MHOST Analysis Capability: Element Definition Options	83
3.3-II	MHOST Analysis Capability: Analysis Module Options	83
3.3-III	MHOST Code, Version 2.0; Elements and Parameters	91
3.3-IV	Displacements for Constant Thickness Vane Model	99
3.3-V	Displacements for Variable Thickness Vane Model	100
3.3-VI	Frequencies for Lindberg and Olson Fan Blade	104
3.3-VII	Central Processing Unit (CPU) Time for the Beam Validation Problem	106
3.3-VIII	Parameters for the Validation Model of a Hole in Finite Plate	112
3.3-IX	Solution at Point A by the Global and Subelement Iterations After Increment One, Total Load $F = 1.1 F_0$	113
3.3-X	Out-of-Plane Displacement at Mid-Plane Vertex Node for 100 Percent Loading	117

## SECTION 1.0

### INTRODUCTION

Aircraft powerplant fuel consumption and expenditures for repair/replacement of worn or damaged parts make up a significant portion of commercial aviation's direct operating costs. For modern gas turbines, both factors depend heavily on the degree to which elevated flowpath temperatures are sustained in the hot section modules of the engine. Higher temperatures reduce fuel consumption by raising the basic efficiency of the gas generator thermodynamic cycle. At the same time, these elevated temperatures work to degrade the durability of structural components (combustor liners, turbine blades and vanes, airseals, etc.) that must function adjacent to or within the hot gaspath itself, leading in turn to larger maintenance/material costs. Pursuit of the best compromise between performance and durability presents a challenge that will continue to tax the ingenuity of advanced gas turbine design analysts for years to come.

Hot section durability problems appear in a variety of forms, ranging from oxidation/corrosion, erosion, and distortion (creep deformations) to occurrence of fatigue cracking. Even modest changes in shape, from erosion or distortion of airfoils for example, can lead to measurable performance deterioration that must be accurately predicted during propulsion system design to insure that long-term efficiency guarantees can be met. Larger distortions introduce serious problems such as hot spots and profile shifts resulting from diversion of cooling air, high vibratory stresses associated with loose turbine blade shrouds, difficult disassembly/reassembly of mating parts at overhaul, etc. These problems must be considered and efforts made to eliminate their effects during the engine design/development process. Initiation and propagation of fatigue cracks represents a direct threat to component structural integrity and must be thoroughly understood and accurately predicted to insure continued safe and efficient engine operation.

Accurate prediction of component fatigue lives is strongly dependent on the success with which inelastic stress/strain states in the vicinity of holes, fillets, welds, and other discontinuities can be calculated. Stress/strain computations for hot section components are made particularly difficult by two factors - the high degree of geometrical irregularity which accompanies sophisticated cooling schemes, and complex nonlinear material behavior associated with high temperature creep/plasticity effects. Since cooling air extraction reduces engine cycle efficiency, concerted efforts are made to minimize its use with the result that elaborate internal passages and surface ports are employed to selectively bathe local regions (airfoil leading edges, louver liner lips, etc.) for which the high temperature environment is most severe. These cooling features frequently interrupt load paths and introduce complex temperature gradients to the extent that the basic assumptions of one- and two-dimensional stress analysis procedures are seriously compromised and the use of three-dimensional techniques becomes mandatory. Even in the presence of cooling, component temperature and stress levels remain high relative to the material's melting point and yield strength values. The combinations of centrifugal, aerodynamic, thermal, and other mechanical loadings that typically occur in flight operation then serve to drive the underlying material response beyond accepted limits for linear elastic behavior and into the regime characterized by inelastic, time-dependent structural deformations. Thus, an ability to account for both complexities, three-dimensional and inelastic effects, becomes essential to the design of durable hot section components.

General purpose finite element computer codes containing a variety of three-dimensional (brick) elements and inelastic material models have been available for more than a decade. Incorporation of such codes into the hot section design process has been severely limited by high costs associated with the extensive labor/computer/time resources required to obtain reasonably detailed results. Geometric modeling systems and automated input/output data processing packages have received first attention from software developers in recent years and will soon mature to the point that previous over-riding manpower concerns will be alleviated. Prohibitive amounts of Central Processing Unit (CPU) time are still required for execution of even modest-size three-dimensional inelastic stress analyses, however, and is chief among the obstacles

remaining to be remedied. With today's computers and solution algorithms, models described by a few hundred displacement degrees of freedom commonly consume one to three hours of mainframe CPU time during simulation of a single thermomechanical loading cycle. A sequence of many such cycles may, of course, be needed to reach the stabilized conditions of interest. Since accurate idealizations of components with only a few geometrical discontinuities can easily contain several thousand degrees of freedom, inelastic analysis of hot section hardware with existing codes falls outside the realm of practicality.

The Inelastic Methods Program addresses the need to develop more efficient and accurate three-dimensional inelastic structural analysis procedures for gas turbine hot section components. A series of new, increasingly rigorous, stand-alone computer codes is being created for the comprehensive numerical analysis of combustor liners, turbine blades and vanes. Theoretical foundations for the codes feature mechanics of materials models, special finite element models, and boundary element models. Heavy attention will be given to evolution of novel modeling methods that permit non-burdensome yet accurate representations of geometrical discontinuities such as cooling holes and coating cracks. A selection of constitutive relations has been provided for economical or sophisticated description of inelastic material behavior as desired. Finally, advantages which accrue from application of the improved codes to actual components will be demonstrated by execution of benchmark analyses for which experimental data exist.

## SECTION 2.0

### SUMMARY

The 3-D Inelastic Analysis Methods program is divided into two 24-month segments: a base program, and an option program to be exercised at the discretion of the Government. During the base program, a series of new computer codes embodying a progression of mathematical models (mechanics of materials, special finite element, boundary element) is being developed for the streamlined analysis of combustor liners, turbine blades and turbine vanes. These models will address the effects of high temperatures and thermal/mechanical loadings on the local (stress/strain) and global (dynamics, buckling) structural behavior of the three selected components.

The first year (Task I) of the base program dealt with "linear" theory in the sense that stresses/strains and temperatures in generic modeling regions are linear functions of the spatial coordinates, and solution increments for load, temperature and/or time are extrapolated linearly from previous information. Three linear formulation computer codes, hereafter referred to as MMM (Mechanics of Materials Model), MHOST (MARC-HOST), and BEST (Boundary Element Stress Technology), have been created and are described in more detail in the First Annual Status Report (NASA CR-174700).

The second half of the base program (Task II), as well as the option program (Tasks IV and V), will extend the models to include higher-order representations of deformations and loads in space and time and deal more effectively with collections of discontinuities such as cooling holes and coating cracks. Work on Task II (polynomial theory) has been completed, and the results are given in the third section of this Second Annual Status Report.

#### 2.1 CONSTITUTIVE MODELS

Three increasingly rigorous constitutive relationships are employed by MMM, MHOST, and BEST to account for nonlinear material behavior (creep/plasticity effects) in the elevated temperature regime. The simplified model assumes a bilinear approximation of stress-strain response and generally glosses over

the complications associated with strain rate effects, etc. (Section 3.1.1). The state-of-the-art model partitions time-independent (plasticity) and time-dependent (creep) phenomena in the conventional way, invoking the Mises yield criterion and standard (isotropic, kinematic, combined) hardening rules for the former and a power law for the latter (Section 3.1.2). Walker's viscoplastic theory, which accounts for the interaction between creep and plasticity that occurs under cyclic loading conditions, has been adopted as the advanced constitutive model (Section 3.1.3).

## 2.2 MECHANICS OF MATERIALS MODEL

In essence, the Mechanics of Materials Model (MOMM) is a stiffness method finite element code that utilizes one-, two- and three-dimensional arrays of beam elements to characterize hot section component behavior. Limitations of such beam model representations are recognized, of course, but are fully acceptable in view of the benefits of having a fast, easy to use, computationally efficient tool available for application during the early phases of component design. The full complement of structural analysis types (static, buckling, vibration, dynamics) is provided by MOMM, in conjunction with the three constitutive models mentioned above. Capabilities of the code have been tested for a variety of relatively simple problem discretizations (examples are provided in Section 3.2.2).

## 2.3 SPECIAL FINITE ELEMENT MODEL

The MHOST (MARC-HOST) code employs both shell and solid (brick) elements in a mixed method framework to provide comprehensive capabilities for investigating local (stress/strain) and global (vibration, buckling) behavior of hot section components. Development of the code has taken full advantage of the wealth of technical expertise accumulated at the MARC Corporation over the last decade in support of their own commercially available software packages to create new/improved algorithms (Section 3.3.4) that promise to significantly reduce CPU (central processing unit) time requirements for three-dimensional analyses. Second generation (Task II) MHOST code is operational and has been tested with a variety of academic as well as engine-related configurations (Section 3.3.6).

## 2.4 ADVANCED FORMULATION (BOUNDARY ELEMENT) MODEL

Development of the new BEST (Boundary Element Stress Technology) code constitutes a very important accomplishment of the Task II effort. The difficult challenge of extending the basic theory and algorithms to deal effectively with inelastic and dynamic effects in three-space was successfully met by combining the special skills and efforts of the research and programming teams at SUNY-B and P&W. As with MOMM and MHOST, the second version of BEST is operational and has been exercised with a number of small and large test cases (Section 3.4.5). While MHOST and BEST are currently viewed as mutually complementary, they are also competitors; and overall performance on large inelastic models will be watched with high interest as the codes continue to mature.

## SECTION 3.0

### TECHNICAL PROGRESS

#### 3.1 CONSTITUTIVE MODELS

Three material models are available for use with the mechanics of materials, special finite element, and boundary element models: 1) a simplified material model, 2) a state-of-the-art material model, and 3) an advanced material model. The simplified model uses secant moduli and assumes a bilinear stress-strain response which is currently neither strain-rate nor temperature dependent. Later versions of the simplified material model may include provisions for both temperature and strain-rate dependence. The state-of-the-art material model is a standard elastic-plastic-creep model (Reference 1). The advanced model is a modified form of Walker's viscoplastic material model (References 2 and 3). The following sections provide a detailed discussion of each of these models.

##### 3.1.1 Simplified Secant Elastic Model

In the simplified elastic model, stress-strain curves for various strain rates are the basic input material properties. Tension response is assumed to be the same as compression response. The initial response is represented by an elastic material with modulus,  $E_0$ , and Poisson's ratio,  $\nu_0$ . At the conclusion of the calculation for the response, an equivalent strain is predicted. At this strain, two equivalent stresses can be considered: 1) the calculated stress, and 2) the stress from the input stress-strain curves at the predicted strain. If the two stresses are sufficiently close in value, then the calculations can be terminated. If the two stresses are not sufficiently close, then the new modulus is taken to be the stress from the stress-strain curves divided by the strain, and the calculations are repeated.

This concept must now be expanded to multidimensional stress states. For this purpose, consider an elastic material, then:

$$\epsilon_{ij} = \frac{1 + \nu}{E} \sigma_{ij} - \frac{\nu}{E} \sigma_{kk} \delta_{ij} \quad (3.1-1)$$

where:

$\epsilon_{ij}$  is the mechanical strain tensor (i.e., total strain minus thermal strain),

$\sigma_{ij}$  is the stress, and

$\delta_{ij}$  is the Kronecker delta.

The stress and strain can be partitioned into deviatoric and volumetric parts,

$$\epsilon_{ij} = e_{ij} + 1/3 \epsilon_{kk} \delta_{ij} \quad (3.1-2)$$

$$\sigma_{ij} = S_{ij} + 1/3 \sigma_{kk} \delta_{ij} \quad (3.1-3)$$

The volumetric components, from equation (3.1-1) are related by:

$$\epsilon_{kk} = \frac{1 - 2\nu}{E} \sigma_{kk} = \frac{1}{3K} \sigma_{kk} \quad (3.1-4)$$

where  $K$  is the bulk modulus.

The deviatoric parts can be shown to be related by:

$$e_{ij} = \frac{1 + \nu}{E} S_{ij} \quad (3.1-5)$$

Let the equivalent stress be represented by:

$$\bar{\sigma} = \sqrt{3J_2} = \sqrt{3/2 S_{ij} S_{ij}} \quad (3.1-6)$$

where  $J_2$  is the second invariant of the deviatoric stress tensor.

Then, from equations (3.1-5) and (3.1-6):

$$\bar{\sigma} = \frac{E}{1 + \nu} \sqrt{3/2 e_{ij} e_{ij}} \quad (3.1-7)$$

Similarly, the equivalent strain can be taken to be:

$$\bar{\epsilon} = \sqrt{3j_2} = \sqrt{3/2 e_{ij} e_{ij}} \quad (3.1-8)$$

where  $j_2$  is the second invariant of the deviatoric strain tensor.

Equation (3.1-7) now becomes:

$$\bar{\sigma} = \left( \frac{E}{1 + \nu} \right) \bar{\epsilon} = 2G\bar{\epsilon} \quad (3.1-9)$$

Since only the ratio  $\bar{\sigma}/\bar{\epsilon}$  will be used to represent the material response, an additional assumption is needed to obtain the second elastic constant. For this purpose, assume the bulk modulus is constant, and given by equation (3.1-4):

$$K = \frac{E}{3(1 - 2\nu)} = \frac{E_0}{3(1 - 2\nu_0)} = \frac{2(1 + \nu_0)G_0}{3(1 - 2\nu_0)} \quad (3.1-10)$$

where  $G_0$ ,  $E_0$ ,  $\nu_0$  are the moduli and Poisson's ratio at the origin (i.e.,  $\bar{\sigma}=\bar{\epsilon}=0$ ). The current shear modulus is known from the slope  $\bar{\sigma}/\bar{\epsilon}$ . Then from equation (3.1-9)

$$\frac{2(1 + \nu)G}{3(1 - 2\nu)} = \frac{2(1 + \nu_0)G_0}{3(1 - 2\nu_0)} \quad (3.1-11)$$

Solving equation (3.1-11) for:

$$\nu = \frac{1}{2} \left[ 1 - \frac{3(G/G_0)}{\frac{2(1 + \nu_0)}{1 - 2\nu_0} + \frac{G}{G_0}} \right] \quad (3.1-12)$$

Figure 3.1-1 presents the variation in Poisson's ratio with modulus. The Young's modulus can be determined from:

$$E = 2(1 + \nu)G = (1 + \nu)\bar{\sigma}/\bar{\epsilon} \quad (3.1-13)$$

As an example, consider a uniaxial stress state:

$$\sigma_{ij} = \begin{cases} \sigma & i=j=1 \\ 0 & i \neq 1, j \neq 1 \end{cases} \quad \text{and} \quad \epsilon_{ij} = \begin{cases} \epsilon & i=j=1 \\ -\nu\epsilon & i=j=2,3 \\ 0 & i \neq j \end{cases} \quad (3.1-14)$$

Then:

$$\bar{\sigma} = \sigma \quad \text{and} \quad \bar{\epsilon} = (1 + \nu)\epsilon = \epsilon_{11} - \epsilon_{22} \quad (3.1-15)$$

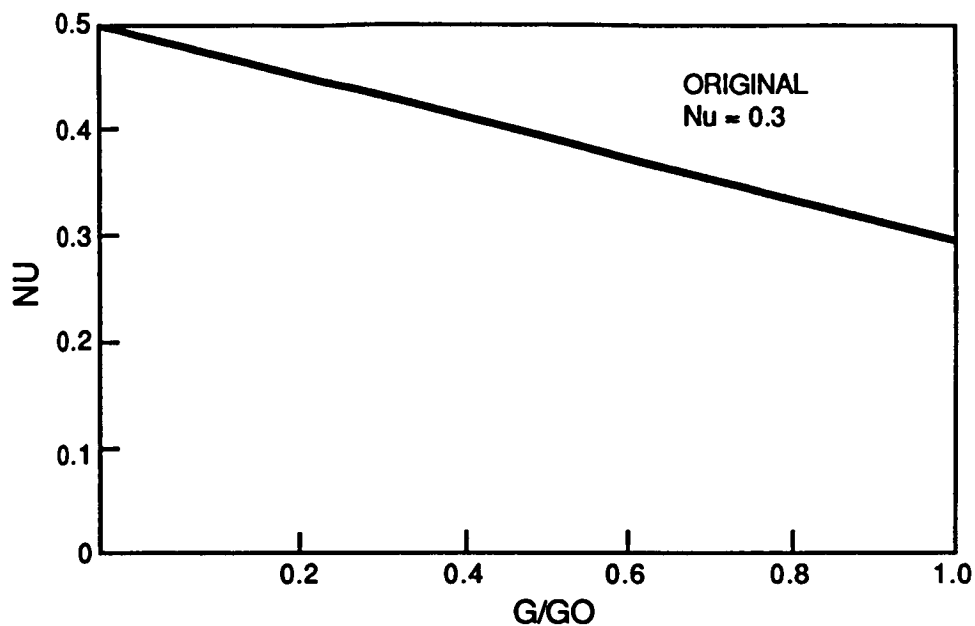


Figure 3.1-1 Variation in Nu

The  $\bar{\sigma}$ ,  $\bar{\epsilon}$  curve is now the input stress-strain curve.

To illustrate the convergence of the iterative procedure, consider three parallel bars supporting an equivalent total load. The bars are assumed to be elastic-plastic. Each has a Young's modulus of  $10 \times 10^6$  psi and a hardening slope of  $0.5 \times 10^6$  psi. The yield stresses are different. The central bar will be assumed to have a yield stress of 20 ksi while the two outer bars have a yield stress of 10 ksi. The area of each bar is  $1/3$  in<sup>2</sup>, making a total area of 1.0 in<sup>2</sup>. Figure 3.1-2 illustrates that convergence has occurred in six iterations for a total load of 30,000 lb and that each of the bars has yielded.

The material constants for the simplified model are input to the computer code through data input cards.

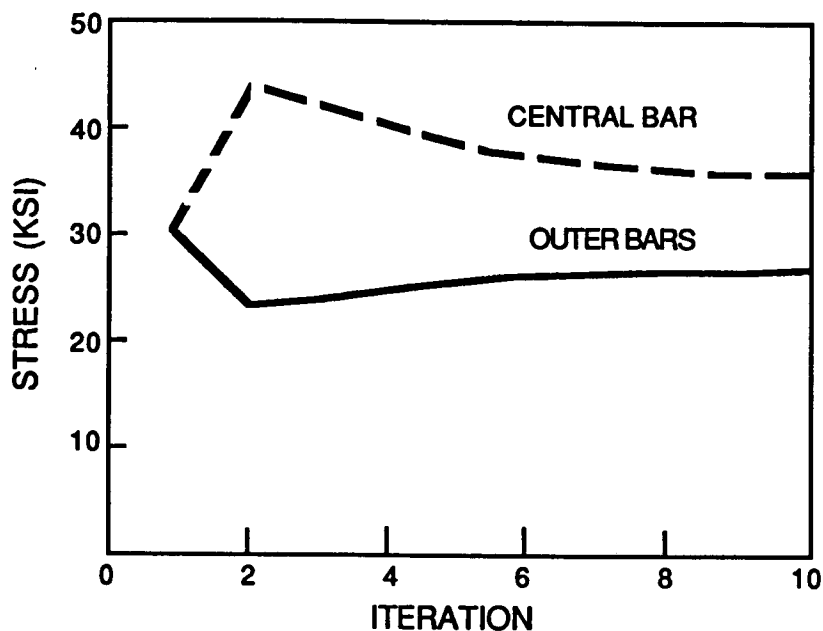


Figure 3.1-2 Three Bar Convergence Using Simplified Model

### 3.1.2 Current State-of-the-Art Model

The current state-of-the-art model has been taken to be the classical elastic-plastic-creep model that is available in the MARC code, and described in Reference 1. The creep model is essentially a steady state power law (stress) model. The plasticity model includes isotropic, kinematic, and a combined hardening law. Both the creep and plasticity models assume no permanent volumetric deformations. For the mechanics of materials computer code, the material properties for the state-of-the-art constitutive model are included in data statements in subroutine SOACON.

#### Plastic Iteration Procedure

Consider the case of a small strain elastic-plastic response of a typical structure. Sufficiently large applied loads will result in permanent or plastic deformation. A procedure for calculating the response of the structure undergoing plastic deformation is required.

To evaluate the response of the structure, the loading history is divided into a number of incrementally applied loading steps. Each of these load increments can then be applied sequentially to the structure. An iterative scheme is then required to calculate the response of the structure to each individual load increment.

At the beginning of a new load increment it may be assumed that the strain will change in a manner analogous to the previous increment. As an initial estimate all of the strain change is then assumed to be elastic. The change in the stresses can then be calculated using Hooke's Law or:

$$\Delta\sigma_{ij} = L_{ijkl}^e \Delta\epsilon_{kl} \quad (3.1-16)$$

where:  $\Delta\sigma_{ij}$  is the incremental stress vector,

$\Delta\epsilon_{kl}$  is the incremental total strain vector, and

$L_{ijkl}^e$  is the matrix of elastic constants.

If the resulting total stress is within the yield surface, the matrix of material constants,  $L_{ijkl}$  is simply given by:

$$L_{ijkl} = L_{ijkl}^e \quad (3.1-17)$$

If the resulting total stress is outside the yield surface, weighted material constants and stiffness matrices will have to be calculated. It should be noted at this point that if a load increment is exceedingly large and if there is a sudden change in the type of loading, care must be taken in order to iterate to the correct solution.

If the resulting total stress is outside the yield surface, the fraction of the stress increment that remains elastic must be determined. This corresponds to  $\Delta \epsilon_{ij}^{e1}$  in Figure 3.1-3. If the yield surface in stress space is considered

to be given by:

$$f(\sigma_{ij}) = 0,$$

then the appropriate  $m$  in:

$$f(\sigma_{ij}^{i-1} + m\Delta\sigma_{ij}) = 0 \quad (3.1-18)$$

may be determined where  $\sigma_{ij}^{i-1}$  is the stress tensor from the previous increment.

The mean material matrix is calculated from:

$$L_{ijkl} = mL_{ijkl}^e + (1-m)L_{ijkl}^{e-p} \quad (3.1-19)$$

where  $L_{ijkl}^{e-p}$  is the tensor relating  $\dot{\sigma}_{ij}$  and  $\dot{\epsilon}_{kl}$ .

Once the tensor  $L_{ijkl}$  has been determined, standard solutions can be applied to find the incremental changes in the displacements, strains and loads. For example, if the strains are given by:

$$\{\Delta\epsilon\} = [B] \{\Delta u\} \quad (3.1-20)$$

where  $\{\Delta u\}$  is the vector of incremental nodal displacements, and  $[B]$  is the matrix relating the vector of element strains  $\{\Delta\epsilon\}$  to the nodal displacements, the stiffness matrix can be found from:

$$[K] = \int_V [B]^T [D] [B] dV \quad (3.1-21)$$

where  $[D]$  is the matrix representation of the tensor  $L_{ijkl}$ . The strain-displacement matrix  $[B]$  depends on the formulation of the element.

The incremental nodal displacements and strains can be evaluated by solving for  $\Delta u$  in:

$$[K] \{\Delta u\} = \{\Delta P\} + \{\Delta G\} \quad (3.1-22)$$

and then applying equation (3.1-20).

In the mechanics of materials computer code the stiffness matrix  $K$  is held constant, and changes in the stiffness matrix are included in  $\Delta G$ .

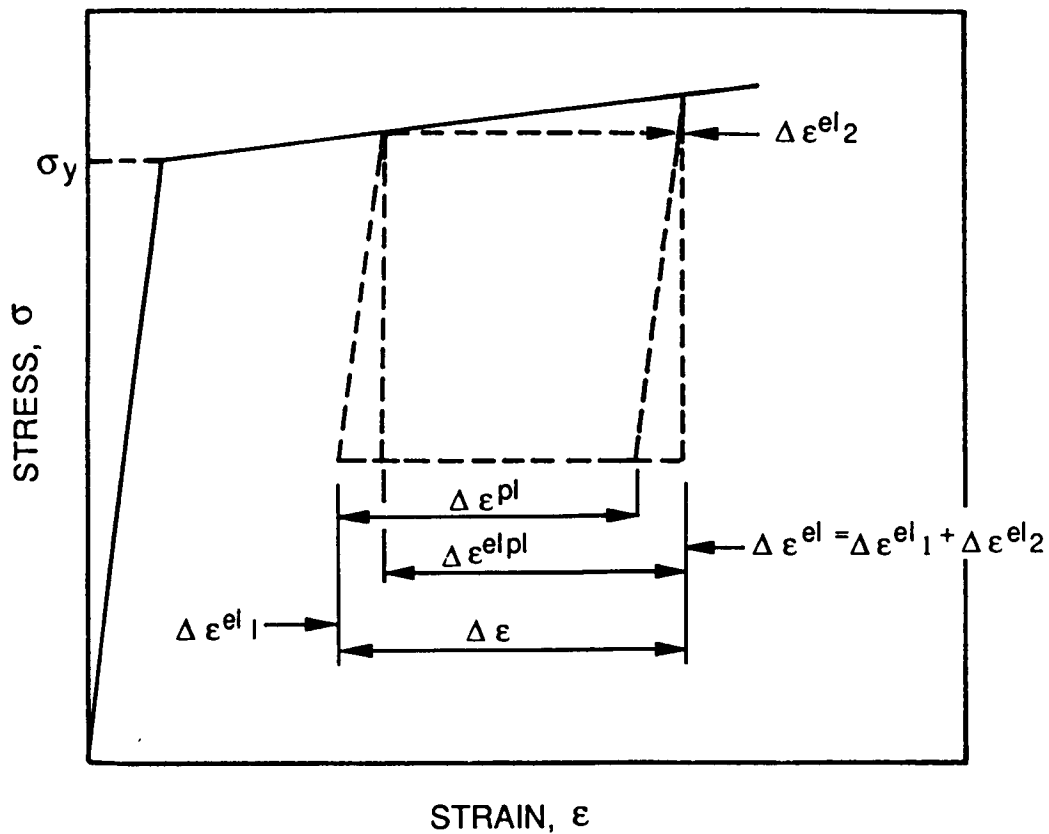


Figure 3.1.3 Elastic-Plastic Strain Decompositions for Bilinear Stress-Strain Law

The term  $\Delta P$  in equation (3.1-22) is the applied incremental load. The term  $\Delta G$  is defined as the pseudo-load correction to the stiffness matrix due to inelastic strains which is added to equation (3.1-22). The  $\Delta G$  vector calculated from creep strain, for example, is shown in equation (3.1-34).

One iteration cycle is completed each time the stiffness matrix is formed and the resulting equations solved. At the end of each cycle the resulting solution must be tested for convergence. This is accomplished, by considering the change in energy,

$$r = \frac{E^N - E^{N-1}}{E^N} = \frac{E^N - E^{N-1}}{1/2 (E^N + E^{N-1})} \quad (3.1-23)$$

where  $E^{N-1}$  is the change in energy summed over all elements on the previous cycle and  $E^N$  is the energy including the present cycle.

An accurate solution will usually result if  $r$  is maintained less than 0.1 for elastic-plastic problems.

If the solution has satisfied the convergence, the stresses and strains can be updated and a new load increment added. If the solution has not converged, then a new guess for the strains, based on the latest cycle, must be input and the calculation procedure repeated. When the solution has not converged after a given number of cycles, the program should exit from the load incrementing loop.

Figure 3.1-4 is a flow chart illustrating the small strain elastic-plastic iteration procedure.

For isotropic materials the moduli in equation (3.1-19) are given by:

$$L_{ijkl}^e = \frac{E}{1 + \nu} \left\{ \delta_{ik} \delta_{jl} + \frac{\nu}{1 - 2\nu} \delta_{ij} \delta_{kl} \right\} \quad (3.1-24)$$

and

$$L_{ijkl}^{e-p} = \frac{E}{1+\nu} \left\{ \delta_{ik}\delta_{jl} + \frac{\nu}{1-2\nu} \delta_{ij}\delta_{kl} - \frac{3/2 (S_{ij} - \Omega_{ij}) (S_{kl} - \Omega_{kl})}{\left[ 1 + \frac{2}{3} \frac{1+\nu}{E} H + \frac{1+\nu}{E} G \right] \sigma_0^2} \right\} \quad (3.1-25)$$

where E is Young's modulus

$\nu$  is Poisson's ratio

$\delta_{ij}$  is the Kronecker delta

$$\sigma_0 = H\bar{\epsilon}^P + \sigma_y \quad (3.1-26)$$

$$\dot{\Omega}_{ij} = G \dot{\epsilon}_{ij}^P \quad (3.1-27)$$

$\dot{\epsilon}_{ij}^P$  are the plastic strain rates

$$\bar{\epsilon}^P = \sqrt{2/3 \dot{\epsilon}_{ij}^P \dot{\epsilon}_{ij}^P} \quad (3.1-28)$$

G is the kinematic hardening slope

H is the isotropic hardening slope

$\sigma_y$  is the initial yield stress, and

$S_{ij} = \sigma_{ij} - 1/3 \sigma_{kk}\delta_{ij}$  is the deviatoric stress.

The strain rate has been decomposed into elastic (including thermal), plastic and creep components, or:

$$\dot{\epsilon} = \dot{\epsilon}^e + \dot{\epsilon}^P + \dot{\epsilon}^C \quad (3.1-29)$$

The plastic yield surface was assumed to satisfy an equivalent Mises yield surface given by:

$$1/2 (S_{ij} - \Omega_{ij}) (S_{ij} - \Omega_{ij}) = 1/3 \sigma_0^2 \quad (3.1-30)$$

The method presented in Reference 4 is used to calculate the elastic-plastic moduli.

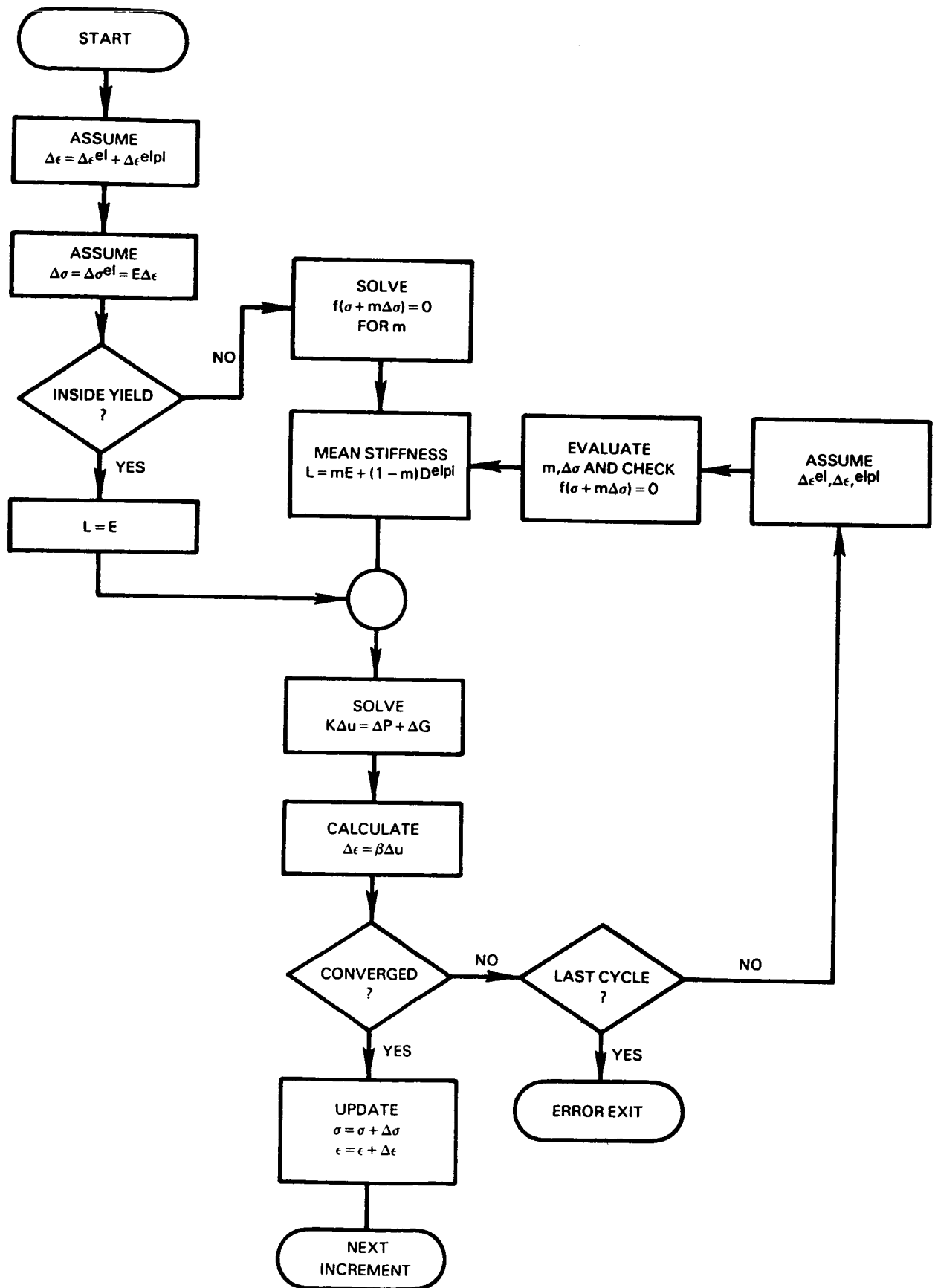


Figure 3.1-4 Elastic-Plastic Iteration Procedure

## Time Effects Iteration Procedure

The creep strain rate will depend in general on the stress, the accumulated creep strain, the temperature and time. To illustrate the incrementing procedure, assume that the creep strain rate is normal to the Mises yield surface in stress space, then the creep strain rate is given by:

$$\dot{\epsilon}_{ij}^{cr} = \left[ \frac{\sqrt{3/2} S_{k1} S_{k1}}{K} \right]^n \frac{3/2 S_{ij}}{\sqrt{3/2} S_{mn} S_{mn}} \quad (3.1-31)$$

For a specific time increment the incremental creep strains were approximated by:

$$\Delta \epsilon_{ij}^{cr} = \dot{\epsilon}_{ij}^{cr} \Delta t. \quad (3.1-32)$$

The incremental displacements are:

$$[K] \{ \Delta u \} = \{ \Delta P \} + \{ \Delta G \} \quad (3.1-33)$$

where

$$\Delta G = \int [B]^T [E] \{ \Delta \epsilon^C \} dV \quad (3.1-34)$$

is the pseudo-creep load,  $\{ \Delta \epsilon^C \}$  is the vector of element creep strain, and  $[E]$  is the elasticity matrix. The strain increment can be calculated from equation (3.1-20) and the strains, creep strains, stresses and displacements can be updated.

A convergence test on the stresses should be performed. If the algorithm has not converged, a shorter time step should be used and the calculations repeated. If the criterion has been satisfied, then the time step can be increased. Figure 3.1-5 is a flow chart illustrating the small strain creep iteration procedure.

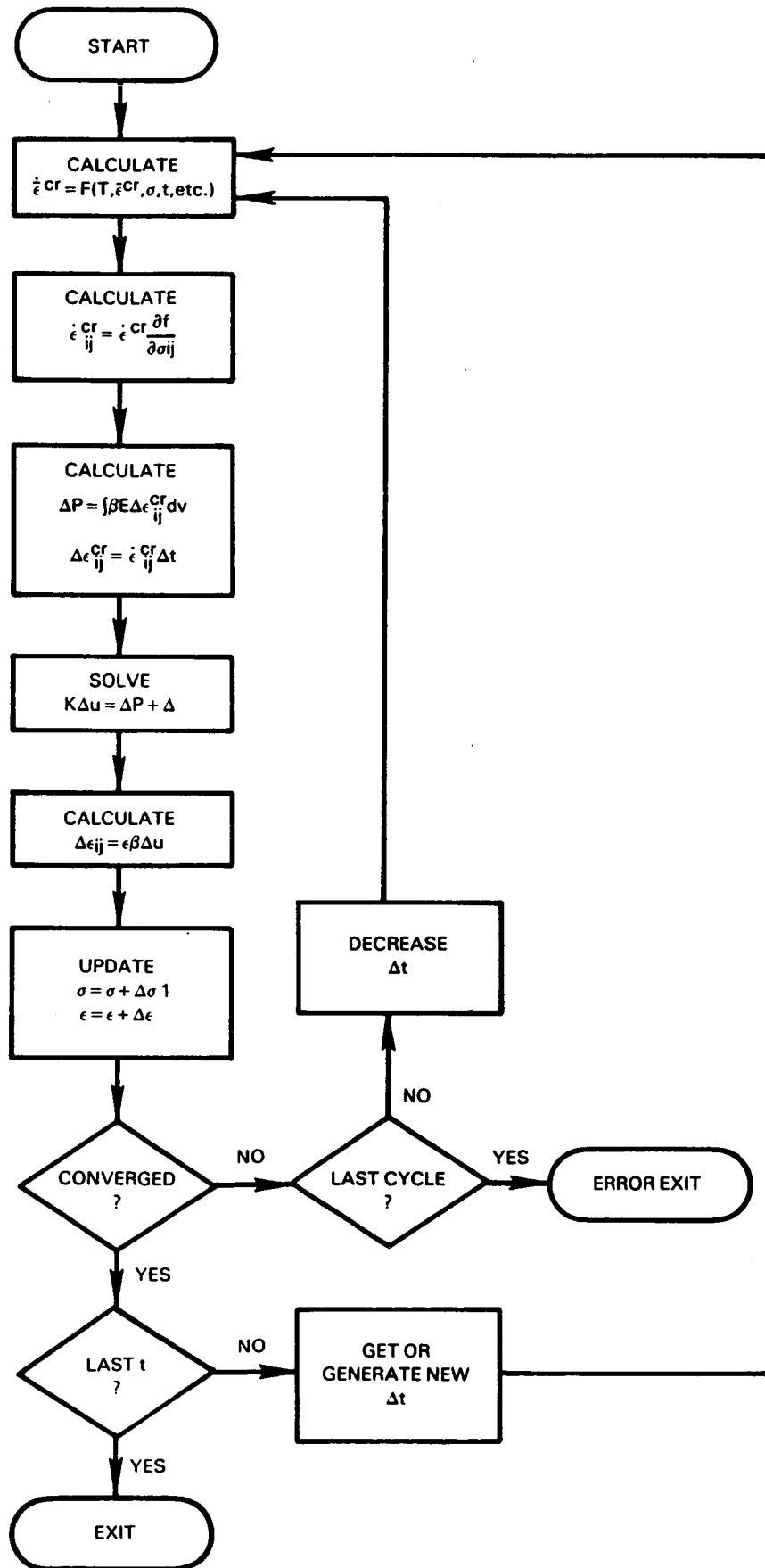


Figure 3.1-5 Creep Iteration Procedure

### 3.1.3 Advanced Viscoplastic Model

The viscoplastic model described in References 2 and 3 has been selected as the advanced constitutive model. Reference 2 describes the basic theory; while Reference 3 describes modifications to the form of the basic theory, and modifications to the material parameters for Hastelloy X. The modifications provide more accuracy at relatively low temperatures.

For uniaxial loading the viscoplastic material model (Figure 3.1-6) reduces to:

$$\dot{c} = \left[ \frac{|\sigma - \Omega|}{K} \right]^n \operatorname{sgn}(\sigma - \Omega) + \frac{(\sigma - \Omega)(1 - k) \langle \sigma \dot{\epsilon} \rangle}{\sigma_{\infty}^2 - k\sigma^2} \quad (3.1-35)$$

$$\dot{\Omega} = n_2 \dot{c} - n_3 |\dot{c}| \Omega \quad (3.1-36)$$

$$c = \epsilon - \frac{\sigma}{E} \quad (3.1-37)$$

where  $C$  is the inelastic strain,

$\Omega$  is the back stress,

$\sigma$  is the stress,

$\epsilon$  is the strain, and

$k, \sigma_{\infty}, n, K, n_2, n_3$  and  $E$  are material constants.

The absolute value and unit ramp functions are represented by:

$$|x| = \begin{cases} -x & x < 0 \\ x & x \geq 0 \end{cases} \quad (3.1-38)$$

and

$$\langle x \rangle = \begin{cases} 0 & x < 0 \\ x & x \geq 0 \end{cases} \quad (3.1-39)$$

The inelastic strain in equation (3.1-35) consists of two components: 1) a time dependent power law creep component, containing the material constants  $n$  and  $k$ , and 2) a time independent plastic component, containing the material constants  $\sigma_{\infty}$  and  $k$ . The parameter  $\sigma_{\infty}$  becomes equivalent to the yield stress as: 1)  $k$ , in equation (3.1-35), approaches unity, and 2) the back stress,  $\Omega$ , approaches zero. The back stress is a key variable in many viscoplastic material models. Its evolution is given by equation (3.1-36). Equation (3.1-37) represents the inelastic strain as the difference between the total strain and the elastic strain.

$$\dot{c}_{ij}^c = \left( \frac{\sqrt{3J_2^1}}{\kappa} \right)^n \left( \frac{\frac{2}{3} s_{ij} - \Omega_{ij}}{\sqrt{3J_2^1}} \right)$$

$$\dot{c}_{ij}^p = \frac{\left( \frac{2}{3} s_{ij} - \Omega_{ij} \right) (1 - \kappa) \langle \sigma_{ij} \dot{c}_{ij} \rangle}{\sigma_{\infty}^2 [1 - \kappa (3J_2^1 / \sigma_{\infty}^2)]}$$

$$\dot{\Omega}_{ij} = (n_1 + n_2) \dot{c}_{ij} + c_{ij} \frac{dn_1}{d\Theta} \dot{\Theta} - (\Omega_{ij} - \overset{\circ}{\Omega}_{ij} - n_1 c_{ij}) \left( \sigma - \frac{1}{n_2} \frac{dn_2}{d\Theta} \Theta \right) \cdot \dot{\overset{\circ}{\Omega}}_{ij}$$

$$\kappa = \kappa_1 - \kappa_2 e^{-n_3 R} = \beta \sigma_{\infty}$$

$$\dot{c}_{ij} = \dot{c}_{ij}^c + \dot{c}_{ij}^p$$

$$c_{ij} = (\delta_{ij} \lambda \epsilon_{kk} + 2\mu \epsilon_{ij} - \sigma_{ij} - \delta_{ij} (3\lambda + 2\mu) \alpha \Theta) / 2\mu$$

$$\dot{G} = (n_3 + n_4 e^{-n_5 R}) \dot{R} + n_6 \left( \frac{2}{3} \Omega_{ij} \dot{\Omega}_{ij} \right)^{\frac{m-1}{2}}$$

$$\dot{R} = \sqrt{\frac{2}{3} \dot{c}_{ij} \dot{c}_{ij}}$$

$$\dot{\overset{\circ}{\Omega}}_{ij} = 3\overset{\circ}{\Omega} \left[ \frac{\dot{c}_{ik} c_{kj}}{C_{pq} C_{pq}} + \frac{c_{ik} \dot{c}_{kj}}{C_{pq} C_{pq}} - \left( \frac{2c_{ik} c_{kj}}{C_{pq} C_{pq}} \right) \left( \frac{C_{rs} \dot{C}_{rs}}{C_{uv} C_{uv}} \right) \right] + \left[ 3 \frac{c_{ik} c_{kj}}{C_{pq} C_{pq}} - \delta_{ij} \right] \frac{d\overset{\circ}{\Omega}}{d\Theta} \dot{\Theta}$$

$$s_{ij} = \sigma_{ij} - \frac{1}{3} \delta_{ij} \sigma_{kk}$$

$$3J_2^1 = \frac{2}{3} \left( \frac{2}{3} s_{ij} - \Omega_{ij} \right) \left( \frac{2}{3} s_{ij} - \Omega_{ij} \right)$$

Material constants  $\lambda, \mu, \overset{\circ}{\Omega}, n, m, n_1, n_2, n_3, n_4, n_5, n_6, n_7, \kappa_1, \kappa_2, k, \sigma_{\infty}$  depend on temperature

Figure 3.1-6 Modified Walker's Theory

Subroutine HYPELA in the mechanics of materials computer code integrates Walker's viscoplastic equations and calls subroutine HYPCON to evaluate the material parameters. HYPCON contains the latest estimates for the parameters in the modified Walker's theory. Each load increment in the analysis is divided into NSPLIT subincrements. The integration of the constitutive equations is performed by using forward differences with a step size determined by dividing the load increment by NSPLIT. Subroutine HYPELA performs the integration in two ways: 1) a fixed step size, or 2) a variable step size. In the fixed step size, forward difference NSPLIT is the same for all load increments and subincrements.

In the variable step size, forward difference NSPLIT is determined by the magnitude of the change in a strain measure for every subincrement. The change in the strain measure is defined as:

$$E = \Delta R + \frac{\sqrt{3\Delta J_2}}{2\mu} \quad (3.1-40)$$

where

$$\Delta R = \sqrt{2/3 \Delta C_{ij} \Delta C_{ij}} \quad (3.1-41)$$

$$\Delta J_2 = 3/2 \Delta S_{ij} \Delta S_{ij} \text{ and} \quad (3.1-42)$$

the quantity  $\Delta \bar{\epsilon}$  is calculated and is stored as variable ERROR0. There are three possible ways to determine NSPLIT. The method depends on the size of ERROR0. If

$$\text{ERROR2} < \text{ERROR0} < \text{ERROR1}, \quad (3.1-43)$$

then NSPLIT remains the same for the next subincrement (ERROR1 and ERROR2 are user-specified in HYPELA). If

$$\text{ERROR0} < \text{ERROR2}, \quad (3.1-44)$$

then NSPLIT is divided in two for the next subincrement and rounded (up) to the nearest integer. If

ERROR0 > ERROR1, (3.1-45)

then NSPLIT is doubled and the step is recomputed. The value of NSPLIT at the end of the increment is stored in the state variable TEMP(16). The initial value of NSPLIT is user-specified in HYPELA. The maximum value of NSPLIT is specified by MXSPLT. If NSPLIT exceeds MSXPLT, the message:

"UNABLE TO REDUCE ERROR IN LESS THAN MXSPLT SUBINCREMENTS"

is written where the value of MXSPLT is inserted in the WRITE statement. After this, the integration is performed using a constant step size.

### 3.1.4 List of Symbols

#### List of Symbols Referenced Within Section 3.1

<u>Symbol</u>	<u>Description</u>	<u>Page</u>
$\epsilon_{ij}$	Strain	8
$\sigma_{ij}$	Stress	8
$\delta_{ij}$	Kronecker delta	8
$\nu$	Poisson's ratio	8
E	Young's modulus	8
$e_{ij}$	Deviatoric strain	8
$s_{ij}$	Deviatoric stress	8
K	Bulk modulus	8
$J_2$	Second invariant of the deviatoric stress tensor	8
$j_2$	Second invariant of the deviatoric strain tensor	8
$\bar{\sigma}$	Equivalent stress	8
$\bar{\epsilon}$	Equivalent strain	8
G	Shear modulus	9
$L_{ijkl}$	Matrix of material constants	12
$\{\Delta u\}$	Incremental nodal displacements	13
$\{\Delta \sigma\}$	Incremental stress	13
$[B]$	Strain-displacement matrix	13
$[K]$	Stiffness matrix	13

List of Symbols  
Referenced Within Section 3.1

<u>Symbol</u>	<u>Description</u>	<u>Page</u>
$\{\Delta P\}$	Incremental applied load vector	14
$\{\Delta G\}$	Incremental pseudo-load vector	14
$E^N$	Energy in Nth cycle	15
$r$	Convergence parameter	15
$[E]$	Elasticity matrix	18
$G$	Kinematic hardening slope	16
$H$	Isotropic hardening slope	16
$\Omega$	Back stress	20
$c$	Inelastic strain	20
$\left. \begin{array}{l} \lambda, \mu, \dot{\Omega}, n, \\ m, n_1, n_2, \\ n_3, n_4, n_5, \\ n_6, n_7, K_1, \\ K_2, k, \sigma_{\infty} \end{array} \right\}$	Material constants	20

### 3.1.5 References

1. "MARC General Purpose Finite Element Program," Volume A, B, C, D, E, Revision J2, MARC Analysis Research Corporation, Palo Alto, California, 1981.
2. K. P. Walker, "Research and Development Program for Nonlinear Structural Modeling with Advanced Time-Temperature Dependent Constitutive Relationships," NASA CR-165533, November 1981.
3. B. N. Cassenti and R. L. Thompson, "Material Response Predictions for Hot Section Gas Turbine Engine Components," AIAA-83-2020, presented at the AIAA/SAE/ASME 19th Joint Propulsion Conference, Seattle, Washington, June 27-29, 1983.
4. J. R. Rice and D. M. Tracey, "Computational Fracture Mechanics," Numerical and Computer Methods in Structural Mechanics, edited by S. J. Fennes, N. Perrone, A. R. Robinson and W. C. Schnobrich, Academic Press, New York, 1973.

## 3.2 MECHANICS OF MATERIALS MODEL

### 3.2.1 Computer Program: Formulation/Description

The three-dimensional nonlinear mechanics of materials finite element computer program utilizes an intersecting network of beams to model a structural component. The program calculates the total strain as a linear function of position in cross section and along the length of the beam. Three material models are included in the code: the simplified material model, Walker's viscoplastic material model, and the state-of-the-art material model. Static and transient analyses can be performed with applied loads, thermal loads, and enforced displacements. Frequencies and mode shapes using either initial or tangent stiffness is calculated; and buckling analysis is included in the static problem using initial or tangent stiffness. The program flow is summarized in Figure 3.2-1.

Input parameters to the computer code consist of information defining the model itself and information describing the method of solution desired. The model is defined by beams which are connected at grid points. The element coordinate system of a given beam is defined by an orientation grid point or vector. The geometry of a beam is rectangular in cross section, with the dimensions of the cross section along the element coordinate axes specified. The material properties are specified for each beam, including Young's modulus, Poisson's ratio, mass density, coefficient of expansion, and yield stress. The initial temperature of the beam network is input, and the time at initial conditions is set to zero. A hardening slope for use with the simplified material model is entered, with a zero slope indicating perfectly-plastic behavior. Boundary conditions are specified by indicating at each node, a constrained or nonconstrained condition for the six degrees of freedom.

Input associated with the selection of the method of solution include the parameters that indicate:

1. the choice of constitutive model to be used,
2. the choice of a static or transient analysis,

3. the choice of initial or tangent stiffness in solving for the frequencies and mode shapes, and
4. the choice of including buckling analysis with either initial or tangent stiffness.

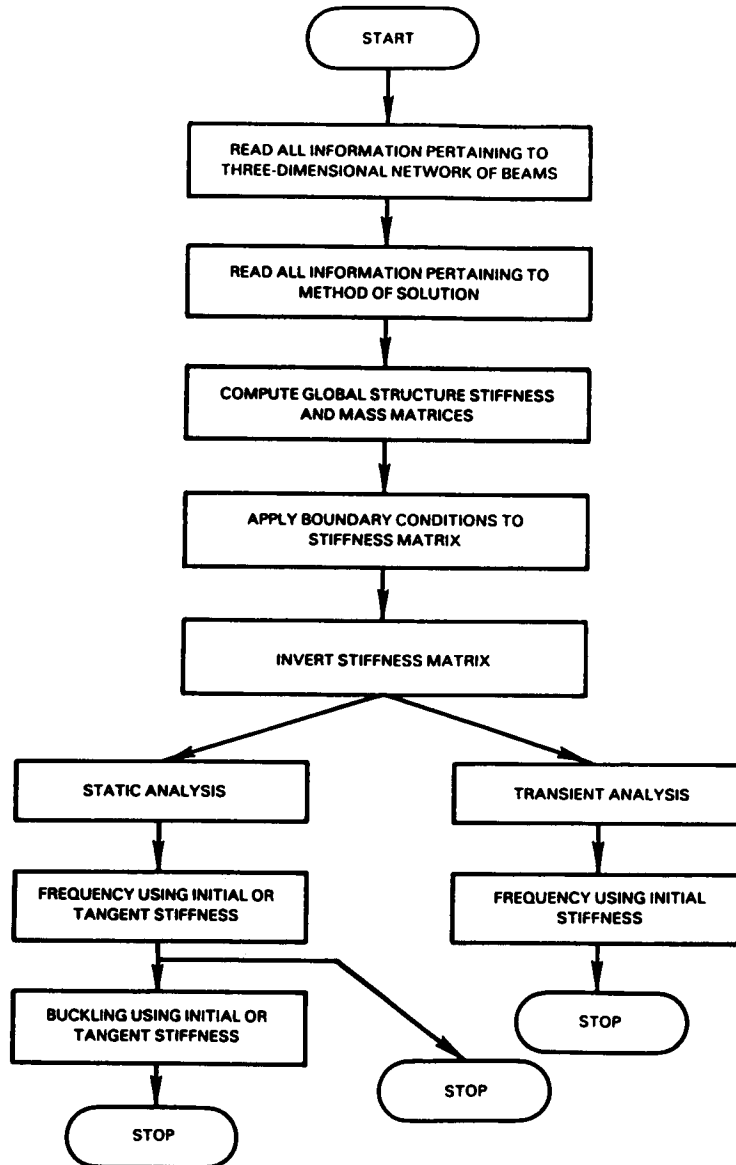


Figure 3.2-1 3-D Inelastic Mechanics of Materials Computer Program Flow Chart

The number of integration points in each direction in each beam is user-specified; stresses and strains are calculated at each integration point, and the user specifies up to 100 points along each element coordinate axis direction in each beam. The convergence value, defining the allowable energy change between two consecutive iterations in the static analysis or allowable range in internal energy for the adaptive time step calculation in the transient analysis, is entered by the user. The number and type of loading increments are also specified.

The stiffness and mass matrices for each beam in the element coordinate system are computed and transformed to the global coordinate system. The stiffness and mass matrices are then assembled to form the global mass and stiffness matrices. The boundary conditions are applied to the stiffness matrix, and the matrix is then inverted. Any change in the stiffness due to nonlinear effects will be accounted for in the pseudo-load vector; therefore, the stiffness matrix is only inverted once.

Depending on user-input, the program now is directed to the appropriate branch of the program: static or transient analysis. For static analysis, the loading increment is read from the data input, including forces and moments or enforced displacements, specified at each degree of freedom of the structure. The temperature increment is also entered. An initial incremental displacement vector is set to zero and strain, stress and pseudo-load vectors are calculated from the incremental displacement vector using the mechanics of materials model selected by the user. The pseudo-load vector accounts for the effects of nonlinearity and allows the use of the original stiffness matrix throughout the calculations. The equations governing the system are as follows:

$$[K] \{\Delta u\} = \{\Delta P\} + \{\Delta G\} \quad (3.2-1)$$

where  $[K]$  = elastic stiffness matrix,  
 $\{\Delta u\}$  = incremental displacement vector,  
 $\{\Delta P\}$  = incremental applied load vector, and  
 $\{\Delta G\}$  = pseudo-load vector, due to inelastic strains.

$$\{\Delta G\} = \int [B]^T [E] \{\Delta \epsilon\} dV \quad (3.2-2)$$

where [B] = strain-displacement matrix,  
 [E] = elasticity matrix, and  
 $\{\Delta \epsilon\}$  = inelastic strains.

Equation (3.2-1) is solved for the incremental displacement vector,  $\Delta u$ , which is substituted for the initial incremental displacement vector and used in the second iteration, continuing until the change in energy in two consecutive iterations is less than the convergence value input by the user. When convergence occurs, the incremental loading, displacements, strains and stresses for that loading increment are printed; the total load, displacement, strain and stress vectors, as well as temperature, are then updated. Each loading increment is read in and executed similarly, and the values of stress, strain and displacement for the total loading are calculated and printed upon conclusion of the last increment.

The transient analysis is based on a simple Euler integration and includes a self-adaptive time step scheme. Damping is not included directly in the transient analysis but is present in the viscoplastic material models. The loading for each increment is the total load at that given time, which is entered into the program by a user-supplied subroutine. The temperature increment and time step are also entered. As in the static branch, the initial displacement vector is set to zero and the strains, stresses and pseudo-load vector are calculated using the designated mechanics of material model. An Euler integration is then used to calculate current displacements at the end of the present time step. The governing equations are as follows:

$$\{A\} = \{\Delta F\} - [K] \{\Delta U_0\} \quad (3.2-3)$$

$$\{\Delta V\} = [M]^{-1} \{A\} * DT \quad (3.2-4)$$

$$\{\Delta U_1\} = (\{V\} + 1/2 \{\Delta V\}) * DT \quad (3.2-5)$$

where  $\{A\}$  = acceleration vector,  
 $\{\Delta F\}$  = applied and pseudo-loads,  
 $[K]$  = elastic stiffness matrix,  
 $\{\Delta U_0\}$  = displacement vector at beginning of time step,  
 $\{\Delta V\}$  = change-in-velocity vector,  
 $[M]$  = mass matrix,  
 $DT$  = time step,  
 $\{\Delta U_1\}$  = displacement vector at end of time step, and  
 $\{V\}$  = velocity vector.

A measure of the work done and the change in internal energy of the system during the time step is computed, and the time step is adapted accordingly. If the time step is accepted, the current displacements, strains and stresses are printed, and the current displacements are inserted for the initial displacements in the following time step. If the time step is unacceptable according to the adaptive scheme, the time step is changed, the load is recalculated, and the displacements are reset to the initial value at the beginning of that time step. The analysis continues until the user-designated number of increments are completed.

Following the static or transient analysis, the user has a choice between calculating the lowest frequency and mode shape or all frequencies and mode shapes. The method of solution for the calculation of the lowest frequency and mode shape is the inverse power method, which is represented by the following expression:

$$([K]^{-1} [M] - \lambda [I]) \{x_{i+1}\} = \{x_i\} \quad (3.2-6)$$

where  $[K]$  = stiffness matrix,  
 $[M]$  = mass matrix,  
 $[I]$  = identity matrix,  
 $\lambda$  = eigenvalue, and  
 $\{x\}$  = eigenvector.

The method of solution in the calculation of all frequencies and mode shapes for a given problem is the Jacobi method, which is based on simple similarity transformations.

The procedure for determining the coefficients of the inverse stiffness matrix is one that can represent the original stiffness of the structure or the current stiffness including nonlinear effects. A small load is placed at one of the nonconstrained degrees of freedom of the structure, and the displacements are computed using the specified constitutive model. The coefficients of the appropriate row of the inverse stiffness matrix are calculated by dividing the calculated displacements by the applied force. This procedure is continued for each nonconstrained degree of freedom until an inverse stiffness matrix, with dimensions equal to the number of nonconstrained degrees of freedom of the structure, is formed. If the frequency is to be calculated using the initial stiffness of the structure, all variables used in the static or transient analysis are set to the original values. If the tangent stiffness is requested, all variables retain the current values for use in the frequency calculation. Only the initial stiffness option is available for use in a transient analysis since current stiffness cannot be readily calculated.

Buckling analysis can be executed in a static problem. The buckling analysis is based on a two step process similar to that in the NASTRAN finite element code. In the first step, the beam loads are determined. In the second step, a first order large displacement correction, proportional to the loads, is included in the stiffness matrix. Buckling occurs when the determinant of the new matrix vanishes. In the determination of the stiffness matrix used in the buckling calculation, the stiffness coefficients are calculated in the same fashion as was described in the frequency calculation, with the user choosing the initial or tangent stiffness. The beam loads are calculated using the initial stiffness matrix and then adding the pseudo-load vector. The actual buckling calculations are accomplished using the inverse power method to find the critical buckling factor and the buckled shape.

Applied loads are entered by specifying the number of loading increments, the number of nodes with concentrated loads, and the number of beams with distributed loads. Concentrated loads are input by defining the values of the six components of the loading at that node. Distributed loads are calculated using a consistent load formulation. The user inputs the six components of the load

at both end A and end B of the beam, and the distributed load is defined as linear between the two ends. A consistent load formulation is then used to calculate the nodal force vector for the beam, which is inserted into the appropriate section of the global force vector. Enforced displacements can be entered in the same way as concentrated loads; however, the corresponding boundary conditions must be constrained.

Axial and transverse holes can be added to any beam. All holes are rectangular and the centerline of a hole must coincide with the centerline of the beam cross section, i.e., no off-center holes. Axial holes are input so that the wall thickness of the beam is constant. A section containing a hole is modeled as a beam with a constant cross section, and the values of cross sectional area, moments of inertia, and torsional stiffness are calculated and used to form the beam stiffness matrix in the same way as for a solid rectangular cross section. Calculations at integration points for determining the pseudo-load vector, strains, and stresses are bypassed if that integration point lies in a hole.

Multipoint constraint equations can be supplied by the user. Each equation consists of a dependent degree of freedom defined in terms of the independent degrees of freedom. The equation is in the form:

$$\{u_m\} = [G_m] \{u_n\} \quad (3.2-7)$$

where  $\{u_m\}$  = set of dependent degrees of freedom  
 $\{u_n\}$  = set of independent degrees of freedom  
 $[G_m]$  = multipoint constraint matrix.

The load-stiffness relationship can now be partitioned as follows:

$$\begin{bmatrix} \bar{K}_{nn} & K_{nm} \\ K_{nm}^T & K_{mn} \end{bmatrix} \begin{Bmatrix} u_n \\ u_m \end{Bmatrix} = \begin{Bmatrix} \bar{P}_n \\ P_m \end{Bmatrix} \quad (3.2-8)$$

Writing equations (3.2-7) and (3.2-8) together and eliminating  $u$  gives:

$$[\bar{K}_{nn} + K_{nm} G_m + G_m^T K_{nm}^T + G_m^T K_{mm} G_m] \{u_n\} = \{\bar{P}_n\} + [G_m^T] \{P_m\} \quad (3.2-9)$$

or

$$[K_{nn}] \{u_n\} = \{P_n\} \quad (3.2-10)$$

where  $K_{nn} = \bar{K}_{nn} + K_{nm} G_m + G_m^T K_{nm}^T + G_m^T K_{mm} G_m$

$$P_n = \bar{P}_n + G_m^T P_m$$

Cracks can be added to the structure. The user specifies the location and crack depth, and the computer code uses the elastic line spring model to determine the effect of the crack on the stiffness of the structure. The equation defining the line spring model is below:

$$\begin{Bmatrix} \delta_c \\ \theta_c \end{Bmatrix} = \begin{bmatrix} P_{11} & P_{12} \\ P_{21} & P_{22} \end{bmatrix} \begin{Bmatrix} N \\ M \end{Bmatrix} \quad (3.2-11)$$

- where  $\delta_c$  = displacement due to crack  
 $\theta_c$  = rotation due to crack  
 $N$  = axial force in crack area  
 $M$  = bending moment in crack area  
 $P$  = crack flexibility matrix.

The matrix  $[P]$  is determined from stress intensity factor calibrations of a plane-strain single edge notched specimen using energy-compliance relations. The matrix  $[P]$  is inverted and added at the appropriate positions in the global stiffness matrix. The elastic stress intensity factor is calculated for each crack as follows:

$$K = (\pi a)^{1/2} [F_1 \sigma_A + F_2 \sigma_B] \quad (3.2-12)$$

where       $K$  = stress intensity factor  
             $a$  = crack depth  
             $\sigma_A$  = axial stress  
             $\sigma_B$  = bending stress  
             $F_1, F_2$  = functions in terms of crack depth and beam thickness.

The functions  $F_1$  and  $F_2$  determine the effect of a crack on the stiffness of the structure. These variables are functions of the crack depth and beam thickness. In addition, these variables are calculated internally in the Mechanics of Materials Model (MOMM) and are not required as input.

The MOMM computer code was designed to be utilized as an initial analysis tool for hot section components. Beam elements can be used to create simple three-dimensional finite element models that approximate the axial, bending and torsional stiffnesses of the components being analyzed. The rectangular beam section used in any particular model has stiffnesses that are a function of the dimensions of the cross section of the beam. The axial stiffness is dependent on the cross sectional area; the bending stiffnesses are related to the moments of inertia about the appropriate axes; and the torsional stiffness is derived from the polar moment of inertia. Application of simple mechanics of materials calculations and engineering judgement are needed to ensure a beam design that will produce accurate results.

### 3.2.2 Program Validation/Verification

Some of the test cases (i.e., TEST1 - TEST5) which have been executed to validate MOMM computer code are summarized below. Each of these cases test various segments of the theory and computer code.

#### TEST1 - Cantilever Beam With Axial Load

A cantilever beam is loaded with a single static compressive loading increment. The beam (Figure 3.2-2) is made up of one member, with all degrees of freedom constrained at one end and all but two constrained at the end where the load is applied. The simple material model is used, and the loading causes

only elastic displacements. The lowest frequency and buckling factor are obtained. The displacements, strains and stresses are found to be:

$$u_1 = P/K = -10^{-4}$$

$$\epsilon_1 = u_1/L = -10^{-5}$$

$$\sigma_1 = E\epsilon_1 = -100$$

The resulting lowest frequency and buckling factor are:

$$f_{\text{lowest}} = \frac{w}{2\pi} = \sqrt{\frac{Ku_2}{m}} = 22.5$$

$$cr = \frac{Ku_2}{KG} = 833.3$$

Agreement between these computed values and independent closed-form solutions is exact.

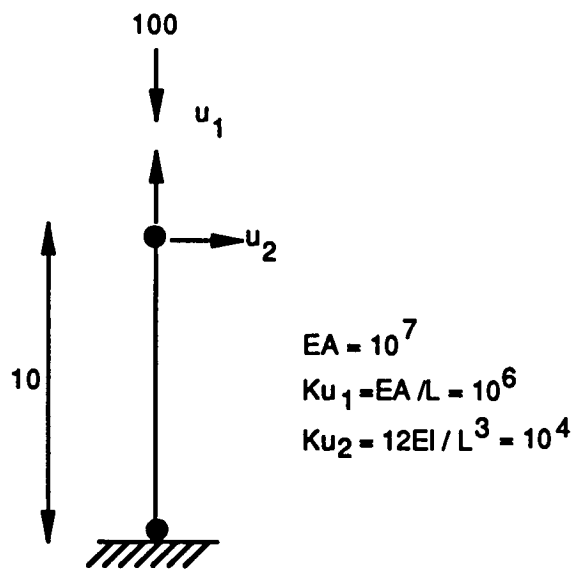


Figure 3.2-2 Schematic of TEST1 Beam

TEST2 - Simply Supported, Centrally-Loaded Square Plate

A quarter of the square plate is modeled using symmetry boundary conditions (Figure 3.2-3). Four outside beams and four interior diagonal beams are used, with dimensions of the beams chosen so as to reproduce the stiffness and mass of the plate. One static loading increment is used with the simple constitutive model in the elastic range. The nonconstrained degrees of freedom are shown.

The theoretical central displacement is:

$$u_2 = .01160 Pa^2/D$$

$$u_2 = -3.2428 \times 10^{-6}$$

The result from the MOMM computer run is:

$$u_2 = -3.4712 \times 10^{-6}$$

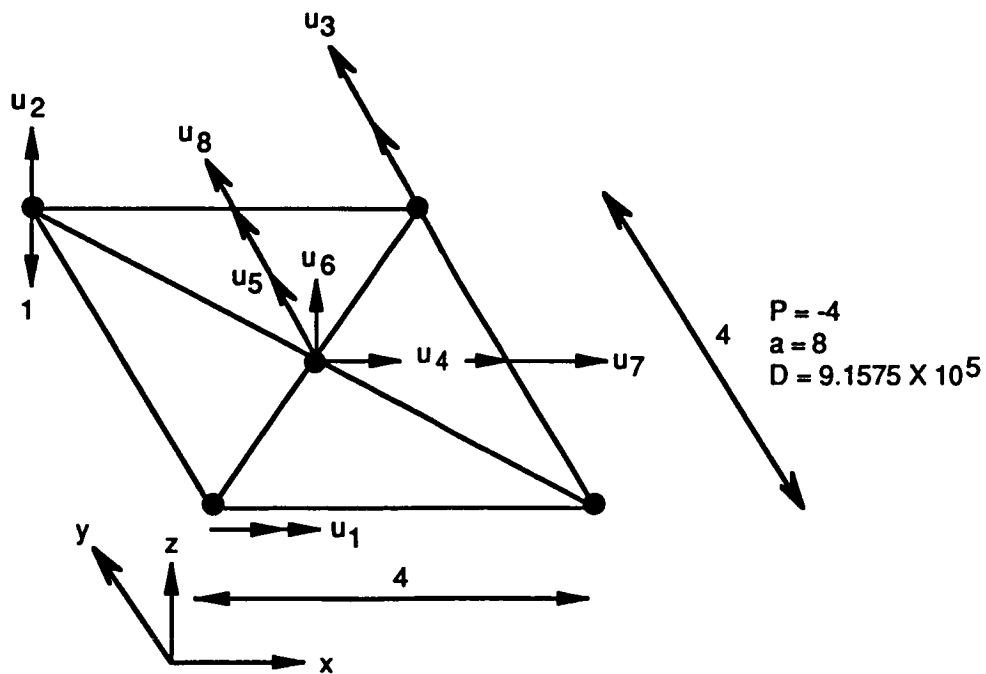


Figure 3.2-3 Square Plate Approximation Centrally Loaded

### TEST3 - Beam With Axial Enforced Displacement (Static)

A static analysis (Figure 3.2-4) is performed using Walker's viscoplastic material model with twelve loading increments. The properties of Hastelloy X at a temperature of 871°C (1600°F) are used, and the tip displacement is enforced at a strain rate of  $3.9 \times 10^{-3} \text{ sec}^{-1}$ . The computer program reproduces the experimental results. A plot of the stress-strain curve obtained from the output is shown in Figure 3.2-5.

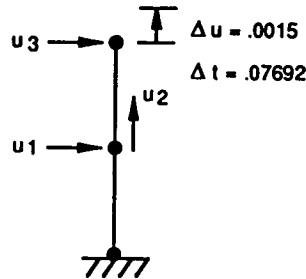


Figure 3.2-4 Schematic of TEST3

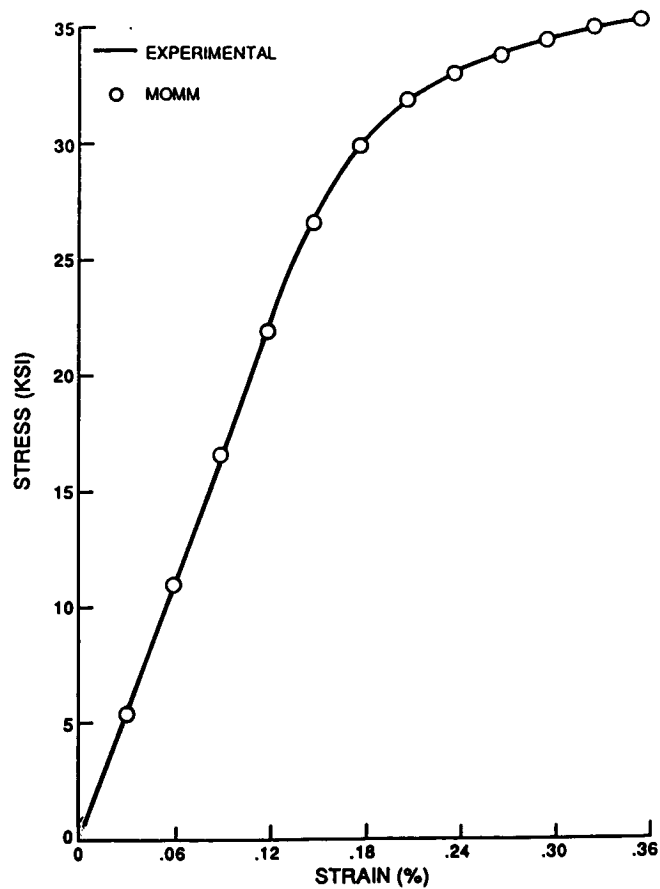


Figure 3.2-5 Stress-Strain Response for TEST3

## TEST4 and TEST5 - Beam With Axial Enforced Displacements (Transient)

Both test cases contain a beam fixed at both ends with a node in the middle of the beam (Figure 3.2-6). One end is displaced so that the strain rate equals  $3.9 \times 10^{-3} \text{ sec}^{-1}$ . A transient analysis is performed, with TEST4 containing Walker's viscoplastic material model and TEST5 containing the state-of-the-art material model. The viscoplastic material model uses the properties of Hastelloy X at a temperature of  $871^\circ\text{C}$  ( $1600^\circ\text{F}$ ). Figure 3.2-7 shows the displacement at the enforced displacement node, as well as the displacement at the center node versus time for each model. The results agree exactly with those obtained using a simple Euler integration.

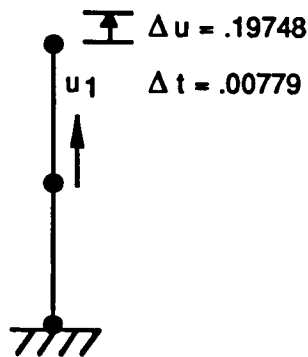


Figure 3.2-6 Schematic of TEST4 and TEST5

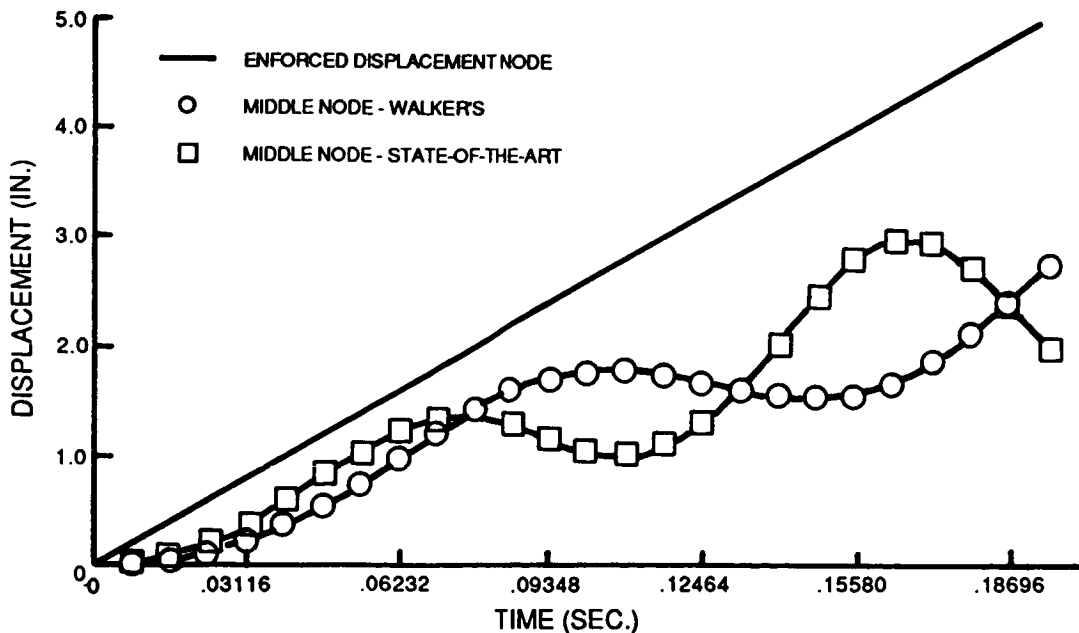


Figure 3.2-7 Displacement History for TEST4 and TEST5

## TEST6 - Beam With Crack

Cracks can be added to the structure at any point between beams and on any of the four faces of the cross section. The rules governing the input require that at the crack location, two grid points (GP2 and GP3) must be defined with identical coordinates. Since the crack is assumed to act at a nodal location, there is no length associated with the crack segment; therefore, the user must define a vector ( $v_x$ ) in the direction of the beam length (the element x-axis direction). The local y-axis must also be entered ( $v_y$ ) to define the element coordinate system. Other data input parameters include geometry set indicator, material set indicator, crack depth (D), and a parameter that indicates on which face of the cross section the crack exists. Multipoint constraint equations must be used to set all the degrees of freedom of the two grid points defining the crack (GP2 and GP3) equal to each other except for the axial and rotational degrees of freedom. The change in the axial and rotational degrees of freedom between the two grid points (GP2 and GP3) is solved for by using the crack stiffness and axial force and bending moment at the crack due to the loading on the structure (refer to Figure 3.2-8).

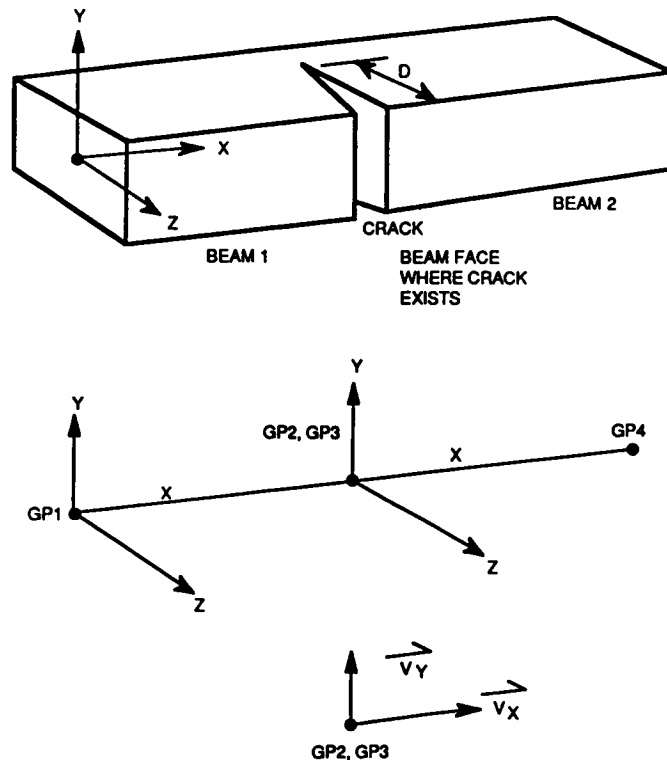


Figure 3.2-8 Schematic of Crack Simulation in Beam

A beam with a crack one-fifth through its thickness and subjected to a tensile load is analyzed. The beam is modeled with two elements. Note that the two grid points at the crack, node 2 and node 3, are assigned the same coordinates. Four multipoint constraint equations are input to set all but the axial and bending degree of freedoms equal at node 2 and node 3. Four multipoint constraint equations are input to set all but the axial and bending degree of freedoms equal at node 2 and node 3.

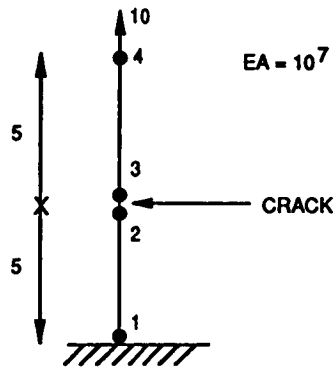


Figure 3.2-9 Schematic of TEST6 Beam

The simple material model was used, and the load is in the elastic range. The default value of two integration points in each direction of each beam is used.

The results show that the axial deflection at node 4, which would be  $1.0 \times 10^{-5}$  without a crack, is equal to  $1.0204 \times 10^{-5}$ . The stress intensity factor was found to be 10.931. Using an analytical expression for the stress intensity factor of a single-edged notch gives a value of 10.860.

The table below shows the comparison between the MOMM computer code results and analytical results for the stress intensity factor for different crack depths.

<u>Crack Depth</u>	<u><math>\kappa I</math></u> <u>(MOMM)</u>	<u><math>\kappa I</math></u> <u>(Analytical)</u>
.10	6.442	6.726
.15	8.738	8.855
.20	10.930	10.860
.25	13.374	13.382
.30	16.220	16.310
.35	19.623	19.818
.40	23.764	23.989
.45	28.916	29.249
.50	35.449	35.845

For this example, the value of the  $K^I$  calculated in the MOMM computer code agreed with the analytical result except when the crack depth was less than 0.10. In general, the user should be aware that the accuracy of the calculation of  $K^I$  will decrease when the crack depth is less than one-tenth the thickness of the beam.

### TEST7 - Beam With Transverse Hole

A beam with a transverse hole is loaded with a moment so that the bending is in the plane of the hole. The model consists of three beam elements end to end, with the middle beam containing the hole. The beam cross section is a 2x2 square, and the rectangular transverse hole is 1x1 square. The hole is input by setting the transverse hole thickness in the z-direction equal to one and the middle beam length equal to one. In order to capture the stress in the region of the hole, seven integration points in each direction are used in the middle beam. The simple material model was used, and the loading is elastic.

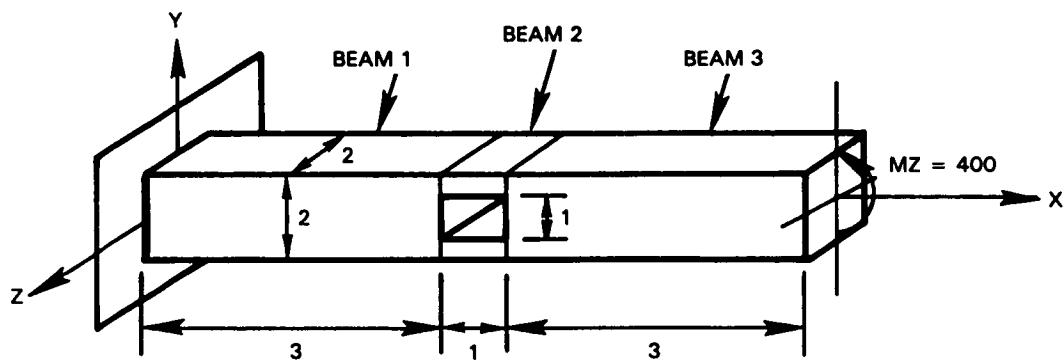


Figure 3.2-10 Schematic of TEST7 Beam

The displacements, strains and stresses are solved for, taking into account the reduced stiffness of the beam with the transverse hole. Interpolating using the stresses obtained at the integration points, the stress at the edge of the hole is found to be 171.4. The stress at the edge of the beam in the section of the hole is equal to 342.9. Stress concentration factors are printed out in the output for a circular hole with a diameter equal to the thickness of the rectangular hole. The in-plane bending stress concentration factor is equal to 2.0, and the stress at the edge of the hole should be multiplied by 2.0, i.e., the stress at the edge of the hole is equal to 342.9.

### 3.2.3 List of Symbols

#### List of Symbols Referenced Within Section 3.2

<u>Symbol</u>	<u>Description</u>	<u>Page</u>
{A}	Acceleration vector	30, 31
{ΔF}	Incremental force vector	30, 31
{V}	Velocity vector	30, 31
[M]	Mass matrix	30, 31
DT	Time step	30, 31
λ	Eigenvalue	31
[I]	Identity matrix	31
{x}	Eigenvector	31

### 3.2.4 Problems That Can Be Solved Using MOMEM

The following table presents problems that can be solved using MOMEM.

	Material Behavior		
	Simplified	Walker's Viscoplastic	State of the Art
Static Analysis	x	x	x
Transient Analysis	x	x	x
Lowest or All Frequencies	x	x	x
Lowest or All Mode Shapes	x	x	x
Buckling Factor	x	x	x
Buckling Mode Shape	x	x	x
Initial or Tangent Stiffness for Frequencies and Buckling	x	x	x
Applied Forces and Moments	x	x	x
Enforced Displacements	x	x	x
Thermal Loads	x	x	x
Cracks	x	x	x
Holes	x	x	x
Multipoint Constraints	x	x	x

Note: Buckling calculations cannot be performed in a transient problem.

### 3.3 SPECIAL FINITE ELEMENT MODEL

#### 3.3.1 Summary

The finite element code MHOST (MARC Hot Section Technology) has been further developed based on the mixed iterative solution technology whose concepts and basic hypotheses were defined in the first year effort. These concepts have been extended in the current phase to incorporate the effect of multiple embedded singularities in generic modeling regions. Specifically, a local mesh refinement technology has been generated based on the mixed element concept; the approach involves a supplemental iteration in conjunction with the introduction of a higher order polynomial representation for spatial discretization.

#### 3.3.2 Introduction

The mixed finite element approximation and its associated iterative solution algorithms have been developed for three-dimensional inelastic analyses with particular application to turbine engine hot section components. The numerical algorithms have been further improved in areas involving accuracy of solution and efficiency of computation.

The enhancement of solution capability has been sought in order to be able to deal effectively with problems involving multiple embedded singularities in generic modeling regions. The concept of subelement iteration has been derived and tested for the present purposes and its numerical performance is shown to be superior to that of the conventional finite element method.

The program development effort includes extensive testing of the capabilities built into the MHOST program as well as further enhancements to control the iterative procedure in a precise manner. An interface file is generated which can be handled by most commercially available finite element postprocessing packages.

In this section, a number of validation/verification problems are included to demonstrate the capability and the performance of the algorithms built into the MHOST program package.

### 3.3.3 Literature Survey

Reports, books and journal articles related to 'nonstandard' finite element methods have been surveyed with the main objective being the search for useful numerical technology in the framework of the mixed iterative solution approach.

In the past, 'nonstandard' finite element methods, such as the mixed and hybrid methods, have not been exploited in a systematic manner. The few exceptions generally involve hybrid elements for plate and shell analysis which generate element 'stiffness' equations or mixed elements for incompressible problems based on the Lagrangian functional used by Herrmann (Reference 1).

As documented in the First Annual Status Report (Reference 2) and in various research papers (References 3 through 6), iterative algorithms for generating continuous stress fields such as those developed by Cantin, Loubignac and Touzot (Reference 7) can be identified with the mixed finite element method. It is important to note that in constructing the iterative methods, use of the Hu-Washizu variational principle is crucial to setting up practical useful algorithms. In a recent paper (Reference 8), a similar observation was made and a finite element method was constructed from the Hu-Washizu principle with application to finite deformation plasticity.

Except for a few early papers such as those mentioned above and literature appearing after the present development effort was initiated, no directly relevant work has been published describing constructive iterative solutions for the mixed finite element equations derived from the Hu-Washizu form. There are, however, a number of papers indirectly relevant to and somewhat useful for further development of the solution strategy employed in the MHOST code.

The algorithm is viewed as composed of three steps. First, the linearized momentum equation is solved in terms of the displacement vector for preconditioning purposes. Second, the postprocessing algorithm is entered to generate the strain field based on the mixed interpolation which is used for the integration of the constitutive equation. Third, the equilibrium is iterated to satisfy the nonlinear virtual work equation with respect to the stress field interpolated in a mixed manner.

It should be noted that the quality of the displacement field generated by the preconditioner contributes significantly to the overall quality of the solution as well as the convergence characteristics. The use of equivalent stiffness in the element discontinuous strain mixed forms is a possible numerical strategy for these purposes (References 9 and 10). In particular, recent applications to plates and shells involving lower order element technology indicate possible improvements for the preconditioning operations (Reference 11), with further efficiency gained by using lower order quadratures (Reference 12).

The strain recovery algorithm based on the mixed interpolation is found to be virtually identical to the classical methodology based on the consistent conjugate stress distribution studied in References 13 and 14. Recent papers (References 15 and 16) present a systematic method to construct and analyze postprocessing algorithms. It is claimed that there are postprocessing procedures which provide accuracy for various quantities of the same order as that provided by the energy error estimate in finite element displacement algorithms. This statement agrees quite well with experimental observations by Owa (Reference 17) and Nakazawa, Owa and Zienkiewicz (Reference 18). Also, the super convergent results, in terms of stress and strain as well as displacement, often observed in the first year of this project may be due to the higher order convergence rate of the postprocessing algorithm used for the strain recovery computation. No literature is available on the effect of numerical quadrature in the postprocessing algorithms except a recent technical note by Simo and Hughes (Reference 19) on assumed strain involving the so-called B type algorithms for plates and shells.

Integration algorithms for nonlinear constitutive equations, in particular rate independent plasticity, are well-established as indicated in the Task I literature survey (Reference 20); and one of the most reliable algorithms, based on the radial return concept (Reference 21) has been implemented. No systematic effort has yet been reported on algorithm development for advanced viscoplastic constitutive models including temperature effects. Further literature search and original investigation is required in this field.

Methods of equilibrium iteration have been investigated in recent years and a number of useful papers and reports have appeared, as mentioned in the previous literature survey report. A survey and series of experiments (Reference 22) provide a useful collection of algorithms and numerical results with application to nonlinear plates. Basic algorithms for the Newton-Raphson and Modified- and quasi-Newton methods are compared in the displacement method framework. As demonstrated later in this section, algorithms discussed in a classical report by Matthies and Strang (Reference 23) are usable even in the context of the mixed iterative method.

The algorithms and convergence arguments directly applicable to the present framework are only available from literature on augmented Lagrangian methods for the quadratic minimization problem with linear equality constraints such as incompressibility and the Dirichlet boundary condition. Possible improvement of the iterative procedure is indicated in Reference 24, and the numerical test examples studied in References 25 and 5 show that significant improvement is obtained by using such algorithms for the analysis of Stokes' flow. Similar mathematical discussions and algorithms are also found in References 26 and 27. The original idea of the mixed iterative solution is, however, found in a historical work by Arron, Hurwicz and Uzawa (Reference 28) and the class of iterative algorithms for mixed problems is referred to as the Uzawa method.

In the context of linear elastic finite element analysis, the use of mixed approximations and equilibrium iterations has appeared in an ad hoc fashion repeatedly in the literature other than the work by Cantin, et al (Reference 7). For nonconforming plate bending elements, Crisfield (Reference 29) has

proposed an iterative algorithm to improve numerical accuracy. In the paper, the similarity of the concept (based on a modified Hellinger-Reissner principle) to the initial strain method iteration is pointed out. Also, an important observation by Crisfield is that all significant changes occur in the first iteration of the mixed process.

The implementation of mixed finite elements without an iterative solution is a topic that was extensively studied several decades ago, mainly with application to linear problems in mechanics as discussed in a survey by Zienkiewicz (Reference 30). These experiences have been used here to avoid possible numerical difficulties particular to this methodology. This is an important issue to be investigated. The characteristics of the particular algorithm used as the postprocessor needs to be understood in the mixed method framework, so as to fulfill the necessary conditions for stability and convergence. Regardless of the solution algorithm, the mixed method needs to satisfy the stability condition referred to as the Babuska-Brezzi condition in some sense (References 31 and 32). However, when equal order interpolations of displacement and stress are used, possible violation of this condition is indicated by Oden (Reference 33). Resultant oscillations of the numerical solution are indicated therein under special circumstances.

As experienced in mixed/penalty finite element computations for incompressible problems, however, the implication of the Babuska-Brezzi condition is not quite clear. For instance, as discussed in Reference 34, stability can be achieved by using a class of unstable elements which violates the condition a priori but which produces stable results by incorporating a postprocessing algorithm which satisfies the necessary condition for the stability.

Modern development of mixed finite element methods mainly involves constructing the displacement stiffness matrix from the element discontinuous approximation for additional variables (Reference 35). The derivation of this class of methods is based on the equivalence theorem stated in Reference 9. An important development along this line is a generalization of equivalence theorem proposed in Reference 36, indicating that for all numerically integrated displacement finite element methods, there exists an equivalent class of mixed

methods based on the Hu-Washizu principle. This observation provides some insights into the iterative process with particular application to inelastic problems. As mentioned earlier, these developments of 'reducible' mixed forms at the element level are useful mainly to construct the preconditioning system of equations as well as to fine tune the equilibrium iterations.

For the numerical modeling of singularities embedded in a structure, papers on fracture mechanics have been surveyed. For displacement finite element technology, the report by Fine (Reference 37) covers the technology to date. Except for a few efforts such as reported in Reference 38, not many papers and research reports are available discussing mixed and hybrid finite elements with application to fracture mechanics, in particular, nonlinear material problems. A paper by Babuska and Miller (Reference 16) on postprocessing to calculate the stress intensity factor was found useful for constructing and validating the numerical algorithm implemented into the MHOST program. The general strategy for numerical postprocessing is extended to deal with problems with singularities.

A series of papers (References 15 and 16) presents possible utilization of postprocessing technology and adaptive mesh refinement. The concepts are closely related to mixed iterative solution algorithms in conjunction with the subelement calculation as discussed later in this section. Literature on adaptivity and a posteriori error estimate (Reference 39) has been found useful in this line of development.

A series of notes by Axelsson (References 40 and 41) indicate the possible utilization of successive relaxation techniques for the solution of finite element equations, in particular, the mixed system of equations. However, no evidence that such algorithms can be used for nonlinear solutions is provided in those publications.

### 3.3.4 Formulation Strategy and Development

#### 3.3.4.1 The Global Solution Strategy

The nonlinear problem involving the inelastic response of a material body in an open, bounded domain  $\Omega$  with sufficiently smooth boundary  $\partial\Omega$  is presented in this section and an augmented form of the generalized nonlinear Hu-Washizu variational principle is derived in the infinitesimal deformation setting. A generic solution algorithm is constructed which is valid for quasi-static and dynamic-transient analyses.

The procedure discussed here represents a generalization of the algorithm developed in Task I of this project (Reference 2), and the resulting scheme can be combined with various solution algorithms and time integration operators other than the conventional Newton-Raphson and Newmark- $\beta$  methods.

The equilibrium equation is given by:

$$-\sigma_{ij,i} = \rho(f_j - a_j) \quad (3.3-1)$$

where  $\rho$  is the material density, assumed constant, with  $\underline{\sigma}$ ,  $\underline{a}$  and  $\underline{f}$  being the stress tensor, the acceleration vector and the body force vector respectively.

We assume a rate constitutive equation:

$$\dot{\sigma}_{ij} = (D_T)_{ijkl} \dot{\epsilon}_{kl} \quad (3.3-2)$$

with  $D_T$  being the tangent material modulus, and  $\dot{\underline{\sigma}}$  and  $\dot{\underline{\epsilon}}$  the stress and strain rates respectively. The strain tensor component is given by:

$$\epsilon_{ij} = \frac{1}{2} (u_{i,j} + u_{j,i}) + \epsilon_{ij}^0 \quad (3.3-3)$$

with  $\epsilon^0$  being the initial strain due to thermal expansion and creep effects. The usual equality constraints are imposed on the boundary such that:

$$u_k = \bar{u}_k \quad \text{on } \partial\Omega_1^{(k)} \quad (3.3-4)$$

and

$$t_k = \sigma_{kl} n_l = \bar{t}_k \quad \text{on } \partial\Omega_2^{(k)} \quad (3.3-5)$$

The weak variational form associated with the above problem statement is:

$$(\sigma_{ij}, u_{ij}^*) = (\rho(f_j - a_j), u_j^*) + \langle \bar{t}_k, u_k^* \rangle_{\partial\Omega_2^{(k)}} \quad (3.3-6)$$

$$\left( \bar{\epsilon}_{ij}, \left\{ \delta_{ij} - (D_T)_{ijkl} \epsilon_{kl} \right\} \right) = 0 \quad (3.3-7)$$

and

$$\left( \sigma_{ij}^*, \left\{ \epsilon_{ij} - \frac{1}{2} (u_{i,j} + u_{j,i}) \right\} \right) = \left( \sigma_{ij}^0, \epsilon_{ij}^0 \right) \quad (3.3-8)$$

where  $(.,.)$  denotes the usual  $L^2$  inner product over the domain  $\Omega$  and  $\langle ., . \rangle$  is the integral defined on the specific boundary, with \* indicating arbitrary variations.

Elimination of stress and strain from the above system of variational equations results in the virtual work equation in terms of displacement:

$$a(\underline{u}, \underline{u}^*) - (f, u^*) = 0 \quad (3.3-9)$$

with  $a(.,.)$  being the usual energy product. The essential boundary condition, equation (3.3-4), can be incorporated by virtue of the penalty approach:

$$a(\underline{u}, \underline{u}^*) - (f, u^*) + \epsilon^{-1} \langle u_k - \bar{u}_k, u_k^* \rangle_{\partial\Omega_1^{(k)}} = 0 \quad (3.3-10)$$

or equivalently:

$$\begin{aligned}
 & (\sigma_{ij}, u_{i,j}^*) + \epsilon^{-1} \langle u_k - \bar{u}_k, u_k^* \rangle_{\partial\Omega_1^{(k)}} \\
 & = (\rho(f_j - a_j), u_j^*) + \langle \bar{t}_k, u_k^* \rangle_{\partial\Omega_2^{(k)}}
 \end{aligned}
 \tag{3.3-11}$$

It can be shown that the simultaneous weak variational statements, equations (3.3-6) through (3.3-8), may be derived directly from the Hu-Washizu principle. This result implies that the boundary conditions, equations (3.3-4) and (3.3-5), enter into the system of equations only via the conservation law for linear momentum. In this setting, imposition of boundary conditions for the stress/strain mixed mode independent variables is unnecessary. If such conditions are applied, the well-posedness of the problem may be disturbed yielding an erroneous solution of possibly a rank deficient system of equations. In addition, the penalty approach involving the Dirichlet boundary condition does not require the space of admissible displacement variations to fulfill the homogeneous counterpart of the same condition.

Using an equal order interpolation function  $\underline{N}$  for all the variables involved in the analysis, we have:

$$u_k = N_M u_{Mk} \tag{3.3-12A}$$

$$a_k = N_M a_{Mk} = N_M \ddot{u}_{Mk} \tag{3.3-12B}$$

$$\epsilon_{ij} = N_M \epsilon_{Mij} \tag{3.3-12C}$$

$$\sigma_{ij} = N_M \sigma_{Mij} \tag{3.3-12D}$$

and for the input (initial) quantities:

$$f_k = N_M f_{Mk} \tag{3.3-12E}$$

$$\epsilon_{ij} = N_M \epsilon_{Mij}^0 \tag{3.3-12F}$$

resulting in a system of algebraic equations:

$$\begin{bmatrix} \tilde{P} & \tilde{0} & \tilde{B} \\ \tilde{0} & \tilde{D} & -\tilde{C} \\ \tilde{B}^T & -\tilde{C} & \tilde{0} \end{bmatrix} \begin{Bmatrix} \tilde{u} \\ \tilde{e} \\ \tilde{s} \end{Bmatrix} = \begin{Bmatrix} \tilde{F} & -\tilde{M} & \tilde{a} \\ \tilde{0} \\ \tilde{Q} \end{Bmatrix} \quad (3.3-13)$$

Denoting the  $L^2$  inner products over the domain by  $(\dots)$  and the surface integral by  $\langle \dots \rangle$ , the entries of matrices in equation (3.3-13) are:

$$P = \epsilon^{-1} \langle N^T, N \rangle$$

$$B = (\nabla N, N)$$

$$C = (N^T, N)$$

$$D = (N^T, D_T N)$$

$$M = \rho (N^T, N)$$

$$F = (N^T, f) + \langle N^T, t \rangle$$

and

$$Q = (N^T, \epsilon_0)$$

Note that, for the sake of simplicity, the time integrated form of the rate constitutive equation is assumed. The details of the incremental process and the stress recovery are discussed later in this section. Elimination of the nodal strains and stresses leads to a 'displacement' solution form:

$$\left\{ \begin{matrix} \tilde{B}(\tilde{C})^{-1} & \tilde{D}(\tilde{C}^T)^{-1} & \tilde{B}^T & + & \tilde{P} \end{matrix} \right\} \tilde{u} = \hat{\tilde{F}} - \tilde{M} \tilde{a} \quad (3.3-14)$$

with

$$\hat{\underline{F}} = \underline{F} + \underline{B}(\underline{C})^T \underline{D}(\underline{C}^T)^{-1} \underline{Q}, \quad (3.3-15)$$

whereas the standard finite element result based on equation (3.3-9) is approximated by a somewhat simpler form:

$$(\underline{K} + \underline{P}) \underline{u} = \underline{F} - \underline{M} \underline{a} + \underline{Q}', \quad (3.3-16)$$

with  $\underline{Q}'$  being the nodal force generated by the initial strain in the structure.

An iterative solution algorithm for the quasi-static counterpart of equation (3.3-13) can be constructed as follows:

- (a) Set a vector  $\underline{R} = 0$ ; initialize the displacement vector  $\underline{u} = 0$
- (b) Solve the preconditioning equations to update the displacement such that:

$$\underline{u} = \underline{u} + \underline{A}^{-1} (\hat{\underline{F}} - \underline{R}) \quad (3.3-17)$$

- (c) Recover the nodal strain:

$$\underline{e} = (\underline{C}^T)^{-1} (\underline{B}^T \underline{u} - \underline{G}) \quad (3.3-18)$$

- (d) Integrate the constitutive equation:

$$\underline{\sigma} = \int_{t^*} \underline{D}_T \dot{\underline{e}} dt^* \quad (3.3-19)$$

with  $t^*$  being the quasi-time associated with deformation history.

(e) Evaluate the residual:

$$\tilde{R} = \tilde{B}^T \tilde{s} \quad (3.3-20)$$

(f) If the residual is small enough, then exit; or else repeat from step (b).

As is obvious from the above discussion, the choice of the preconditioner  $\tilde{A}$  is crucial in obtaining convergence characteristics necessary for a practical implementation. For instance, if:

$$\tilde{A} = \tilde{B}(\tilde{C})^{-1} \tilde{D}(\tilde{C}^T)^{-1} \tilde{B}^T + \tilde{P}, \quad (3.3-21)$$

then no iteration is needed. However, sparseness properties of the finite element system matrix could no longer be exploited if the above form were to be utilized. As a reasonable compromise, we use the equilibrium equation involving an augmented displacement stiffness matrix which is set to:

$$\tilde{A} = \tilde{K} + \tilde{P}. \quad (3.3-22)$$

Other methods of preconditioning have been investigated, but so far no robust scheme is known to be applicable for a wide range of solid and structural analyses (Reference 42). Except for minor modifications, the present solution utilizes the form defined by equation (3.3-22).

#### 3.3.4.2 Incremental Iterative Solution Algorithms

The inelastic problem is solved through the deformation history in an incremental manner. Let the solution for a given state of displacement, strain and stress which satisfies the nonlinear algebraic equation (3.3-13) for specified load and displacement boundary conditions be identified by  $\underline{u}^n$ ,  $\underline{e}^n$ ,  $\underline{s}^n$ , and  $\underline{F}^n$ , respectively. Then for a given load increment,  $\Delta \underline{F}^n$ , the increments of displacement, strain and stress denoted by  $\Delta \underline{u}^n$ ,  $\Delta \underline{e}^n$ , and  $\Delta \underline{s}^n$  are determined in an iterative fashion as described in the previous section. Note

that the tangent stiffness  $\underline{K}_T$  is used instead of the total stiffness equation in the preconditioning process. To follow a complicated equilibrium path, an automatic adjustment procedure which controls the size of the load increment in the iterative process is available. The algorithm in outline form is:

- (a) Set the residual vector  $R = 0$ , initialize the incremental displacement vector  $\Delta u^n = 0$ . If the first increment, initialize the total load factor  $\lambda$ .

- (b) Project the displacement by:

$$\tilde{d}u = \tilde{K}_T^{-1} \hat{F} \quad (3.3-23)$$

and if it is the first cycle of iteration, calculate the arc length and initialize the incremental load factor ( $\Delta\lambda$ ) and  $d\lambda$ . The arc length  $\ell$  is defined by:

$$\ell = (du)^{1/2}$$

and the incremental load factor is given by solving the quadratic equation for the iterative load change. Then, carry out the back substitution to get:

$$\tilde{d}\bar{u} = \tilde{K}_T^{-1} (\lambda \hat{F} - R) \quad (3.3-24)$$

- (c) Update the displacement vector:

$$\Delta u = \Delta u + \tilde{d}\bar{u} + d\lambda \tilde{d}u \quad (3.3-25)$$

(d) Find the total load factor update:

$$\lambda = \lambda + d\lambda \quad (3.3-26)$$

and the incremental load factor:

$$\Delta\lambda = \Delta\lambda + d\lambda \quad (3.3-27)$$

based on the spherical path formulation (Reference 43).

(e) Form the residual vector in the mixed manner [equations (3.3-18 through 3.3-20)] and then check the convergence. If convergent, start the next increment; or else repeat step (b).

Figure 3.3-1 presents a flow chart for this algorithm, and further details regarding this process will be included in the MHOST Theoretical Manual. In the mixed method, steps which generate the residual force are treated as a package of operations. Any iterative method designed to improve convergence characteristics can be employed. For instance, the BFGS update procedure (Reference 23) is utilized in the following fashion:

(a) Initialize the residual vector  $\underline{R}$  and the incremental displacement  $\Delta\underline{u}$  such that:

$$\underline{R} = 0; \quad \Delta\underline{u} = 0 \quad (3.3-28)$$

(b) Modify the residual with  $i$  being the iteration counter:

$$\underline{R} = \left\{ \prod_{j=2}^i (\underline{I} + \underline{v}_j \underline{w}_j^T) \right\} \underline{R} \quad (3.3-29)$$

(c) Intermediate displacement update:

$$\underline{d\bar{u}} = \underline{K_T}^{-1} \underline{\bar{R}} \quad (3.3-30)$$

where  $\underline{K_T}^{-1}$  is the latest stiffness matrix factorized in the current increment. The BFGS iteration counter is set to 1 when the factorization is performed.

(d) Complete the displacement update:

$$\underline{du} = \left\{ \prod_{j=2}^i (I + \underline{w}_j \underline{v}_j^T) \right\} \underline{d\bar{u}} \quad (3.3-31)$$

(e) Form the new incremental displacement:

$$\underline{\Delta u} = \underline{\Delta u} + \underline{du} \quad (3.3-32)$$

(f) Form the new residual with respect to the updated incremental displacement using equations (3.3-18) through (3.3-20).

(g) Check convergence and, if necessary, repeat from step (b) or else, exit.

Note in the above algorithm, vectors  $\underline{v}_i$  and  $\underline{w}_i$  represent the iterative changes in the residual and displacement vectors respectively so as to form the inverse BFGS update:

$$[\underline{K_{Ti}}]^{-1} = \left( I + \underline{w}_i \underline{v}_i^T \right) [\underline{K_{Ti-1}}]^{-1} \left( I + \underline{v}_i \underline{w}_i^T \right) \quad (3.3-33)$$

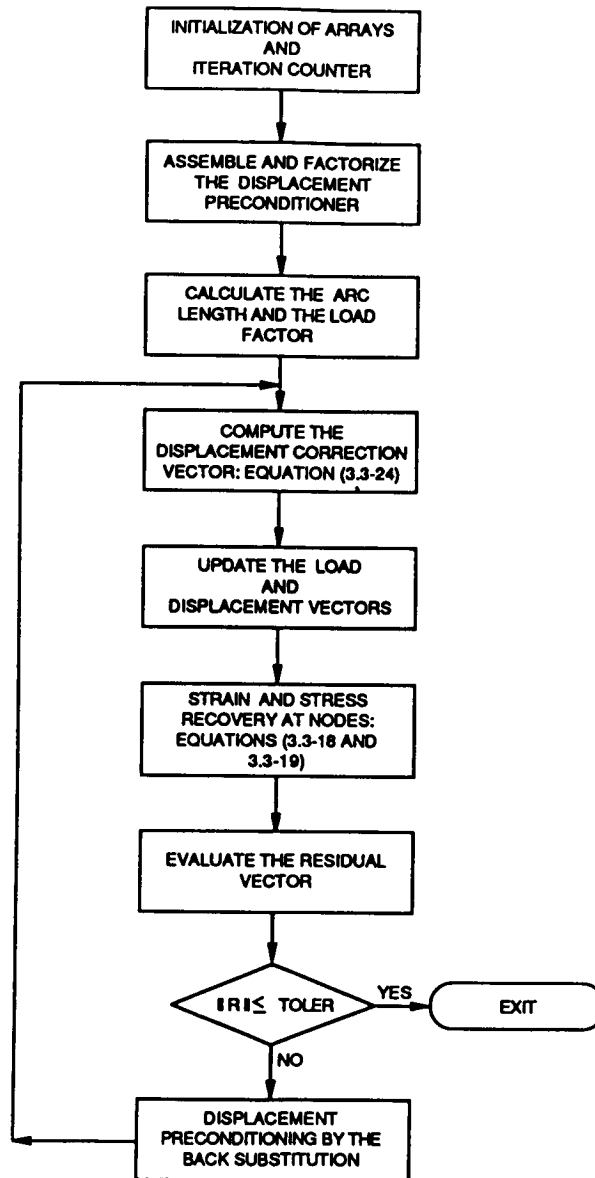


Figure 3.3-1 The Arc-Length Method for the Mixed Iterative Solution

Figure 3.3-2 presents a flow chart for the BFGS procedure. It is possible to introduce combined BFGS - arc length algorithms in the mixed iterative solution algorithms incorporating a line search technique. The applicability of such advanced techniques requires further investigation.

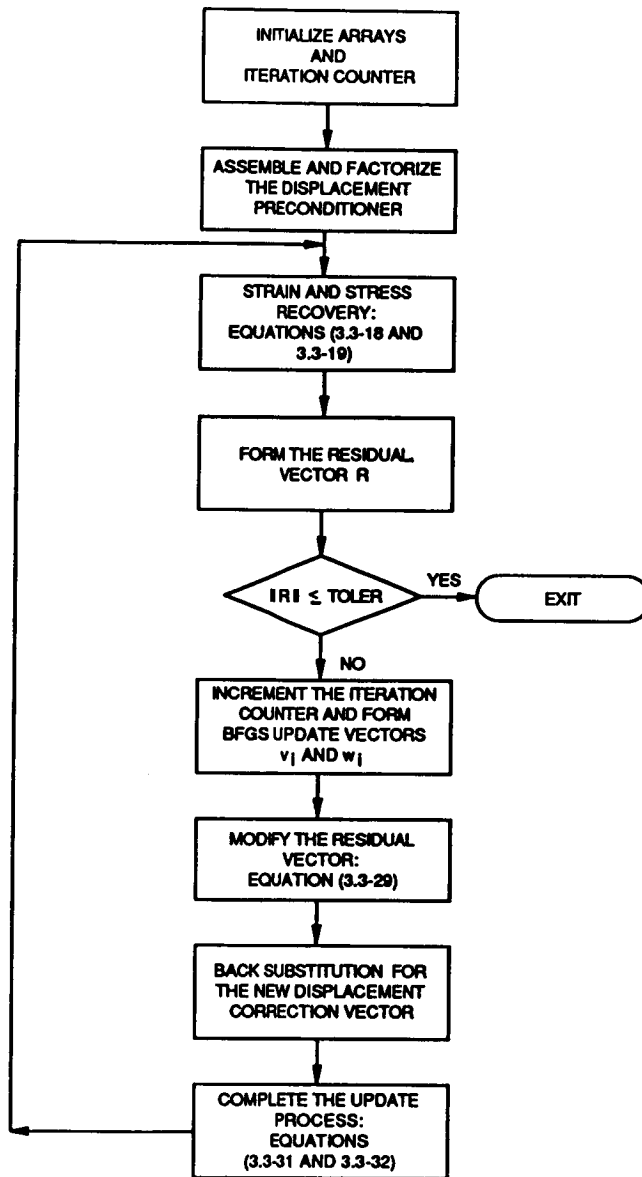


Figure 3.3-2 The Inverse BFGS Update for the Mixed Iterative Solution

### 3.3.4.3 Construction of the Stiffness Equations

A number of different element based integration schemes are implemented into the MHOST numerical solution procedures. To achieve stability and coarse mesh accuracy in the finite element solution, not all the terms in the equations are integrated at the nodes. Two-point Gauss quadrature is used for evaluation of the stiffness coefficients and the internal force vector in each coordinate direction. A nodal quadrature (element discontinuous trapezoidal integration) is used in the strain recovery operations, and all the stress components are evaluated at the global nodes.

To extract near optimal numerical performance of the elements implemented in the MHOST code, a selective reduced integration option is available in which the shear strain components are evaluated at the internal element centroid.

All the integration procedures are internal operations designed to generate an accurate finite element solution and are invisible to the user as results are reported primarily at the nodes.

Two major refinements have been incorporated into the MHOST program to ensure the generation of a good displacement update for preconditioning purposes. These are an improved version of the filtering scheme for selectively reduced integration and a modified numerical quadrature for plates and shells which avoids possible kinematic mode excitation.

#### Coordinate Transformation and Filtering Algorithms

With application to general two- and three-dimensional elements, a method is developed for construction of the element coordinate system and its utilization to filter particular strain components for the selectively integrated stiffness equations. A nonstandard notation is used to maintain maximum possible generality in the following discussions. Whenever indicial notation is applied, the summation convention is assumed for repeated indices unless otherwise stated.

In this section, we first establish the coordinate systems used in the isoparametric finite elements. In particular, the local (pointwise) definition of the orthogonal system associated with the Jacobian matrix is presented based on the theory of polar decomposition, and this definition is used later to devise a family of filtering algorithms for the element strain components. The deformation tensors associated with the Jacobian matrix are used as a basis for constructing the measure of isoparametric distortion. The filtering scheme is constructed from strain tensor components with particular application to selectively reduced integration to avoid possible numerical locking and further to improve the accuracy of finite element displacement type solution procedures.

Consider a linear isoparametric element in two dimensions. We denote the global coordinates fixed in physical plane by  $\underline{x} = (x^1, x^2)$  and the isoparametric coordinates in the reference plane by  $\underline{q} = (q^1, q^2)$ . The notation and the results which follow are readily extended to general three-dimensional elements.

We denote the Jacobian matrix by  $\underline{J}$ , which is defined by:

$$\underline{J} = [J^k_K] \quad (3.3-33)$$

where

$$J^k_K = x^k_{,K} = \partial x^k / \partial q_K \quad (3.3-34)$$

By definition the Jacobian is invertible and for any invertible linear transformation there exists a decomposition, known as the polar decomposition such that:

$$\underline{J} = \underline{R} \underline{U}, \quad (3.3-35)$$

where  $R$  is the orthogonal rotation tensor and  $U$  is a symmetric, positive-definite matrix often referred to as the right stretch tensor. In the present setting, the rotation tensor represents the orientation of the physical coordinate system with respect to the orthogonal basis associated with the isoparametric coordinates in physical space. Hence, its inverse gives the basis vectors for the orthogonal coordinates parallel to the element orientation.

The computational procedure to obtain  $R^{-1}$  is to utilize the relation:

$$J^T J = U^T U, \quad (3.3-36)$$

as demonstrated in Reference 44 among several others, together with the decomposition, equation (3.3-35):

$$R = J U^{-1} \quad (3.3-37)$$

The inverse of the right stretch tensor is obtained from the eigenvalues and eigenvectors of the right Cauchy-Green tensor  $C$  which is defined as:

$$C = J^T J. \quad (3.3-38)$$

Hence,

$$U^{-1} = \underset{C}{-1/2} = N_C^T \lambda_C^{-1/2} N_C \quad (3.3-39)$$

with  $\lambda_C$  and  $N_C$  being the eigenvalues and eigenvectors, respectively, arranged in matrix forms. Hence, the equation used in the actual computation is:

$$R = J N_C^T \lambda_C^{-1/2} N_C. \quad (3.3-40)$$

The purpose of selective integration is to avoid numerical locking due to the overestimation of certain element deformation modes as illustrated in Reference 34. This is realized by integrating the contribution of strain energy associated with the strain components characterizing such deformation modes at the reduced integration points. The strain components to be under-integrated are not defined in the global coordinate system but in the coordinate system parallel to the element orientation given by the rotation tensor  $R$  discussed above.

Let  $e_{ij}^{(kl)}$  be the global Cartesian tensor associated with the  $kl^{\text{th}}$  strain tensor component in the local coordinate system. Denoting the coordinate transformation matrix by  $g$  such that:

$$g = [g_m^k] = R^{-1} \quad (3.3-41)$$

where the superscript and the subscript denote the local and the global coordinates, respectively. Then we have:

$$e_{ij}^{(kl)} = g_i^k g_j^l \epsilon^{kl} = g_i^k g_j^l g_m^k g_n^l \epsilon_{mn}. \quad (3.3-42)$$

Introducing an array  $G$  referred to as the filtering matrix such that:

$$G_{ij}^k = g_i^k g_j^k \text{ (no sum on } k), \quad (3.3-43)$$

we simplify the above expression as:

$$\epsilon_{ij}^{(kl)} = G_{im}^k G_{jn}^l \epsilon_{mn} \quad (3.3-44)$$

Hence, the volumetric strain in the element coordinate system is given in terms of the global strain components by:

$$\epsilon_{ij}^{(v)} = G_{im}^k G_{jn}^l \delta^{kl} \epsilon_{mn} \quad (3.3-45)$$

and the deviatoric strain by:

$$\epsilon_{ij}^{(D)} = G_{im}^k G_{jn}^l (1 - \delta^{kl}) \epsilon_{mn} \quad (3.3-46)$$

where  $\delta^{kl}$  is the Kronecker delta.

Defining the original strain component  $e$  by:

$$e = B u, \quad (3.3-47)$$

where  $B$  is the usual strain-displacement matrix calculated at the quadrature points and  $u$  is the nodal displacement vector, the energy functional  $I(u)$  is obtained in terms of nodal displacement for linear elasticity as an example by,

$$I(u) = \int_{\Omega} \lambda e^{(v)} : e^{(v)} dx + \int_{\Omega} \mu e^{(D)} : e^{(D)} dx - \int_{\Omega} f \cdot u dx - \int_{\partial\Omega} T \cdot u ds \quad (3.3-48)$$

where : denotes tensor inner products,  $\lambda$  and  $\mu$  are the Lamé-Navier coefficients and  $f$  and  $T$  are the prescribed body force and surface traction respectively.

In the above energy functional, either the first term or the second term is under-integrated to obtain the necessary effects of the selectively reduced integration.

In computations, it is often more convenient to construct the strain-displacement matrix selectively, so that the above energy functional can be written as:

$$I(u) = u^T \int_{\Omega} B_S^T D B_S dx u - F^T u \quad (3.3-49)$$

where  $F$  is the collection of prescribed load terms which appeared in equation (3.3-48). The new strain-displacement matrix  $B_S$  is the selectively sampled matrix equivalent to a certain mixed method under isoparametric distortion. In matrix notation, the filter for the element volumetric strain is written as:

$$e^{(v)} = G^T I G B u \quad (3.3-50)$$

and for the element deviatoric strain:

$$e^{(D)} = G^T (1 - I) G B u \quad (3.3-51)$$

at each integration point, where  $1$  and  $I$  are the matrices:

$$1 = [1] ; I = [\delta_{ij}] . \quad (3.3-52)$$

Hence, we have:

$$B_S = G^T I G B + G^T (1 - I) G B \quad (3.3-53)$$

where either the first or the second term is sampled at the reduced integration points and substituted to the array associated with the full integration points. Such an operation is trivial only for the linear Lagrangian elements with a single reduced integration point.

## Hourglass Control Algorithm for Plates and Shells

The kinematic model generated by the reduced integration of transverse shear terms in 4-noded bilinear plate and shell elements often induces numerical noise in the displacement preconditioning operation. However, excitation of these modes, often referred to as the hourglass modes, does not cause significant deterioration in the convergence of the mixed iterative algorithms. To eliminate these modes, filtering methods have been developed either to constrain the modes by modifying the stiffness equation (a priori hourglass control) (Reference 45) or to filter out the spurious noise after the nodal displacement is obtained (a posteriori hourglass control) (Reference 46).

A simplified a priori hourglass control algorithm based on an approach similar to the scheme proposed in Reference 47 has been implemented into the MHOST code. The algorithm takes advantage of the fact that the fully integrated stiffness matrix (2x2 integration) does not contain kinematic modes.

The transverse shear stiffness matrix  $\underline{K}_S$  is constructed as follows:

$$\underline{K}_S = \epsilon \underline{K}_S^{(2x2)} + (1 - \epsilon) \underline{K}_S^{(1x1)} \quad (3.3-54)$$

where  $\epsilon$  is a small parameter associated with the aspect ratio of the element. Numerical locking is avoided due to the insignificant participation of the fully integrated terms.

The value for  $\epsilon$  is calculated at the centroid of the element using the formula:

$$\epsilon = \epsilon_0 t_c / h \quad (3.3-55)$$

where  $t_c$  is the thickness of the element at the centroid and  $h$  is the mesh size given by:

$$h = \frac{1}{2} (|x_1 - x_4| + |x_2 - x_3|). \quad (3.3-56)$$

Typically a value of 0.01 for  $\epsilon_0$  has been used for the validation and verification exercises.

No additional computational cost is involved in this hourglass control algorithm because the element stiffness equations are integrated selectively and, hence,  $\tilde{K}_S^{(2 \times 2)}$  is available without adding a new integration procedure.

#### 3.3.4.4 Time Integration Algorithm

The basic temporal discretization procedure is virtually identical to the quasi-static solution of the mixed finite element equations. The system of ordinary equations:

$$\tilde{M} \ddot{\tilde{u}} = \tilde{I}(\tilde{u}) \quad (3.3-57)$$

where  $\tilde{I}$  is the nonlinear function of nodal displacements and is discretized in time resulting in a recursive form for updating  $u$  such that:

$$\tilde{A}^t \tilde{u}^{t+\Delta t} = \tilde{B}^t(\tilde{u}^t) \quad (3.3-58)$$

where  $\tilde{A}$  and  $\tilde{B}$  are the linearized versions of the time integration operator matrices. The final goal here is to use formula (3.3-58) iteratively as the preconditioner to find a displacement vector and its time derivatives which satisfy:

$$\tilde{M} \ddot{\tilde{u}}^{t+\Delta t} = \tilde{I}(\tilde{u}^{t+\Delta t}). \quad (3.3-59)$$

The generalized Newmark- $\beta$  method is used to construct the iterative solution algorithm. The semi-discrete approximation yields a set of nonlinear ordinary differential equations:

$$Ma + Cv + \int_{\Omega} B^T \sigma \, dx = F, \quad (3.3-60)$$

where the third term on the left-hand side is the integral associated with the strain energy, and for elasticity we can write:

$$\int_{\Omega} B^T \sigma \, dx = K u . \quad (3.3-61)$$

Otherwise, the deformation history needs to be integrated for evaluating this term. The mass matrix is defined in terms of the nodal basis functions, and mass density is designated by the symbol  $\rho$ :

$$M = \int_{\Omega} \rho N^T N \, dx \quad (3.3-62)$$

One of the possible forms for the damping matrix is to express it in terms of the mass and stiffness matrices as follows:

$$C = c_1 M + c_2 K . \quad (3.3-63)$$

Based on the weighted residual argument of Zienkiewicz (Reference 30), the generalized form of the Newmark- $\beta$  algorithm is written in a recursive manner as:

$$u^{t+\Delta t} = u^t + \Delta t v^t + \frac{\Delta t^2}{2} \left\{ (1 - 2\beta) a^t + 2\beta a^{t+\Delta t} \right\} \quad (3.3-64A)$$

$$u^{t+\Delta t} = v^t + \Delta t \left\{ (1 - \gamma) a^t + \gamma a^{t+\Delta t} \right\} \quad (3.3-64B)$$

where  $t$  indicates the current time (known) and  $\Delta t$  is the current time increment.

The overall equilibrium at the next time level is:

$$M a^{t+\Delta t} + C v^{t+\Delta t} + \int_{\Omega} B^T \sigma (u^{t+\Delta t}) \, dx = F^{t+\Delta t} . \quad (3.3-65)$$

Approximating the energy term linearly yields:

$$\int_{\Omega} B^T \sigma (u^{t+\Delta t}) \, dx = K^* \Delta u + \int_{\Omega} B^T \sigma (u^t) \, dx \quad (3.3-66)$$

where  $K^*$  is the tangent stiffness matrix which shall be considered later. Equilibrium at the current time level:

$$M a^t + C v^t + \int_{\Omega} B^T \sigma(u^t) dx = F^t$$

implies that:

$$\int_{\Omega} B^T \sigma(u^{t+\Delta t}) dx = K^* \Delta u + F^t - (M a^t + C v^t) . \quad (3.3-67)$$

Substituting equation (3.3-67) into (3.3-65), we have the following incremental equilibrium form, where  $\Delta u$  is the displacement increment associated with  $\Delta t$ :

$$M a^{t+\Delta t} + C v^{t+\Delta t} + K^* \Delta u = \Delta F^* + (M a^t + C v^t) . \quad (3.3-68)$$

From equations (3.3-64A) and (3.3-64B):

$$a^{t+\Delta t} = \frac{1}{\beta \Delta t^2} \Delta u - \frac{1}{\beta \Delta t} v^t - \left(\frac{1}{2\beta} - 1\right) a^t \quad (3.3-69A)$$

$$v^{t+\Delta t} = \frac{\gamma}{\beta \Delta t} \Delta u - \left(1 - \frac{\gamma}{2\beta}\right) v^t + \Delta t \left[ \left(1 - \gamma\right) - \gamma \left(\frac{1}{2\beta} - 1\right) \right] a^t . \quad (3.3-69B)$$

Substituting the above, equations (3.3-69A) and (3.3-69B), yields a linearized algebraic system of equations:

$$\left[ \frac{1}{\beta \Delta t^2} M + \frac{\gamma}{\beta \Delta t} C + K^* \right] \Delta u = \Delta F^* + (M a^t + C v^t) + M \left\{ \frac{1}{\beta \Delta t} v^t + \left(\frac{1}{2\beta} - 1\right) a^t \right\} + C \left\{ \left(1 - \frac{\gamma}{2\beta}\right) v^t - \Delta t \left[ \left(1 - \gamma\right) - \gamma \left(\frac{1}{2\beta} - 1\right) \right] a^t \right\} \quad (3.3-70A)$$

which we write simply as:

$$\hat{K} \Delta u = \hat{F} \quad (3.3-70B)$$

Now, we shall recast the above algorithm in the mixed iterative framework. First, the conventional Newton-Raphson scheme is constructed in the context of the displacement calculation:

$$\Delta u_{n+1} = \Delta u_n + \hat{K}_n^{-1} (\hat{F} - \hat{R}_n) \quad (3.3-71)$$

with  $\hat{R}_n$  being the residual at nth iteration cycle defined by:

$$\hat{R}_n = \int_{\Omega} B^T \left\{ s^t + \Delta s (\Delta u^n) \right\} dx - \left\{ M a^{t+\Delta t} + C v^{t+\Delta t} \right\}. \quad (3.3-72)$$

The updated values for acceleration and velocity vectors in equation (3.3-72) are calculated from the formulae (3.3-69A) and (3.3-69B) using the latest update for incremental displacements. The mixed interpolations for stresses are used in place of total and incremental stress arrays in the first term of equation (3.3-72). The computation is accomplished in exactly the same manner as in the quasi-static incremental iterative analysis.

Introducing a new variable  $d_n$ :

$$d_n = K^{-1} (\hat{F} - \hat{R}_n), \quad (3.3-73)$$

the iterative update of the velocity and acceleration is written as:

$$a_{n+1}^{t+\Delta t} = a_n^{t+\Delta t} + \frac{1}{\beta \Delta t^2} d_n \quad (3.3-74A)$$

$$v_{n+1}^{t+\Delta t} = v_n^{t+\Delta t} + \frac{\gamma}{\beta \Delta t} d_n \quad (3.3-74B)$$

with the starting values:

$$a_0^{t+\Delta t} = -\frac{1}{\beta \Delta t} v^t - \left(\frac{1}{2\beta} - 1\right) a^t \quad (3.3-74C)$$

$$v_0^{t+\Delta t} = -\left(1 - \frac{\gamma}{2\beta}\right) v^t + \Delta t \left[\left(1 - \gamma\right) - \gamma \left(\frac{1}{2\beta} - 1\right)\right] v^t \quad (3.3-74D)$$

calculated at the beginning of each time increment.

Note that the load vector  $\hat{F}$  is left unchanged throughout the iteration.

### 3.3.4.5 Eigenvalue Extraction for Modal and Buckling Analysis

The eigenvalue extraction procedure in the MHOST program utilizes a standard subspace iteration method to obtain the natural vibration frequencies and the buckling load at a given quasi-static load step. The band matrix solver is used to factorize the global stiffness equations prior to the subspace iterations. In the subspace, the Jacobi method is used to extract all the eigenvalues and eigenvectors.

For a modal analysis, the consistent mass matrix is formed including the rotational inertia terms for shell elements. The generalized mass is calculated and reported in conjunction with the eigenvalues and eigenvectors.

In a buckling analysis, the initial stress matrix is calculated from the nodal stress resulting from the mixed iterative solution for the initial quasi-static loading. The displacement stiffness equations are used to represent the structural model in the eigenvalue analyses. However, the accurate representation of the initial stress terms improves the overall accuracy of the buckling load estimates.

### 3.3.4.6 Subelement Iterations

Computational fracture mechanics aspects of the inelastic analysis of turbine engine hot section components are discussed in this section. The motivation for this endeavor is to seek an economically feasible numerical process without sacrificing the accuracy of the solution.

The standard finite element method is to take into account the effect of embedded singularities by refining the mesh subdivision in the neighborhood of such points, or alternatively to introduce special elements with singular functions in this neighborhood. The currently available approaches are often prohibitively expensive, especially when the analysis involves a structure with multiple singularities, each of which needs special treatment.

The use of nonstandard schemes, in particular the mixed finite element form, is accurate and stable, and appears to be far more advantageous when compared with conventional schemes in regular nonlinear structural analysis. Hence, utilization of nonstandard schemes for problems including singularities is worth investigating to see if a major improvement in computational fracture mechanics can be realized.

The main reason for using the mixed finite element method in problems with embedded singularities is that higher resolution for stresses and strains can be obtained without excessive mesh refinement for the displacement variables near the singularities.

In the framework of the displacement finite element method, the only information primarily available from the computation provides the nodal displacements from which the strain/stress components are calculated by differentiating the shape functions. The stress/strain values are then used to determine fracture mechanics related quantities such as the stress intensity factor and the J-integral.

It is clear then that the accuracy of the strain/stress components is a full one order less than that of the displacement components for the displacement finite element method, even without a singularity. Moreover, the approximation of strains/stresses could be extremely unstable near singularities, as well as in regions where the deformation is highly concentrated. To obtain accurate results for a problem with embedded singularities by the standard displacement technology, mesh refinement near singularities is unavoidable in order to be able to determine an accurate and stable displacement field, which indeed is the only source for generating the strain/stress approximations. For the best possible results, monitoring an a posteriori error indicator, together with several passes of (adaptive) mesh refinement are advisable in such calculations.

When the strains or stresses, sometimes both, are included explicitly in the finite element system of equations, in particular interpolated by  $C^0$ -continuous basis functions, the resulting approximations are not only accurate but also stable, having no spurious modes in the strain/stress recovery operator.

For regular problems, the numerical representation of the stress field in particular is quantitatively accurate due to the equilibrium condition being explicitly satisfied by the approximate stress field itself. Compared with displacement method results, a full one order improvement is indeed expected of the convergence rate in the mixed method for the same mesh subdivision. It should be noted that the role of the displacement solution in the mixed form is to generate qualitatively the deformation mode from which indirectly the deformation gradient is extracted and fed into the stress recovery and equilibrium iteration operations. Therefore, the quantitative measure of error in the displacement vector contributes relatively less significantly to the overall error in calculating fracture related quantities.

The approximate solution procedure for a deformable body with embedded singularities involves first solving the total structural problem without the singularities; this step shall be specifically referred to as the global system approach. The second step then computes the deformation and the stresses near the singularity based on the first step results and is called the local system approach. The concept is somewhat similar to substructuring in conventional finite element computations. In Figure 3.3-3, the hierarchical structure of the mesh subdivision and subelement representations is illustrated.

Assume that P in Figure 3.3-3(a) is a singularity embedded in the structure the size of which is small compared with the scale of the whole structure. Typically, the conventional finite element representation needs a quite fine mesh for such a situation. Figure 3.3-3(b) is an example of a reasonable mesh subdivision to represent the global behavior of the structure. In this model, the singularity is still embedded in an element, but not explicitly considered in the numerical model. This model is referred to as the global finite element mesh.

The subelement mesh subdivision is shown in Figure 3.3-3(c) where the element with an embedded singularity is subdivided further down to the scale of the singularity and its effect is now evaluated explicitly.

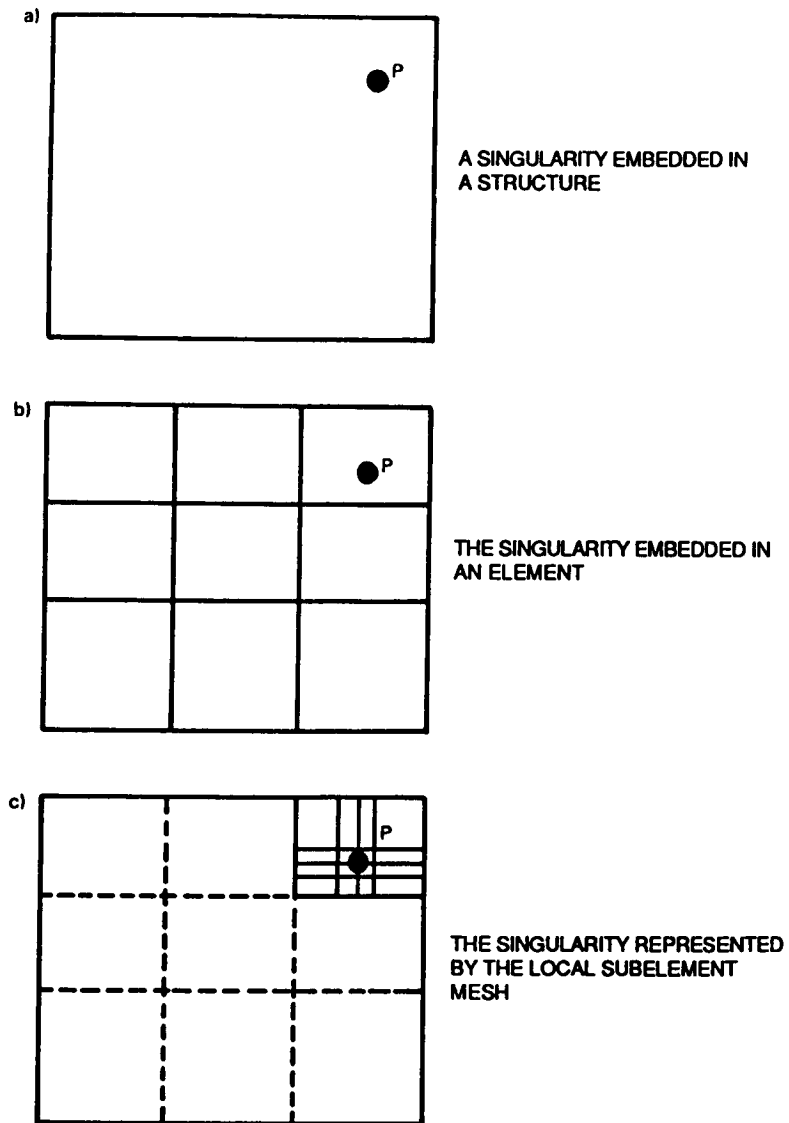


Figure 3.3-3 Local-Global Representation of an Embedded Singularity

Topologically, the global mesh is constructed such that the minimum element size is much larger than the scale of the singularities so that no singularity is identified by the global system. The local system is constructed in a single global element and is coupled with the global system through nodes common between the single global element and the local elements within it.

A major difference of the present approach from substructuring is that the local refinement takes place a posteriori and the information extracted from the locally subelemented element is brought back to the global mesh via the residual load correction. This implies that no special algebraic treatment is required even when material nonlinearity occurs in the subelement region.

The concept of interacting two geometrical models implies an iterative algorithm as follows:

- (a) Solve the global system of finite element equations for preconditioning purposes, equation (3.3-17).
- (b) Use the above results together with information available for the singularity to set up the local finite element equations which have, in principle, the same form as equations (3.3-17) through (3.3-19).
- (c) Form the internal residual load vector based upon the result of step (b) and modify the right-hand side vector of the global system.
- (d) If the residual load vector is small enough, then exit; otherwise repeat from step (a).

As a result, overall equilibrium is achieved with respect to the presence of the local system.

This solution strategy represents a mixed version of the adaptive process which has been investigated in recent years and which has yielded results that are encouraging for elastic stress analyses with singularities. The computational strategy we propose here is to define the local mesh and the refined interpolation altogether in the region near the singularity in a manner somewhat similar to that of combined h-p refinement.

As a result, we expect to obtain an accurate stress-strain solution in the global approximation subspace enriched by the local approximations.

The final solution is found in the global-local system with the global system being used only for preconditioning purposes. This means that factorization of the approximate global stiffness matrix obtained by the conventional displacement method may be sufficient to kick off the present solution procedure. Further details will be discussed in following sections.

Consider as another practical situation a single displacement element with an embedded hole. The isoparametric element in the physical plane shown in Figure 3.3-4(A) is mapped onto the reference plane as shown in Figure 3.3-4(B).

Some computational aspects need to be considered here for application of the present method to practical problems of turbine engine hot section components.

From a programming point of view, a parametric representation of an elliptic hole by its size, orientation and location in a displacement element is convenient because this allows the code to generate directly subelement mesh data whenever such data are needed. The data structure is simple as no permanent storage allocation is required for the subelement mesh. In Figure 3.3-4(B), an example of such a ready-made subelement mesh is presented for a circular hole located at the center of displacement element mesh.

On the other hand, it may be user-friendly and perhaps conceptually more general to define explicitly the subelement mesh as an additional data set. The data structure then needs to be reviewed so as to allocate additional memory for subelement mesh storage.

As experienced in the h-version of adaptive mesh refinement, it is anticipated that the subelement mesh approach will be used recursively in a fashion similar to that of the multi-level substructure technique. A well-organized data storage scheme needs to be developed, therefore, in order to realize a fully flexible implementation of the proposed method.

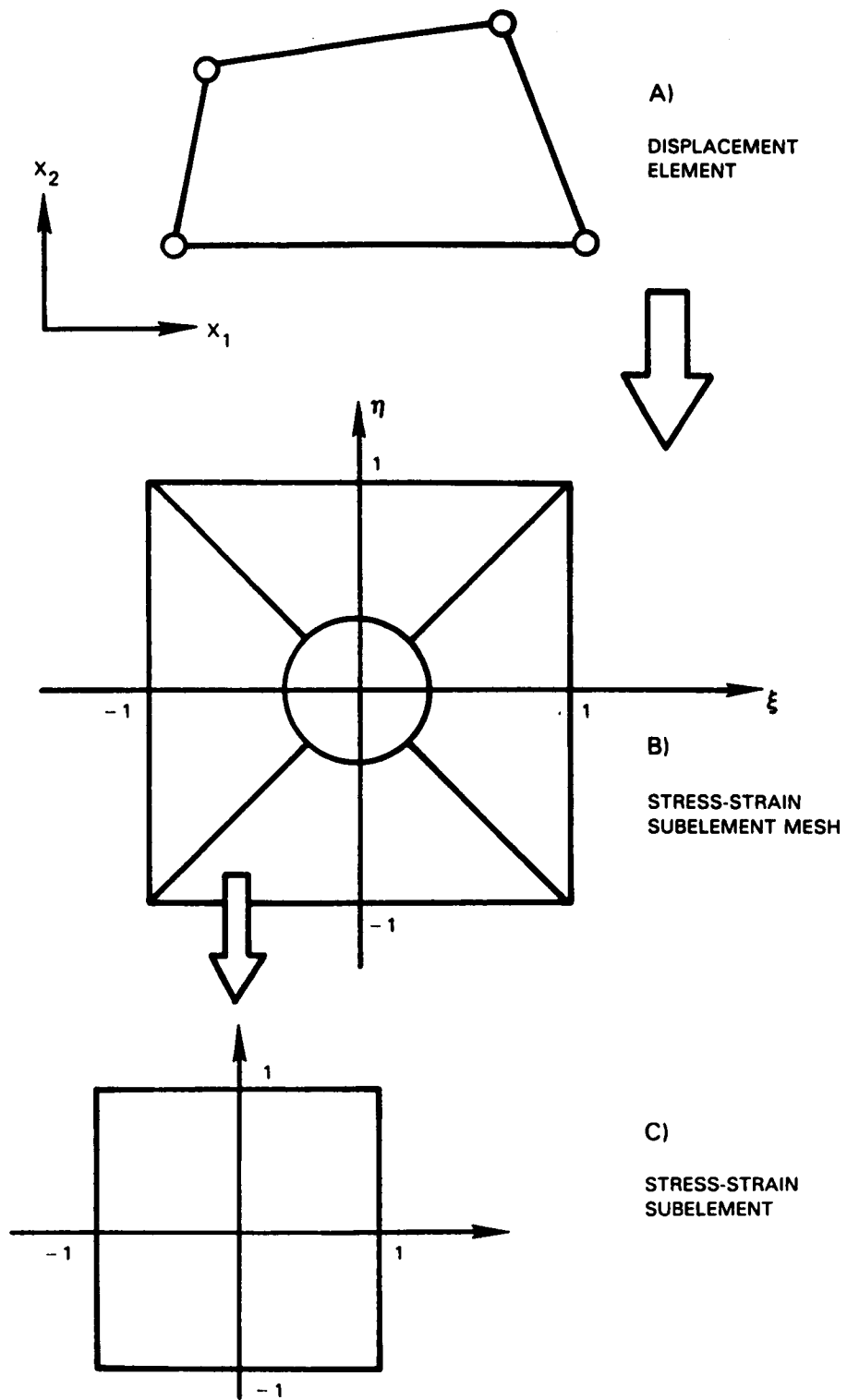


Figure 3.3-4 Multiple Isoparametric Mapping for an Element with an Embedded Hole

In the following discussions, we assume (for the purpose of simplicity) that the subelement mesh is defined in the isoparametric element coordinate system rather than in the physical space in which the global mesh is defined.

The stresses and strains are represented at the nodes of subelements defined in the first reference plane, Figure 3.3-4(B). We introduce variables to characterize the internal deformation of the stress and strain subelements so as to obtain these quantities uniquely in an accurate manner. As mentioned in the first section, some further mathematical investigation is required to come up with an optimal combination of subelement mesh definition, functions to represent the deformation of each subelement as well as the stress-strain interpolations.

A major difficulty encountered in multidimensional computation involves integrating the coupling matrix  $B$  over the subelement, Figure 3.3-4(C). Once the size of the hole and its location are identified, the values of displacement interpolation functions are obtainable at every nodal point of the subelement mesh. Denoting these quantities by  $N_K$ , we introduce the local displacement-type interpolation of  $N$  in these elements by:

$$N = N_K^S N_K \quad (3.3-75)$$

and the coupling matrix is integrated approximately by:

$$B = \left[ \int_S \frac{\partial N_K^S}{\partial(\xi, \eta)} N_L^S d\xi d\eta N_K \right], \quad (3.3-76)$$

where the superscript  $S$  denotes the functions defined at the subelement level. The calculation is carried out on each local subelement  $\Omega^S$  and summed over the global displacement element. This general integration procedure plays a central role in coupling the global and local meshes by representing the residual load vector at the global displacement node locations yet reflecting the information at the local element level. For consistent definition of the operator matrix  $B$ , the transformation of the shape function from global to local

needs to be carried out as defined by equation (3.3-75) on the isoparametric element space, Figure 3.3-4(B). This must also be properly coordinated with the fact that each subelement in Figure 3.3-4(B) is individually mapped into another isoparametric space, Figure 3.3-4(C).

It is obvious that the location of nodal points is needed in the element coordinate system. When the locations of subelement nodal points are specified in the physical plane, then the inverse of the nonlinear isoparametric mapping needs to be calculated in order to find these points in the element coordinate system.

We outline the solution strategy in a general format. First, as a preconditioner, we introduce the conventional stiffness equation with respect to the global displacement degrees of freedom  $u$  as follows:

$$\underset{\sim}{K} \underset{\sim}{u} = \underset{\sim}{F} . \quad (3.3-77)$$

This is derived directly from the virtual work principle in terms of displacement. A modified recursive form of the mixed finite element equations is written again in terms of the global unknown variables:

$$\begin{bmatrix} \underset{\sim}{K} & 0 & \underset{\sim}{B} \\ 0 & \underset{\sim}{C} & -\underset{\sim}{Q} \\ -\underset{\sim}{B}^T & -\underset{\sim}{Q}^T & 0 \end{bmatrix} \begin{Bmatrix} \underset{\sim}{u} \\ \underset{\sim}{\epsilon} \\ \underset{\sim}{\sigma} \end{Bmatrix} = \begin{Bmatrix} \underset{\sim}{F} + \underset{\sim}{K} \underset{\sim}{u} \\ 0 \\ 0 \end{Bmatrix} \quad (3.3-78)$$

Setting  $\underset{\sim}{u}^{(0)} = \underset{\sim}{0}$  and  $\underset{\sim}{\sigma}^{(0)} = \underset{\sim}{0}$  with the superscript being used for the iteration counter, we solve the system of displacement equations:

$$\underset{\sim}{u}^{(n+1)} = \underset{\sim}{u}^{(n)} + \underset{\sim}{K}^{-1} (\underset{\sim}{F} - \underset{\sim}{B} \underset{\sim}{\sigma}^{(n)}) . \quad (3.3-79)$$

Then the stresses and strains are updated in the subelement region by solving implicitly:

$$\begin{bmatrix} \tilde{C} & -\tilde{Q} \\ -\tilde{Q}^T & 0 \end{bmatrix} \begin{Bmatrix} \tilde{\epsilon}^{(n+1)} \\ \tilde{\sigma}^{(n+1)} \end{Bmatrix} = \begin{Bmatrix} 0 \\ \tilde{B}^T \tilde{u}_s^{(n)} \end{Bmatrix} \quad (3.3-80)$$

with  $\tilde{u}_s$  being the enriched displacement in the subelement region. To obtain this quantity, the factorization of a displacement type stiffness equation is required in this region.

It should be noted that the discussion presented here describes in general terms the solution strategy used. The approach actually implemented into the code involves hierarchical displacement approximations for realizing the interaction between the global and local meshes.

Equation (3.3-80) is improved by increasing the information contained on the right-hand side. The use of additional terms characterizing the deformation near the singularity needs to be considered. The simplest approach, for example, is to take the displacement as a dummy variable at stress-strain nodal points, with the displacement interpolated by conventional polynomial basis functions in a manner similar to that of the substructuring technique.

When such variables are introduced, the solution procedure becomes very close to what is called the multi-grid method in the finite difference context. The overall solution flow can then be given as follows:

- (a) Solve for the global displacement by equation (3.3-79).
- (b) Recover the strain at nodes in the global finite element mesh.
- (c) Evaluate the stress at nodes in the global finite element mesh.

- (d) Enter the inner loop and calculate the displacement quantity (used only as a dummy variable) in the subelement mesh.
- (e) Evaluate the stress and strain by equation (3.3-80).
- (f) Check the convergence in terms of residual in the subelement mesh. If not converged, repeat from step (d).
- (g) Evaluate the global residual including the stresses in the subelement. If convergent, start a new increment; otherwise, repeat from step (a).

Through the inner loop, the global finite element mesh interacts with the subelement and an accurate, high-resolution stress field is obtainable without increasing the size of the global stiffness equations.

It is emphasized that additional coding is needed to incorporate steps (d) to (f), which can be performed by adding an element routine to handle the embedded singularities and by allocating the core storage associated with the arrays used for the inner iteration. As the size of the algebraic equations used for representing the embedded singularity is limited, a performance test is needed to decide whether to employ either a nested loop for within-element solution or factorization of the same matrix without iteration.

### 3.3.5 Computer Program Development

#### 3.3.5.1 Solution Capabilities

Version 2.0 of the MHOST program, which is the development version for Task II efforts, currently supports many options and a limited number of linear and quadratic finite elements, all of which are operational for both the mixed iterative approach described in Section 2 and the conventional displacement method. The MHOST analysis capabilities are summarized in Tables 3.3-I and 3.3-II. Additional information is provided below through descriptions of the control parameter keywords.

Table 3.3-I

## MHOST Analysis Capability: Element Definition Options

Element Definition Options	Beam	Plane Stress	Plane Strain	Axi-symmetric Solid	Three-Dimensional Solid	Three-Dimensional Shell
Linear <sup>*1</sup> Elasticity	x	x	x	x	x	x
Simplified Plasticity		x	x	x	x	x
Elasto- <sup>*1</sup> Plasticity		x	x	x	x	x
Unified Creep-Plasticity		x	x	x	x	x
Thermal <sup>*2</sup> Strain		x	x	x	x	x
Creep <sup>*2</sup> Strain		x	x	x	x	x

## NOTES:

\*1 Applicable to isotropic and anisotropic (user subroutines) materials.

\*2 Not applicable to unified creep-plasticity in which these quantities are the integrated part of the model.

Table 3.3-II

## MHOST Analysis Capability: Analysis Module Options

Analysis Module Option	Beam	Plane Stress	Plane Strain	Axi-symmetric Solid	Three-Dimensional Solid	Three-Dimensional Shell
Quasi-static Analysis	x	x	x	x	x	x
Buckling Analysis	x	x	x	x	x	x
Modal Analysis	x	x	x	x	x	x
Transient Dynamics	x	x	x	x	x	x

## \*ANISOTROPY

Elastic material anisotropy may be included in an analysis by adding the user subroutine UHOOK. The anisotropic plastic response of a material is described by the user subroutine ANPLAS as documented in the MHOST User's Manual.

## \*BFGS

The inverse BFGS update procedure is invoked by flagging this optional parameter. The default iterative algorithm is the conventional Newton-Raphson scheme.

## \*BOUNDARY

Nodal displacement constraints are imposed using a penalty approach as discussed in Section 3.3.4.2.

## \*BUCKLE

The initial stress stiffness matrix is formed and an eigenvalue extraction is performed to obtain buckling modes. This option can be invoked at an arbitrary step of the incremental nonlinear solution process in order to detect the change in the buckling load due to inelastic response of the structure.

## \*CONSTITUTIVE

Three different constitutive formulations are included in the code for describing material behavior. They involve: (1) secant elasticity (simplified plasticity) in which the material tangent is generated for use with Newton-Raphson type iterative algorithms; (2) von Mises plasticity with the associated flow rule treated by using the radial return algorithm; and (3) the nonlinear viscoplastic model developed by Walker, in which an initial stress iteration using the elastic stiffness is utilized. A linear elasticity option can be flagged for experimental purposes, and the default is the conventional von Mises plasticity model. Anisotropic plasticity is invoked by updating the user subroutine ANPLAS. The dummy subroutine supplied with the MHOST code is always required to produce correct results for isotropic cases.

#### \*CREEP

Creep effects are taken into account by integrating the time history in an explicit manner. An optional self-adaptive time step size control algorithm is available.

#### \*DISPLACEMENTMETHOD

This option invokes the conventional displacement model in which the residual load is evaluated directly at the integration points. For linear elastic stress analysis, no iteration will take place when this option is flagged. In inelastic analyses, the material tangent is interpolated and multiplied by the integration point strain which is directly sampled at the quadrature point. This option cannot be used for the advanced constitutive model since the correct material tangent is not generated.

#### \*DISTRIBUTELOAD

Body force and surface traction loadings are referred to as distributed loads in the MHOST program. The body force option includes gravity acceleration definable in any direction and centrifugal loading with the centerline and angular velocity specified by the user.

#### \*DUPLICATENODE

The continuity of stresses at nodal points can be broken by defining two nodal points at the same geometrical location and connecting them by this option which enforces compatibility of displacements only. This option is used to define the connections between generic modeling regions.

#### \*DYNAMIC

The generalized Newmark time integration algorithm is entered by setting this flag. A simple adaptive time stepping algorithm is employed at the user's option.

## \*ELEMENTS

The elements included in this version of the code are described in Table 3.3-III. Core allocation is performed for the nodal and element quantities on the basis of maximum storage space requirements among the types of elements specified in this option.

## \*EMBED

The subelement iteration capability is flagged by this option which signals the code to allocate the working storage for the subelement data in a hierarchical manner. The actual subelement mesh definition and the nodal and element data storage allocation take place when the individual subelements are defined.

## \*FORCES

Concentrated nodal forces are defined and stored in an incremental manner. Core allocation takes place only when this option is invoked.

## \*FRONTALSOLUTION

The frontal solution option for quasi-static analysis is implemented in this version of the code. Out-of-core storage devices are utilized and, hence, the capacity of the program is increased significantly. A direct access, rather than a sequential access, file is used for the solution buffer to avoid overhead due to the backspace operation in the back substitution phase.

## \*GMRS

Generic modeling regions are defined as collections of elements that model geometrically parametrized parts of hot section components. Multiple generic modeling regions in a given mesh are connected using the duplicated node option. Different parameters are specified for each generic modeling region, and

the input data can be prepared separately. Internally, the complex of the generic modeling regions is treated as a single mesh for the purposes of constructing and solving the finite element equations. A table is prepared to report results separately for each generic modeling region.

#### \*LOUBIGNAC

Parameters for numerical quadrature used in the mixed iterative processes are defined in a very precise way. Full integration, selective integration, or selective integration with filtering can be chosen for construction of the stiffness matrix. For residual vector integration, full and reduced integration can be selected. The strain integration can be performed either by using uniformly reduced integration, trapezoidal integration with the reduced shear strain approximation or the previous quadrature with the filtering option.

#### \*MODAL

The free vibration modes of linear elastic structures are extracted when this option is invoked. The subspace iteration technique is utilized and a power shift option is included.

#### \*NODES

All the variables are defined and reported at nodal points. In the incremental processes, deformation and stress histories are integrated and stored only at the nodal points. Note that this architecture economizes storage substantially compared with fully integrated finite element displacement methods.

#### \*OPTIMIZE

A band width optimization procedure, based on the Cuthill-McGee algorithm, is applicable to in-core solution processes. No optimization procedure is required for the frontal solver.

## \*PERIODICLOADING

For transient calculations, nodal displacements and concentrated forces can be input as sinusoidal functions using this option.

## \*POST

The postprocessing data, which contain all the information supplied to and generated by the code, are written to the file connected to FORTRAN unit number 19. This file is formatted and can easily be manipulated by commercially available postprocessing packages with minor modifications. The header record of the file is designed to be compatible with the MARC post file which is processed by many finite element graphics packages.

## \*PRINTSETS

The report generation is carried out on a nodal point basis with element integration point options provided by interpolation using the shape function.

## \*REPORT

The frequency of the line printer report generation is now controlled by this option. The default is to print at every increment.

## \*SCHEME

Parameters that control the characteristics of the time integration operator are defined by the user. The default is the average acceleration algorithm commonly used in nonlinear dynamic finite element analysis.

## \*STRESS

Boundary conditions for stress can be specified by the user as an option, although no mathematical justification is yet available for this type of constraint. Any stress component can be prescribed at any nodal point. Simple

numerical tests have shown that inconsistent imposition of stress boundary conditions can lead to rapid divergence in the iterative process, so this option should be used with caution.

#### \*TANGENT

This option invokes the modified Newton iteration procedure. The tangent matrix is updated until a user-specified iteration count greater than or equal to 1 is met. No updating occurs in subsequent iterations. The default iteration count is equal to 1, and the procedure generated by this value is known as the  $K_{T1}$  method of modified Newton iteration. This option has no effect when the BFGS process is employed.

#### \*TEMPERATURE

Nodal temperatures are read and used to generate thermal strains. These quantities are used also for the evaluation of creep strain and the integration of coupled creep-plasticity models such as Walker's model.

#### \*THERMAL

Temperature dependent material properties are evaluated when this option is invoked and the appropriate user subroutine is provided to the system prior to execution. This operation is not necessary for the conventional creep model since temperature dependence can easily be incorporated into the user subroutine CRPLAW.

#### \*TRANSFORMATIONS

Coordinate transformations at nodal points are specified by this option in which the angle of rotation is input by the user so that the code can generate necessary transformation matrices. The postprocessing file does not support coordinate transformations at this time.

## \*TYING

Multiple degree-of-freedom constraint equations are specified by the user through this option. Note that constraint equations are generated only for the displacement degrees-of-freedom. This option is more flexible than the duplicate node option since constraints may be applied to individual degrees-of-freedom.

The following parameters are used to signal to the MHOST program the presence of specific user subroutines:

*UBOUN	*UFORCE	*UTEMP
*UCOEF	*UHOOK	*UTHERM
*UDERIV	*UPRESS	

As summarized above, the analysis capability included in the MHOST code covers most of the needs for inelastic analysis of turbine engine hot section components. The free format data input routines and report generation packages have been improved in the Task II program development effort to create a more comfortable environment for users. Presently, the code consists of around 30,000 lines of FORTRAN statements including extensive self-explanatory comment lines in each subroutine. The preliminary system document was generated in an automatic manner from these comment lines and the cross reference capability available on the Prime FORTRAN compiler and linker.

Table 3.3-III summarizes the elements currently available in the MHOST code, Version 2.0, and the parameters used internally to define element characteristics. Further details are available in the MHOST User's Manual.

Lagrangian rather than Serendipity quadratic functions are being employed in the MHOST code at present. This choice was based, in part, on the fact that Serendipity elements are known to behave in a less accurate manner than Lagrangian elements for nonlinear fracture mechanics applications based on the quarter point technique. In addition, the lumped mass approximation for nodal stress/strain recovery has not been implemented in Serendipity elements and,

hence, the accuracy and stability of these elements are not yet known in the context of mixed iterative computations. Lagrangian elements have, in contrast, already produced encouraging results in the mixed iterative environment.

Table 3.3-III

MHOST Code, Version 2.0  
Elements and Parameters

	Beam	P. Stress	P. Strain	Axsym.	Brick	Shell
ITYPE	9	3 / 101	11/ 102	10/ 103	7	75
NELCRD	3	2	2	2	3	3
NELNFR	3	2	2	2	3	6
NELNOD	2	4 / 9	4 / 9	4 / 9	8	4
NELSTR	1	3	4	4	6	8
NELCHR	3	5	5	5	5	5
NELINT	2	4	4	4	8	4
NELLV	3	3	3	3	3	4
NELLAY	0	1	1	1	1	5
NDI	1	2	3	3	3	2
NSHEAR	0	1	1	1	3	1
JLAW	1	2	3	4	5	6

- NELCRD      Number of coordinate data per node.
- NELNFR      Number of degrees-of-freedom per node.
- NELNOD      Number of nodes per element.
- NELSTR      Number of stress and strain components per node.
- NELCHR      Number of material property data for the element.
- NELINT      Number of 'full' integration points per element.
- NELLV      Number of distributed load types per element.
- NELLAY      Number of layers of integration through the thickness of the shell element.
- NDI          Number of direct stress components.
- NSHEAR      Number of shear stress components.
- JLAW        Type of the constitutive equation.

Four-point Gaussian quadrature is employed in the stiffness calculations for the Lagrangian elements in accordance with common practice. The lumped mass matrix with unit density constructed for strain recovery is also based on reduced four-point quadrature instead of the nodal quadrature used in the linear quadrilaterals. Similarly, other integrations in the strain recovery process employ reduced integration in order to avoid stress/strain oscillation.

The ongoing investigation of quadratic element technology will focus on reproduction of nonlinear material behavior and sensitivity to isoparametric distortion.

The algorithm used in the MHOST code to construct the residual load vector, which drives the iterative solution, has employed mixed strain/stress interpolation for all the generalized strain/stress components. However, the mixed continuous strain recovery for certain terms can possibly violate the necessary condition for stability and cause convergence to an inferior numerical solution after a number of iterations. This numerical instability is particularly significant when the method is applied to incompressible problems and the dilatation terms are smoothed during the iterative displacement update. Due to the similarity in the mathematical structure of constraints, the transverse shear terms in the bending of plates and shells could cause the same difficulty if they are smoothed in the iterative process. Hence, a modified algorithm which utilizes the smoothed stress field for all the terms except the transverse shear so as to avoid possible numerical instability has been implemented into the MHOST code.

#### 3.3.5.2 Data Storage and Control Structure

The input data and information associated with the global finite element formulation and solution are stored in blank common using a conventional dynamic core allocation scheme. No array is prepared for quantities defined at element integration points. The storage required for the subelement iteration is allocated in the same work area in an indirect way. We prepare the element array for pointers and the actual work area is allocated when the storage is required. At this time, the pointer array is filled. The conceptual representation of the indirect core storage scheme enables us to set up a multi-level subelement refinement.

In the recovery phase for residual vectors associated with the iterative solution, a flag is set to indicate whether the global displacement mesh is subelemented or not. This flag is built into the code internally as part of the element definition data array. The same flag can also be attached to the definition data for subelements. From the global displacement mesh definition

upwards, the generic modeling regions (GMRs) can be handled internally in the same fashion. That is, a tree structure of element mesh topology is constructed.

The use of out-of-core storage may be needed to swap the information related to different mesh levels, and the storage scheme for the element level data manipulation is retained as it is. This means that the subelement mesh data are loaded to the array where the global mesh is stored when the subelement level analysis module is entered. If further refinement is activated, the software stack is pushed down again. Such a recursive storage scheme enables us to use the existing element manipulation scheme developed for the global solution without major modifications.

The reporting scheme is such that the global solution is reported as it is carried out in the present code, and then the same data stack is used for generating reports separately at the subelement level.

The nodal coordinates of the subelement mesh need to be stored in terms of the local coordinates defined in the global system. For catalogued mesh subdivisions such as the one shown on Figure 3.3-4, these values are easily defined in the required system of coordinates.

When the mesh is prepared by the user in physical space, the nonlinear equation which represents its isoparametric counterpart is solved by an iterative manner. It is feasible to utilize the bilinear mapping function for the geometrical definition of subelements, assuming that in practice, the subelement size is small enough compared with the geometrical features of the entire structure.

The actual subelement solution is carried out in the element residual calculation routine. When the subelement flag is set in the element loop, the subelement solution driver routine is entered and the mixed iterative solution is performed in the subelement domain. A set of procedures, which are somewhat different from the global solution subroutines, has been developed to manipulate matrices for the subelement domain.

### 3.3.6 Validation/Verification Analyses

#### 3.3.6.1 Analysis of Plate and Shell Structures

The complexity of plate and shell problems is mainly due to the higher order derivatives in the variational functional, or equivalently the necessity to introduce additional rotational degrees-of-freedom. The results of a series of analyses which demonstrate the characteristics of the MHOST shell element are presented in this section.

##### Clamped Plate with Central Load

The displacement convergence characteristics of the current version of the plate and shell element are illustrated on Figure 3.3-5. The solution for a clamped plate subjected to a concentrated load is plotted together with some well-known plate solutions obtained using the finite element method. In terms of the deflection at the center of the plate, mixed iteration produces results consistent with a conventional mixed formulation. Note that the Reissner-Mindlin plate solution (the result from displacement preconditioning) provides a lower bound where the mixed and mixed iterative solutions provide an upper bound of the solution. The MHOST code could be tuned to reproduce the lower bound solution, if desired, by selectively undoing the continuous stress approximation, particularly for the bending moments.

##### Plate Supported at Corners

The performance of the hourglass control algorithm is demonstrated using an example of a square plate supported at its corners and subjected to a concentrated load at its center. This is the same model problem used by Belytschko and Tsay (Reference 12). The problem statement is illustrated on Figure 3.3-6, and the results with and without the hourglass control are plotted on Figures 3.3-7 and 3.3-8. The participation factor for the fully integrated transverse shear stiffness matrix was determined using this example and further validation analyses were performed to ensure that the hourglass control modification does not significantly change numerical solutions.

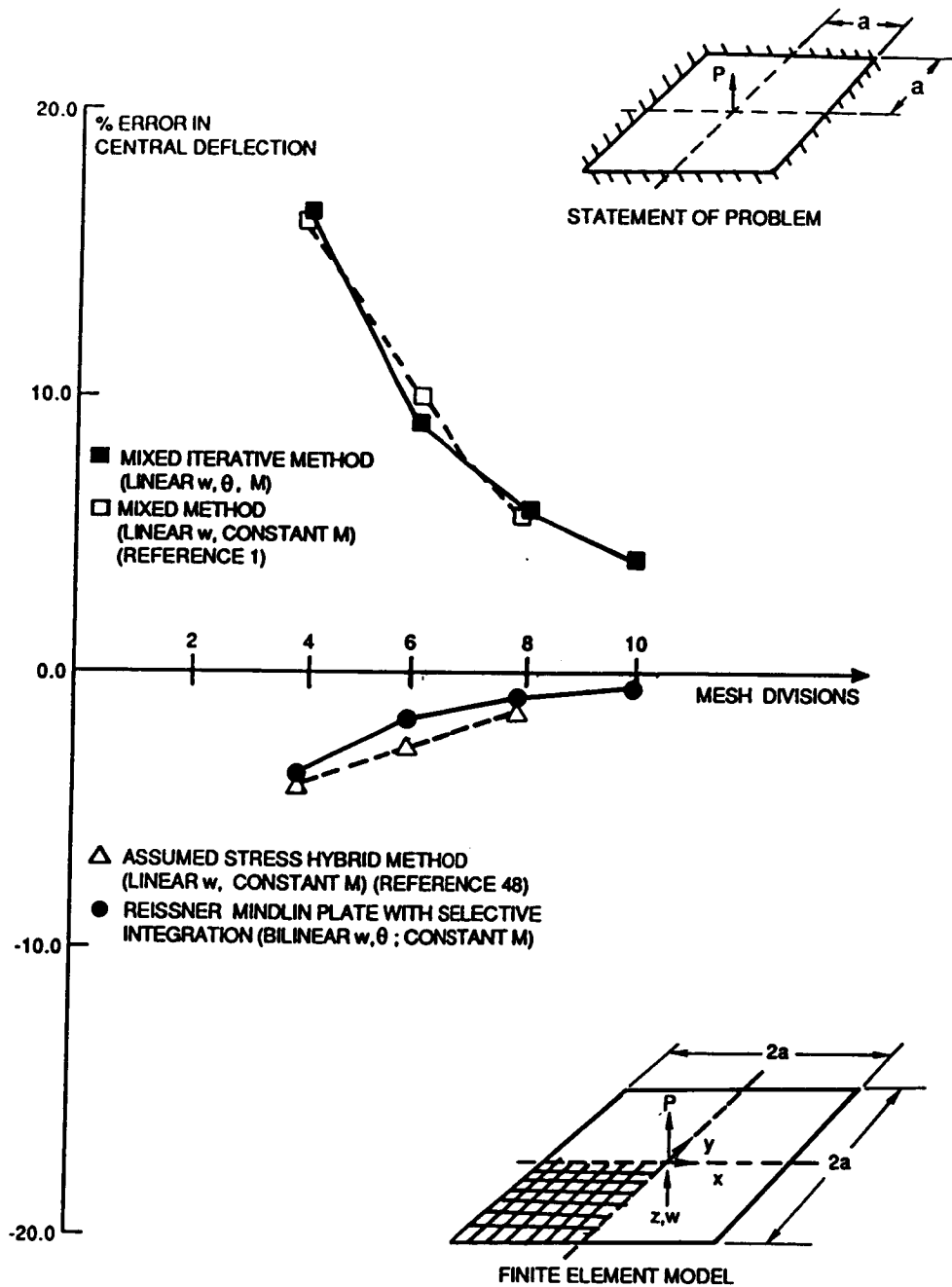


Figure 3.3-5 Clamped Square Plate

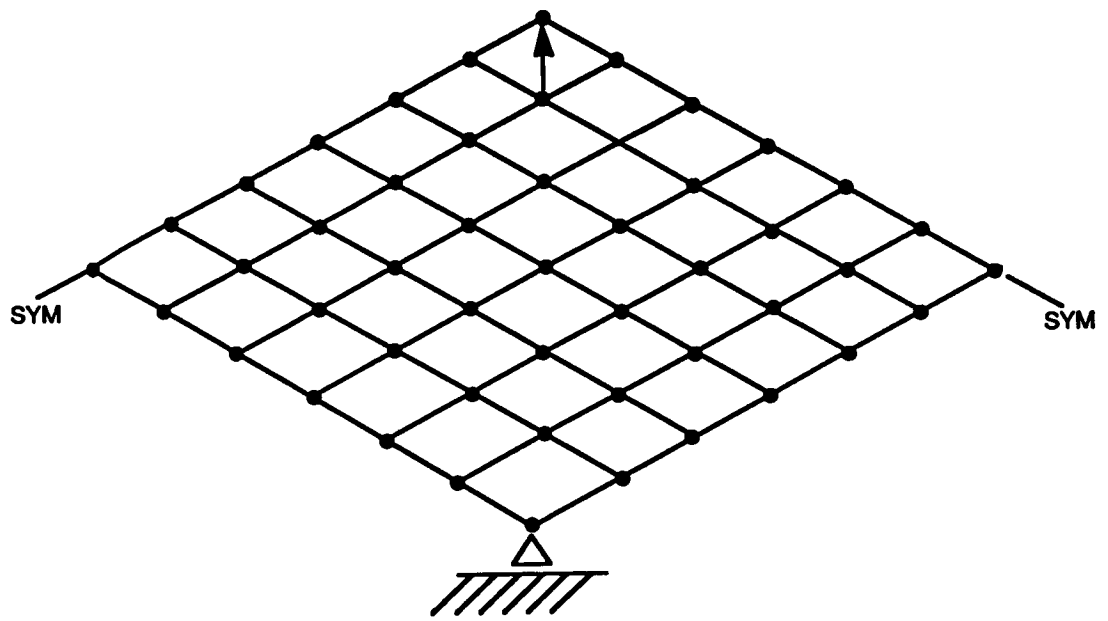


Figure 3.3-6 Corner Supported Plate with Central Concentrated Load

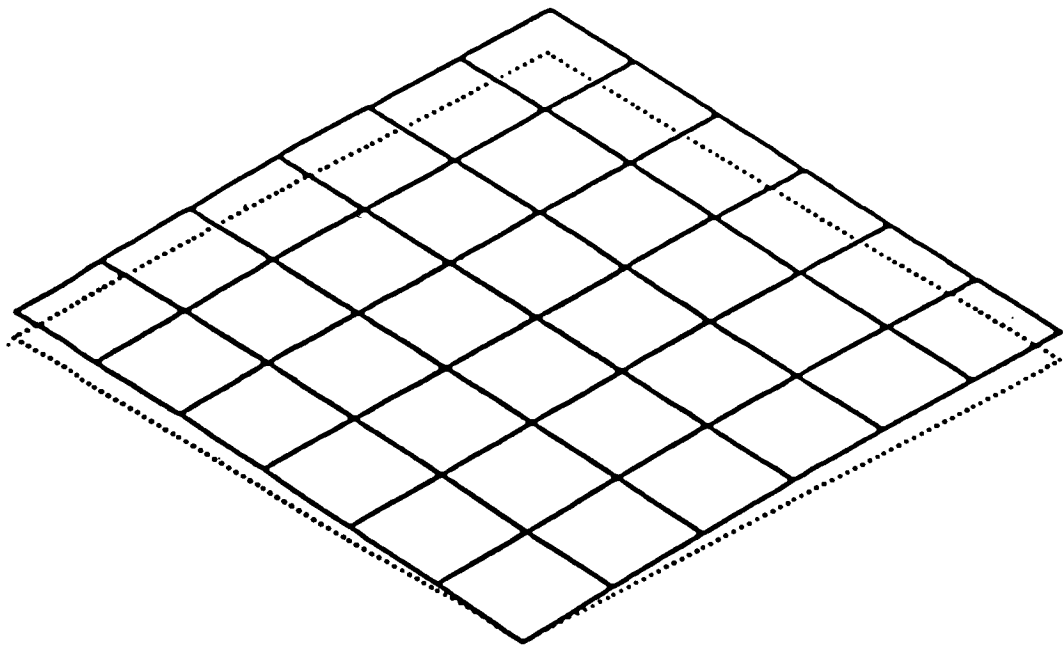


Figure 3.3-7 Lateral Displacement with Hourglass Control

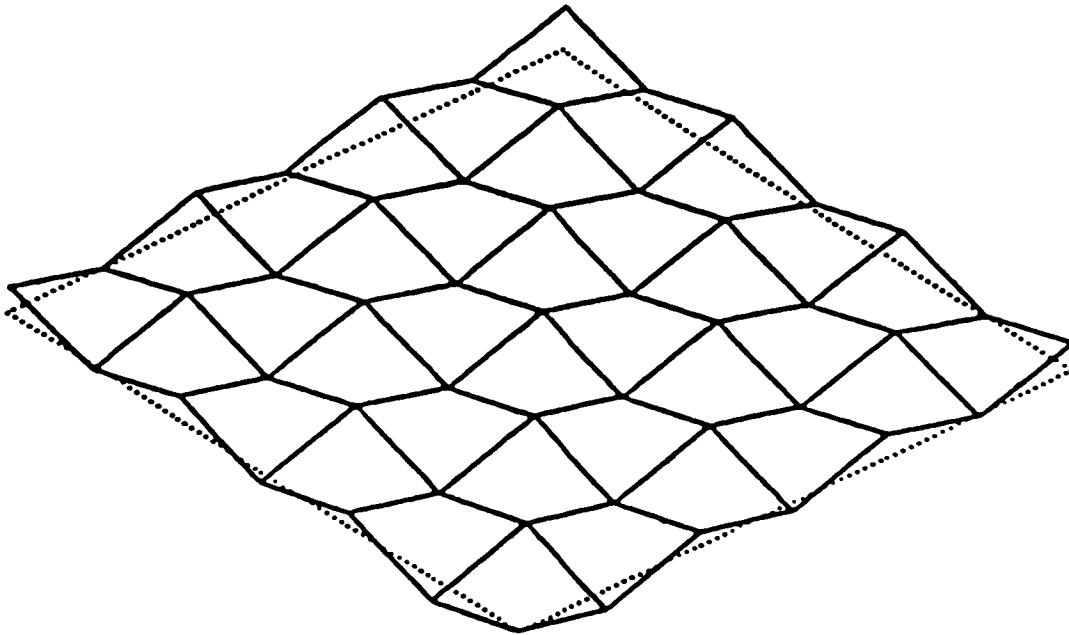
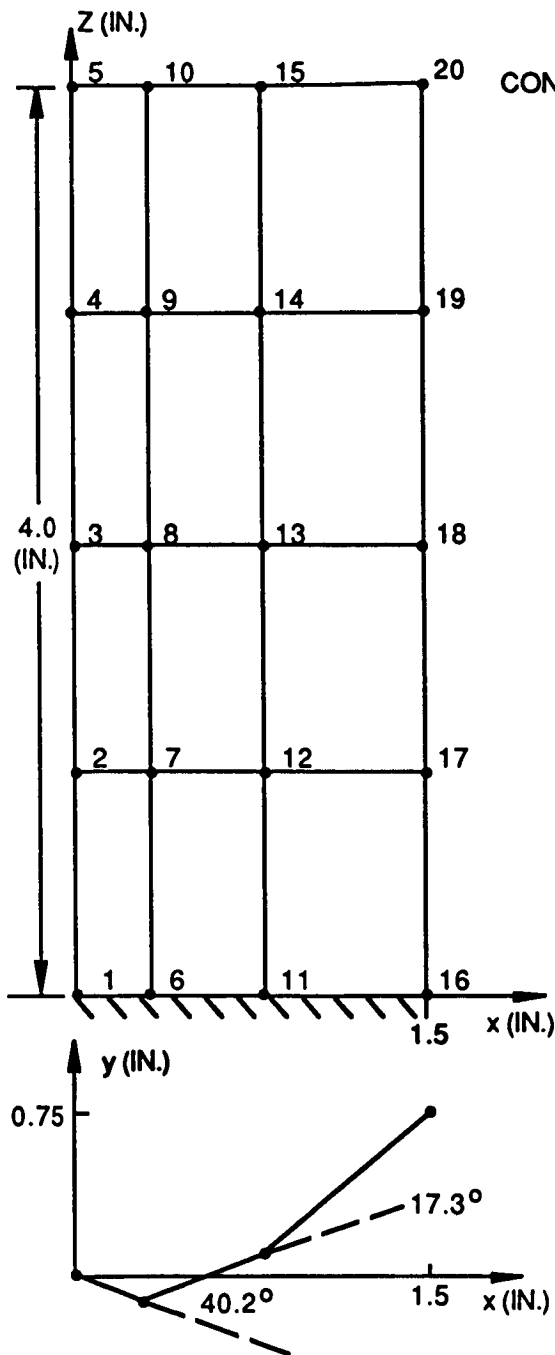


Figure 3.3-8 Lateral Displacement without Hourglass Control

#### Simplified Turbine Vane Airfoil

A highly simplified model of a turbine vane airfoil has been studied as part of the shell element validation effort. The finite element model and applied loads are shown on Figure 3.3-9. A primary motivation for analyzing this structure was to determine the effects of kink angles between adjacent elements on the behavior of the MHOST mixed iterative solution process. As shown on Figure 3.3-9, kink angles as large as  $40^\circ$  were present in the model.

Constant thickness analyses were performed using MARC element 75 (bilinear Reisner-Mindlin shell, Reference 11) and the NASTRAN QUAD4 element as well as the MHOST shell element. Typical displacement results at nodes 10 and 20 are shown in Table 3.3-IV. MHOST results with zero iterations compared very favorably with the MARC and NASTRAN values. The MHOST displacements for the iterated analysis were larger than the other tabulated results, but this behavior is not considered unreasonable for such a coarse mesh. However, the relatively slow rate of convergence of the iterative process (14 iterations) is a source of concern.



$E = 30 \times 10^6$  PSI.  $\nu = 0.3$ .

CONSTANT THICKNESS MODEL:  $t = 0.1$  IN.

VARIABLE THICKNESS MODEL

NODES	THICKNESS (IN.)
1 - 5	0.10
6 - 10	0.25
11 - 15	0.15
16 - 20	0.10

LOADS: + x DIRECTION

NODE	FORCE (LB.)
5	7.5
10	7.5
15	7.5
20	7.5

Figure 3.3-9 Simplified Vane Model

Table 3.3-IV

## Displacements for Constant Thickness Vane Model

<u>Deck/Element</u>	<u>Number of Iterations</u>	<u>x-Displacement (in.)</u>	
		<u>Node 10</u>	<u>Node 20</u>
MARC/75	-	$0.469 \times 10^{-2}$	$0.745 \times 10^{-2}$
NASTRAN/QUAD4	-	$0.477 \times 10^{-2}$	$0.764 \times 10^{-2}$
MHOST/75	0	$0.468 \times 10^{-2}$	$0.762 \times 10^{-2}$
MHOST/75	14	$0.496 \times 10^{-2}$	$0.822 \times 10^{-2}$

The investigation was continued with analyses of the variable thickness model. In this case, results using MARC element type 4 (Hermitian curved shell element) were obtained in place of QUAD4 results. Displacement solutions obtained for nodes 10 and 20 are shown in Table 3.3-V. The tabulated variable thickness results show the same trends as those exhibited by the constant thickness displacements. In an effort to improve the convergence results, continuity of stresses/strains across the largest kink angle was destroyed by introducing duplicate nodes coincident with nodes 6-10. This action had the effect of reducing residuals by about an order of magnitude as is shown on Figure 3.3-10. The displacements in the x direction at nodes 10 and 20,  $0.320 \times 10^{-2}$  inch and  $0.400 \times 10^{-2}$  inch respectively, compared favorably with corresponding results for the continuous stress/strain case (Table 3.3-V).

In summary, the cantilevered vane results showed that, while substantial kink angles between adjacent shell elements do not cause the MHOST iterative procedure to produce erroneous results, such angles can slow convergence to the point that complete stress/strain continuity constraints may have to be relaxed on a selective basis in order to achieve acceptable convergence rates.

Table 3.3-V

Displacements for Variable Thickness Vane Model

Deck/Element	Number of Iterations	x-Displacement (inch)	
		Node 10	Node 20
MARC/4	-	$0.267 \times 10^{-2}$	$0.356 \times 10^{-2}$
MARC/75	-	$0.274 \times 10^{-2}$	$0.357 \times 10^{-2}$
MHOST/75	0	$0.266 \times 10^{-2}$	$0.341 \times 10^{-2}$
MHOST/75	20	$0.331 \times 10^{-2}$	$0.415 \times 10^{-2}$

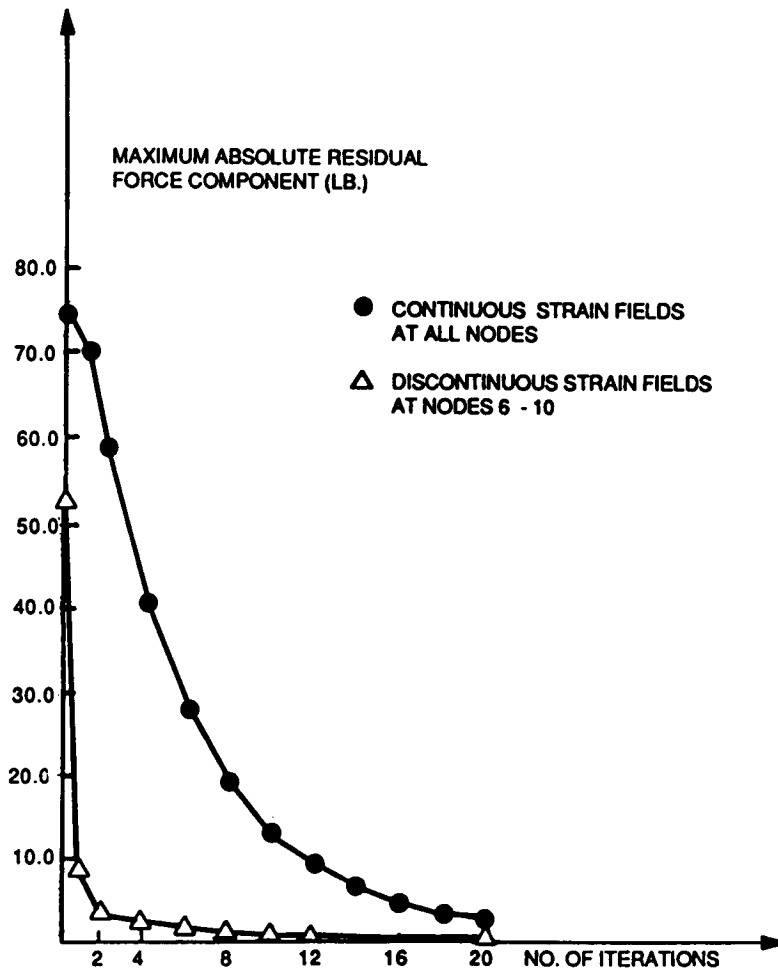


Figure 3.3-10 Convergence of Residual Forces

## Transient Response of a Simply Supported Bar

The pinned beam shown on Figure 3.3-11 represents a simple validation case for the MHOST time integration algorithm (constant average acceleration option). The beam was modeled using three MHOST shell elements, and was subjected to the impulsive pressure load shown on the figure. The lateral displacement time history is compared to a MARC modal solution (Timoshenko beam element model) on Figure 3.3-12. As the plotted results show, the MHOST solution is in excellent agreement with the MARC results over the complete time range (0.0 to 0.18 seconds).

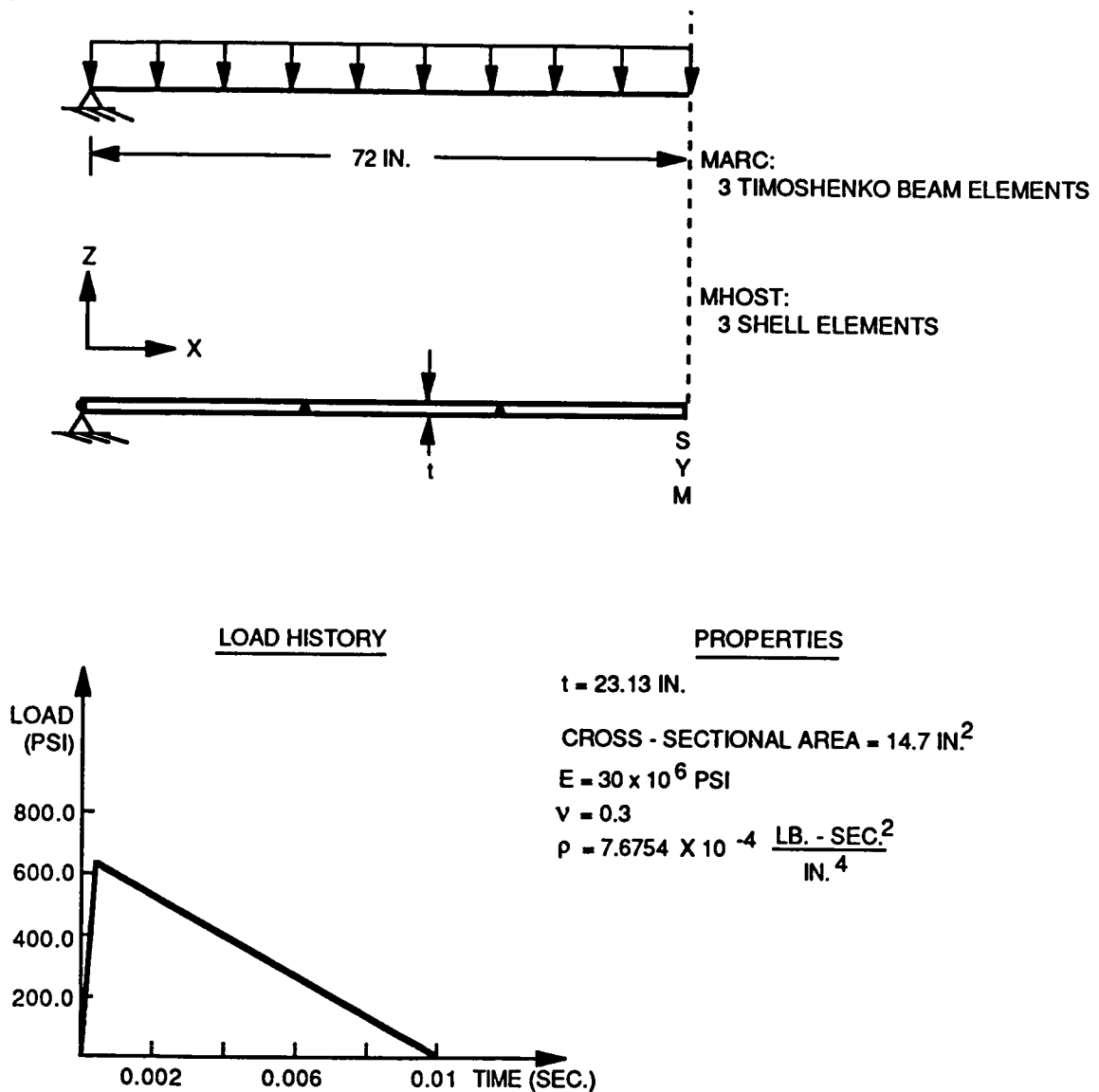


Figure 3.3-11 Model and Dynamic Loads for Pinned Beam

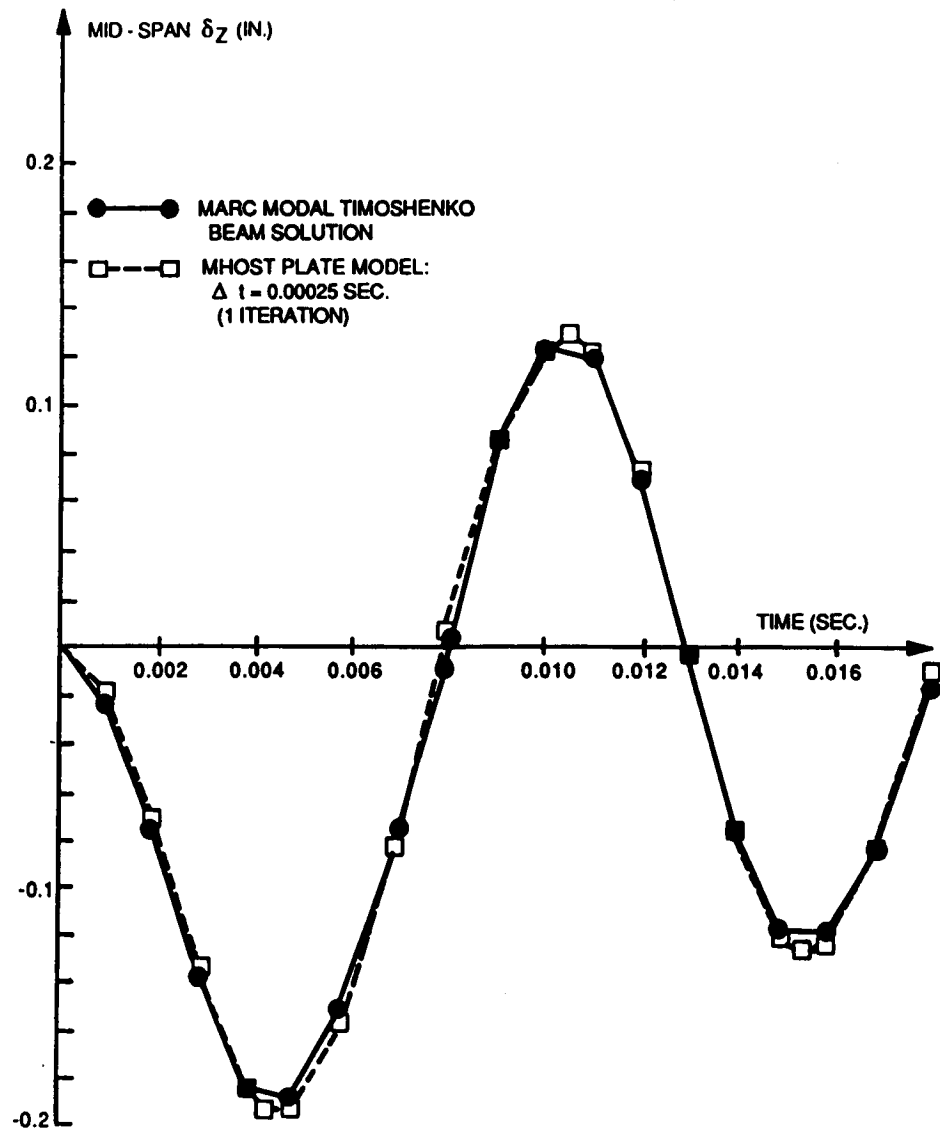


Figure 3.3-12 Pinned Beam: Mid-Span Deflection

## Free Vibrations of a Cylindrical Fan Blade

The MHOST free vibrations capability was verified by analyzing the well-known Lindberg and Olson cylindrical fan blade (Reference 49). The MHOST shell element model of the fan blade as well as a NASTRAN model that employs an 8 node element (Reference 50) are defined on Figure 3.3-13. The MHOST frequencies for the first ten modes are compared to NASTRAN and test values in Table 3.3-VI. Overall, the MHOST frequencies are in good agreement with test values, and represent approximately the same level of approximation as the tabulated NASTRAN results. Macroscopic comparisons between MHOST and experimental mode shapes are shown on Figure 3.3-14. The MHOST program captures the essential characteristics of all the modes shown on the figure.

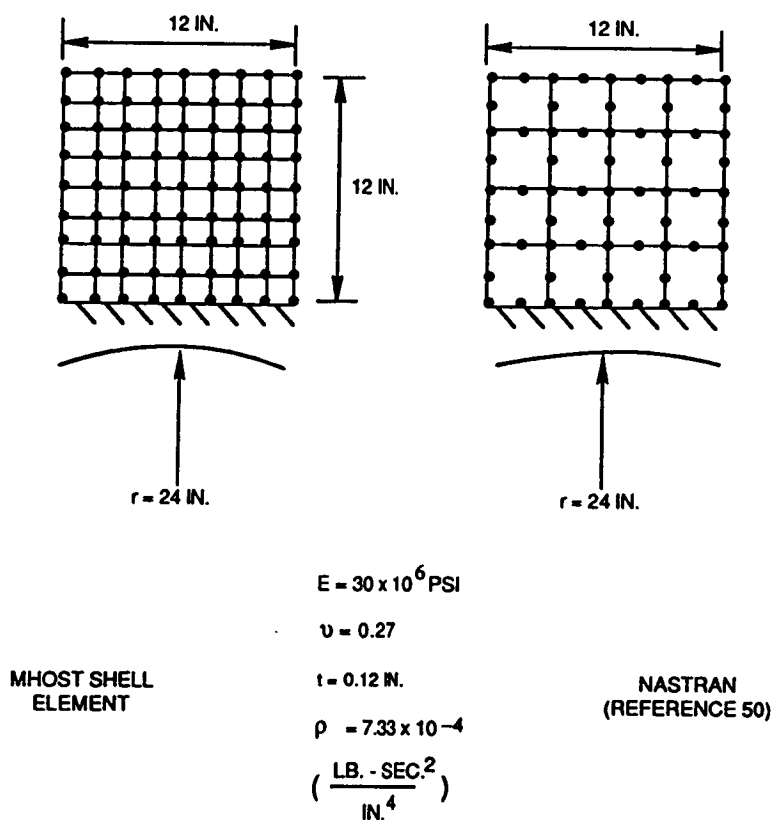


Figure 3.3-13 Models of Lindberg and Olson Fan Blade

Table 3.3-VI

Frequencies for Lindberg and Olson Fan Blade

Mode	Type*	Test	Frequencies (Hz)	
			NASTRAN	MHOST
1	A	85.6	86.7	87.0
2	S	134.5	139.6	138.9
3	S	259.0	250.3	253.5
4	A	351.0	349.6	355.8
5	S	395.0	407.9	395.9
6	A	531.0	552.5	571.7
7	A	743.0	777.2	788.2
8	S	751.0	759.7	775.0
9	S	790.0	826.2	824.8
10	A	809.0	920.9	874.3

\*S = symmetric  
A = anti-symmetric

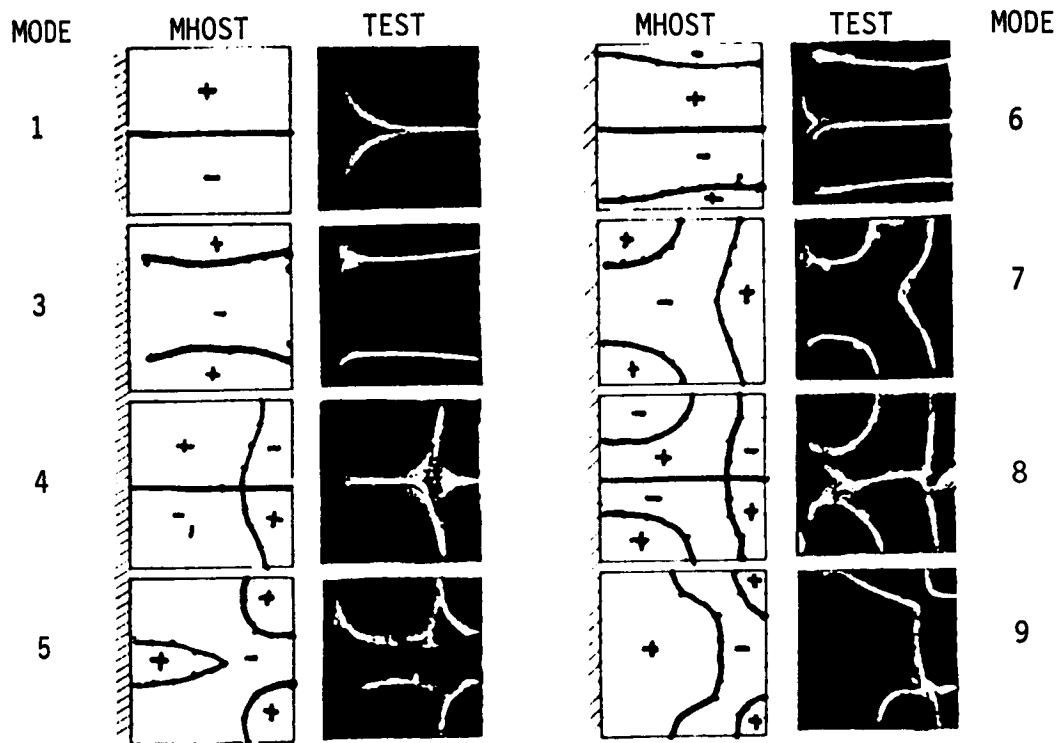


Figure 3.3-14 Comparisons Between MHOST and Experimental Mode Shapes

### 3.3.6.2 Analyses with Subelement Iterations

#### Cantilever Beam

The cantilever beam shown on Figure 3.3-15 was analyzed using a 2 x 10 global mesh in conjunction with uniform 2 x 2 subelement meshes. The subelement solution extracted exact bending stress/strain and displacement values at all nodes including the interior subelement mesh points.

A global 4 x 20 model of the beam was also analyzed to provide reference timing information. The computational efforts required for the standard and subelement approaches are summarized in Table 3.3-VII. It should be noted that the subelement procedure offers a computational advantage over the global approach in large-scale applications even though the total computational efforts listed in Table 3.3-VII do not reflect this fact. Since matrix solution costs increase by powers of the number of degrees-of-freedom, the reduction in this cost obtained using the subelement approach in large-scale applications will more than compensate for the cost increase associated with subelement calculations which varies linearly with problem size. The differences in matrix solution costs associated with the subelement and global procedures are apparent even in the cantilever example as is shown in Table 3.3-VII.

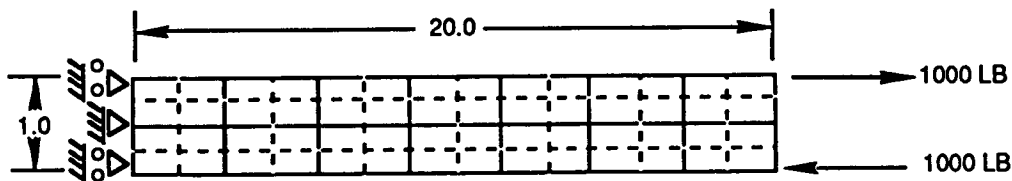


FIGURE NOT TO SCALE

$$E = 10^6 \text{ PSI}$$

$$\nu = 0.3$$

$$t = 1.0 \text{ INCH}$$

----- SUBELEMENT MESH

CANTILEVER BEAM PROBLEM (PLANE STRESS)

Figure 3.3-15 Cantilever Beam Validation Problem

Table 3.3-VII

Central Processing Unit (CPU) Time for the  
Beam Validation Problem

- Run A 2x10 mesh with 2x2 uniform subelement division throughout 66 main degrees-of-freedom and 360 subelement degrees-of-freedom
- Run B 4x20 mesh of the standard finite elements 210 degrees-of-freedom

<u>Operation</u>	<u>CPU Time (seconds in PRIME 9950)</u>	
	<u>Run A</u>	<u>Run B</u>
Matrix Assembly	0.803	2.267
Matrix Solution	0.091	2.290
Residual Calculation	<u>10.803*</u>	<u>3.906</u>
TOTAL	11.607	8.463

\*Including the subelement solution which averages 0.5 sec/global element.

Plane Stress Problem with a Reentrant Corner

The plane stress problem with a reentrant corner shown on Figure 3.3-16 was analyzed as a validation case for problems with discontinuities. Related work at Swansea has indicated that stress fields obtained from the mixed iterative procedure are oscillatory when stress singularities are present. These numerical difficulties are related to the stability condition of Babuska-Brezzi, and the possible unstable characteristics of equal order interpolation for displacement and stress have been pointed out by Oden (Reference 33). The stress distributions obtained by MHOST after global iteration with continuous stress fields are shown on Figures 3.3-17 through 3.3-19. Except for a small amplitude stress oscillation, no significant indication of numerical instability is observed.

The nature of the discontinuity at the reentrant corner is such that the continuous stress constraint is excessive. When this constraint is removed, a more accurate representation of singular behavior at the corner is obtained as shown on Figure 3.3-20. A further refinement shown on Figure 3.3-21 is obtained by using a 2 x 2 subelement mesh representation in the three elements at the singular point.

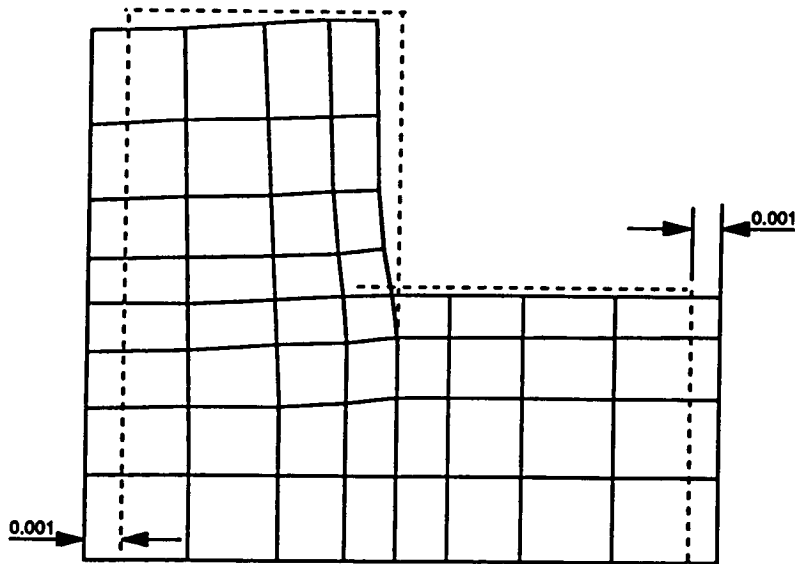
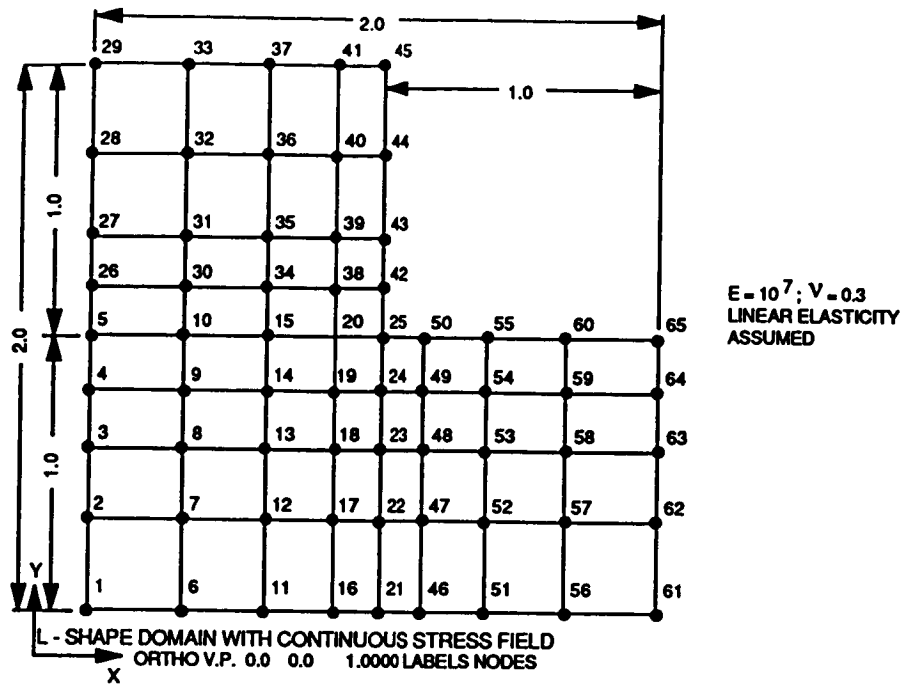


Figure 3.3-16 Problem Statement for Plane Stress Deformation of a Domain with a Singularity to Prescribed Displacement

ORIGINAL PAGE IS  
OF POOR QUALITY

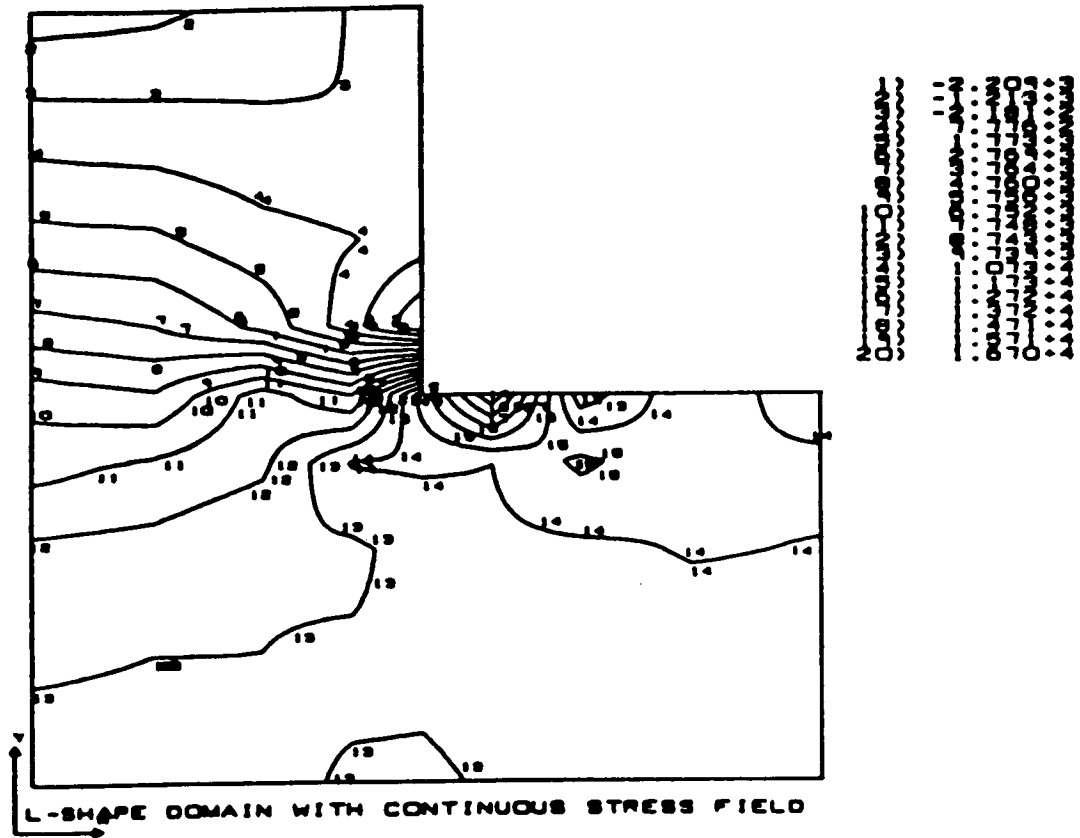


Figure 3.3-17 Stress Distribution ( $\sigma_x$ ) for L-Shape Domain with Continuous Stress Field

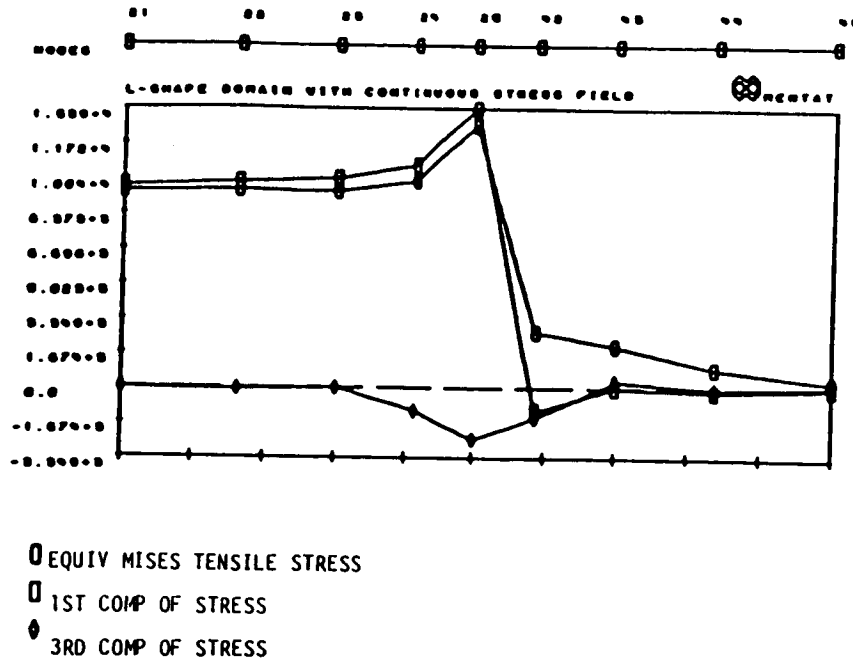


Figure 3.3-18 Distribution of  $\sigma_x$ ,  $\tau_{xy}$ , and Equivalent Stress Along Line Connecting Nodes 21 and 45

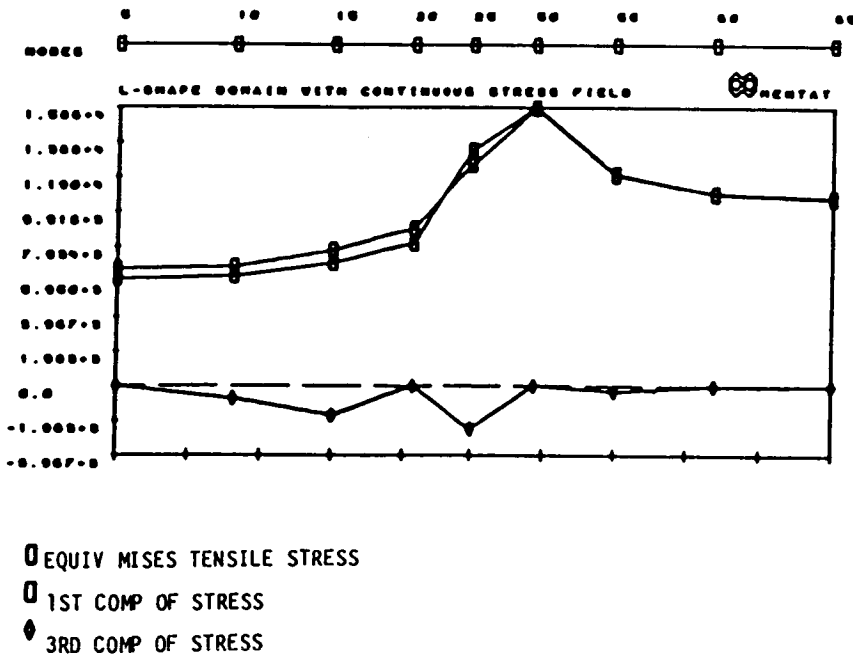


Figure 3.3-19 Distribution of  $\sigma_x$ ,  $\tau_{xy}$ , and Equivalent Stress Along Line Connecting Nodes 5 and 65

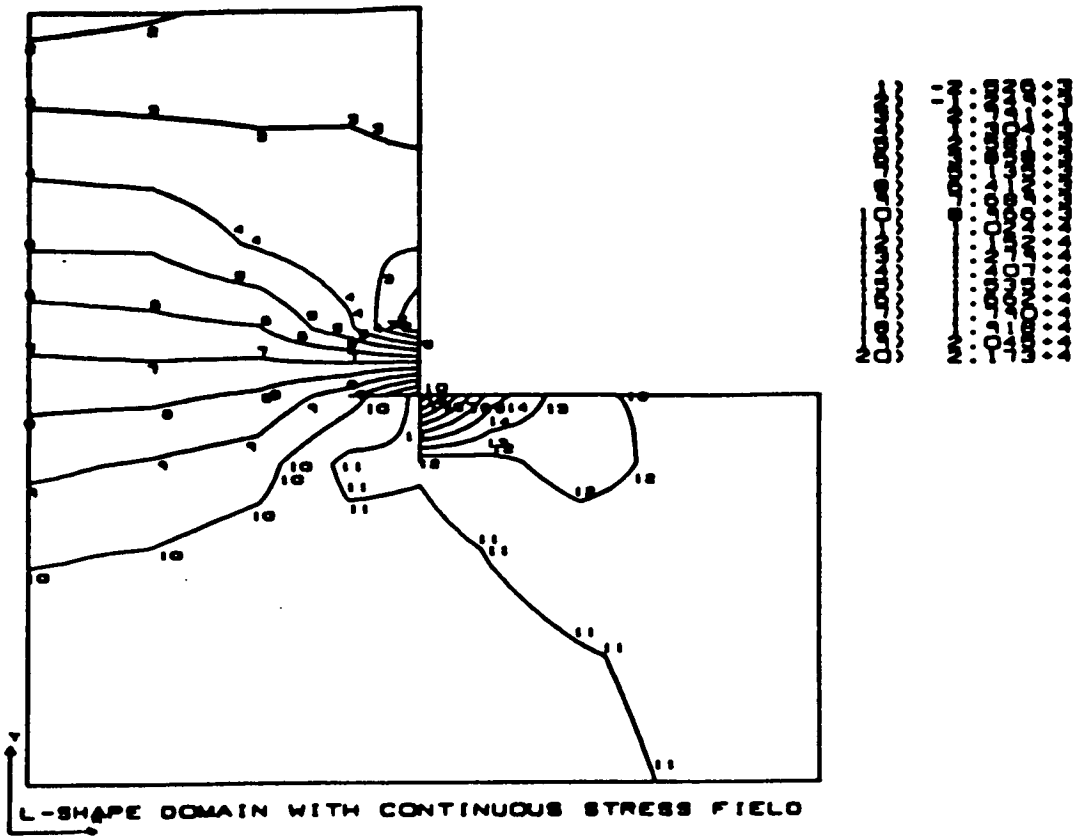


Figure 3.3-20 Stress Distribution ( $\sigma_x$ ) for L-Shape Domain with Discontinuous Stress Field

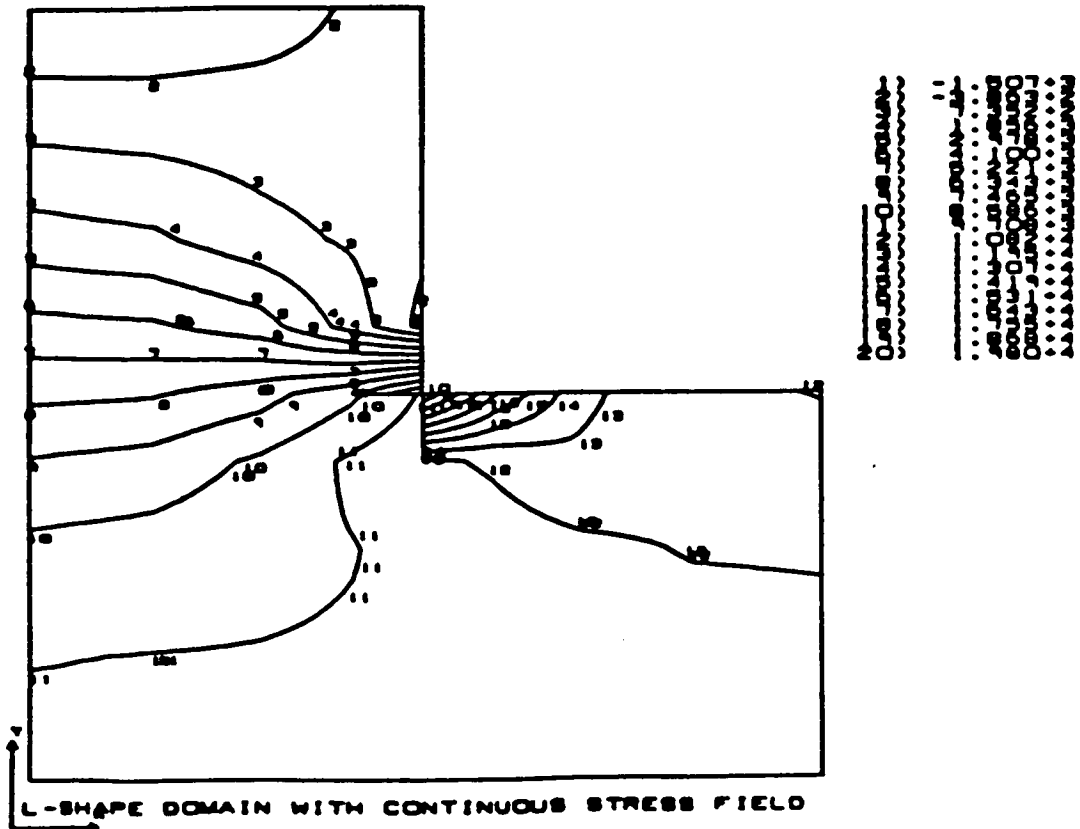


Figure 3.3-21 Stress Distribution ( $\sigma_x$ ) for L-Shape Domain with Discontinuous Stress Field and Subelement Mesh

## Inelastic Analysis of a Plate with a Hole

An elastic-plastic analysis of a plate with a circular hole was performed using the model shown on Figure 3.3-22. Elements 7, 8, 17, and 18 were divided into  $2 \times 2$  uniform subelement meshes. The material data used in the analysis are shown in Table 3.3-VIII. In this problem, an average of 4 to 5 iterations was required in each subelement to reach convergence with a displacement tolerance of 0.1. The deformed shape after one increment is plotted on Figure 3.3-23. As shown in Table 3.3-IX, the equivalent plastic strain detected at the subelement level in element 8 was an order of magnitude larger than the value observed in the global solution. This result indicates the potential capability of the subelement approach in nonlinear fracture mechanics applications.

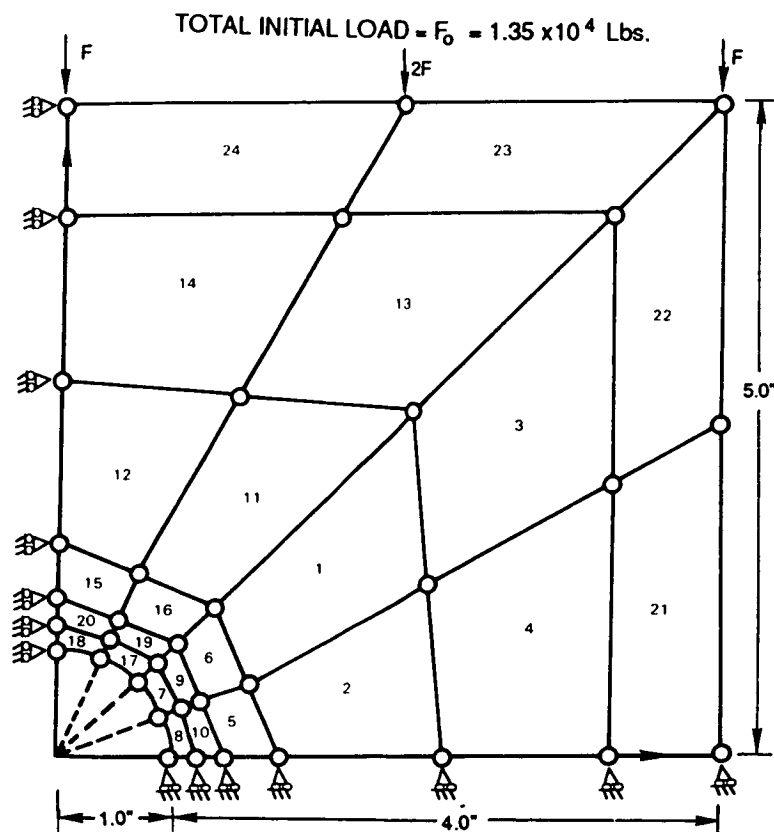


Figure 3.3-22 Finite Element Model of a Plate with a Circular Hole

Table 3.3-VIII

Parameters for the Validation Model  
of a Hole in Finite Plate

Thickness	1.0 inch
Young's Modulus	$3.0 \times 10^7$ psi
Poisson's Ratio	0.3
Yield Function	Plastic
Equivalent Stress (psi)	Equivalent Strain
$3.0 \times 10^4$	0.0
$3.5 \times 10^4$	$0.5 \times 10^{-2}$
$4.0 \times 10^4$	$1.5 \times 10^{-2}$
$5.0 \times 10^4$	$1.0 \times 10^{-1}$
$6.0 \times 10^4$	1.0

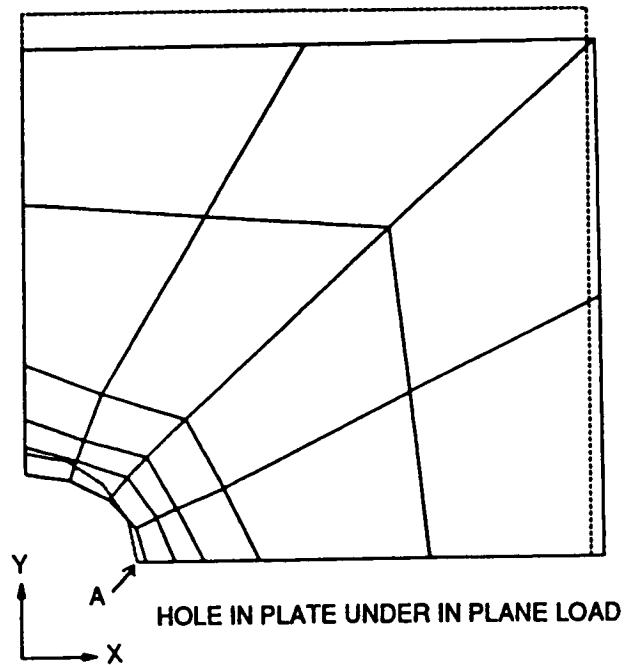


Figure 3.3-23 Deformation After One Increment

Table 3.3-IX

Solution at Point A by the Global and  
Subelement Iterations After Increment One  
Total Load  $F = 1.1 F_0$

	Global Node	Local Node
x Displacement (inches)	$6.5360 \times 10^{-4}$	$6.5360 \times 10^{-4}$
Von Mises Stress (psi)	$3.0003 \times 10^4$	$3.0185 \times 10^4$
$\sigma_x$ (psi)	$-1.9666 \times 10^3$	$-2.7765 \times 10^3$
$\sigma_y$ (psi)	$-3.0114 \times 10^4$	$-3.0941 \times 10^4$
$\tau_{xy}$ (psi)	$4.0285 \times 10^3$	$3.2650 \times 10^3$
Equivalent Plastic Strain	$3.5822 \times 10^{-6}$	$1.9407 \times 10^{-4}$

### 3.3.7 Three-Dimensional Solid Element Analyses

#### Burner Blister Specimen

A series of elastic-plastic analyses has been completed for a burner blister specimen configuration. The blister specimen was modeled as a  $45^\circ$  in-plane wedge with a radius of 1.5 inches, Figures 3.3-24 and 3.3-25. The thickness for the out-of-plane direction was 0.05 inch and three planes of nodes (each plane containing 199 nodes) were used through the thickness. The three planes were designated as bottom plane, mid-plane, and top plane respectively. Roller in-plane boundary conditions were applied along the horizontal and  $45^\circ$  wedge boundaries. Out-of-plane boundary conditions prevented rigid body motion. Eight-noded three-dimensional brick elements were selected for both the MHOST and MARC analyses, with two elements used through the out-of-plane thickness direction. Elastic and plastic material properties corresponded to realistic burner liner materials. The external loading involved a radially varying temperature distribution, which ranged from  $1800^\circ\text{F}$  at the vertex hot spot to  $1100^\circ\text{F}$  at the outer radius, Figure 3.3-26. The distribution was based upon experimental burner temperature measurements, was applied proportionally for incremental loading, and was linear through the thickness direction.

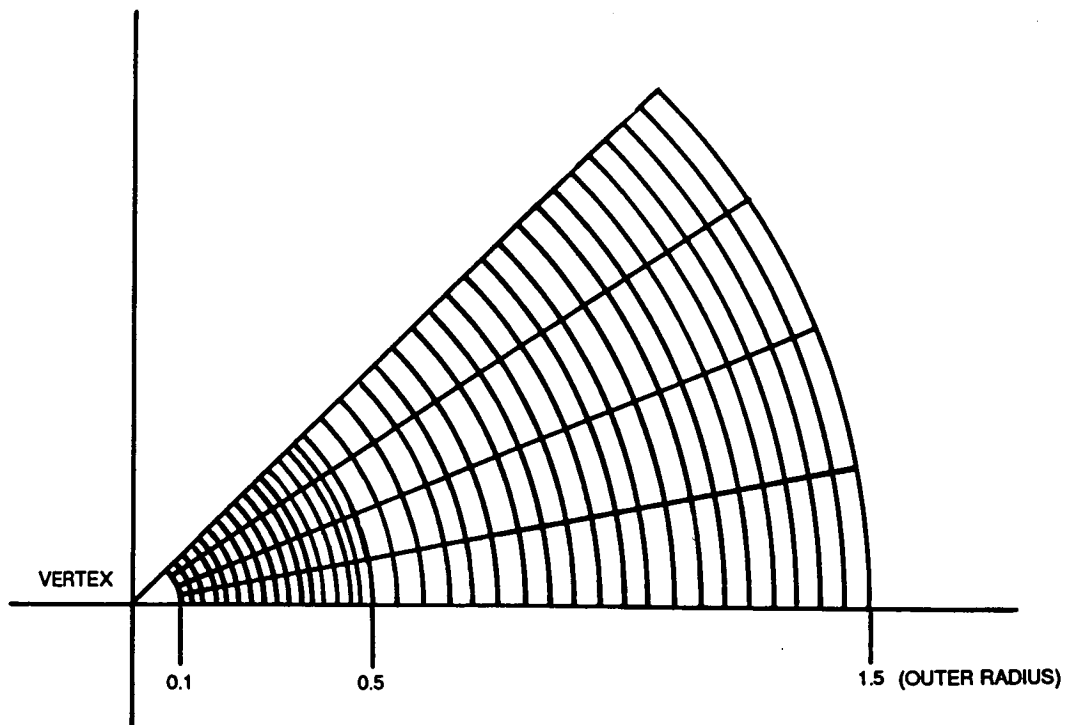


Figure 3.3-24 Burner Blister Specimen Model In-Plane General Breakup (Three-Dimensional)

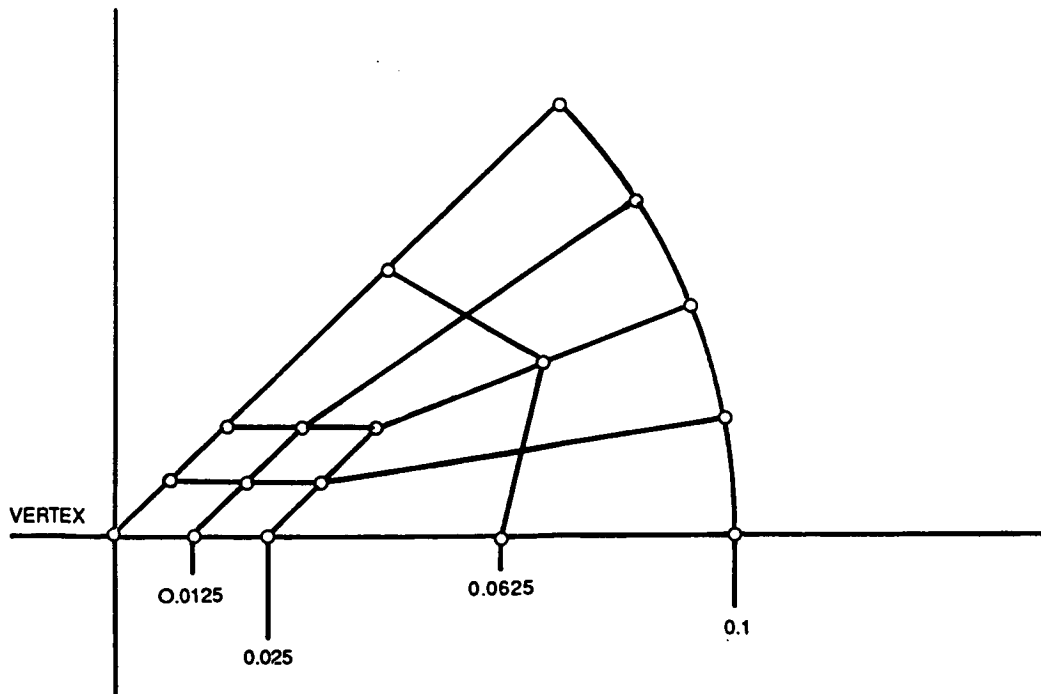


Figure 3.3-25 Burner Blister Specimen Model In-Plane Local Vertex-Neighborhood Breakup (Three-Dimensional)

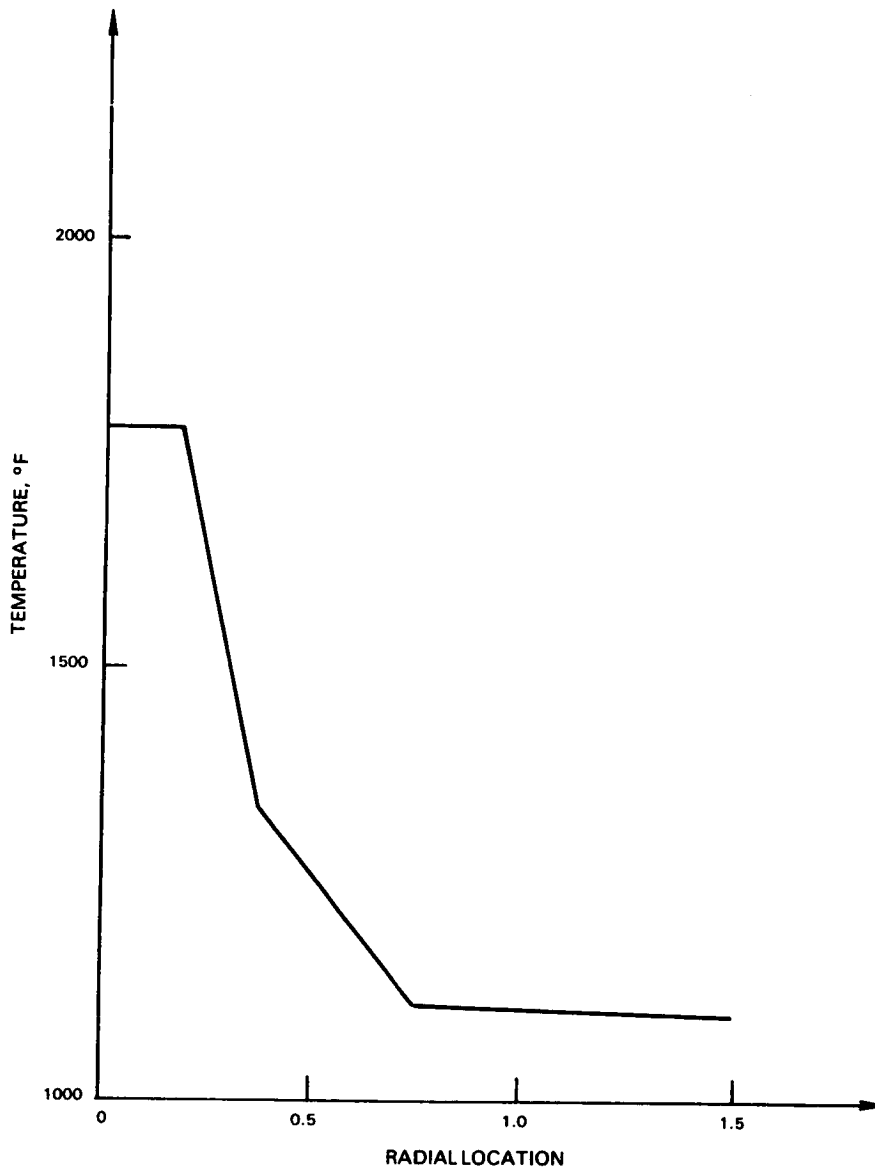


Figure 3.3-26 Hot Spot Temperature Distribution (Mid-Plane) for Burner Blister Specimen Model

In addition to a three-dimensional modeling of the burner blister specimen, a finer-meshed axisymmetric blister specimen model, Figure 3.3-27, was also developed and run on MARC. The axisymmetric model contained four four-noded elements through the thickness direction, as well as a mesh breakup near the vertex that was somewhat finer than the 3-D model mesh breakup near the vertex (compare Figures 3.3-27 and 3.3-25). The results associated with the MARC axisymmetric model calculations were taken to be base case numbers, to be used to judge the accuracy of the MHOST and MARC three-dimensional model calculations.

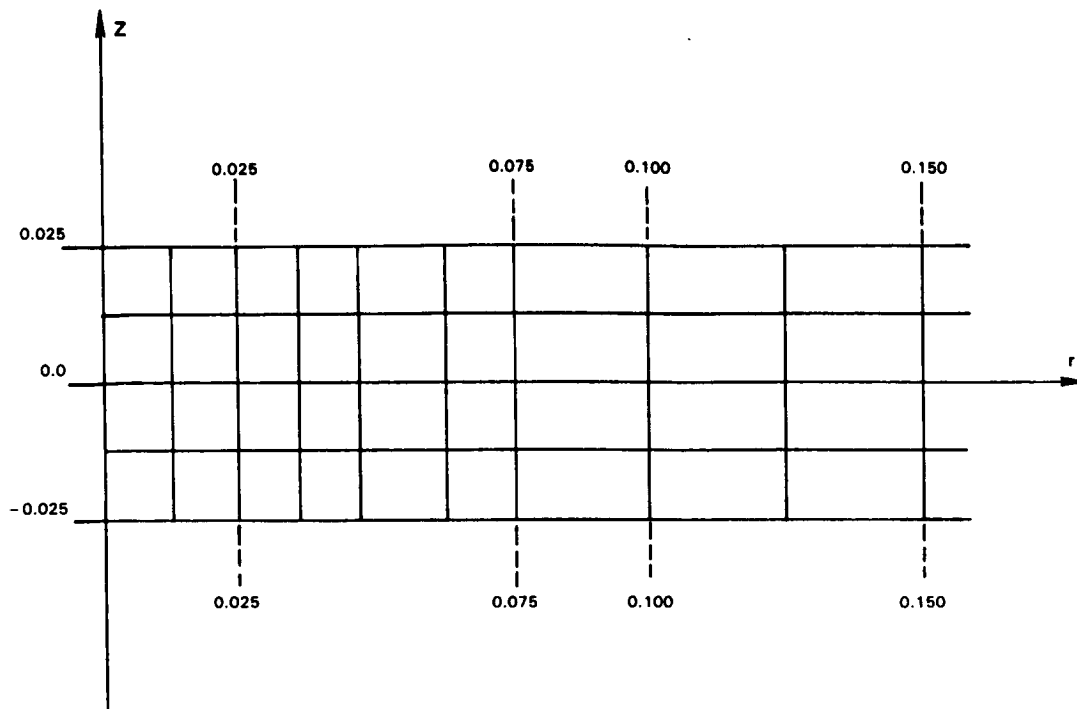


Figure 3.3-27 Axisymmetric Burner Blister Model for MARC-Breakup Near Vertex

Agreement of results between the MHOST and MARC three-dimensional model calculations was very good for most quantities. Typical of this good agreement are the results shown on Figure 3.3-28, where the Mises plastic strain at the mid-plane vertex node is plotted from both sets of results. As can be seen from this figure, the comparison is excellent even at 100 percent load for which significant plastic strain occurs at the vertex node. Even better agreement was obtained for the in-plane radial displacements which sometimes showed three or four figure exact matchup between MHOST and MARC values. It should also be noted that whenever good agreement occurred between MHOST and MARC three-dimensional calculations, the corresponding quantity found from the MARC axisymmetric calculation also agreed very well with both 3-D results.

On the other hand, poor agreement between the MARC and MHOST three-dimensional calculations was found for the out-of-plane displacement values, in particular for the blister displacement at the vertex nodes as indicated in Table 3.3-X.

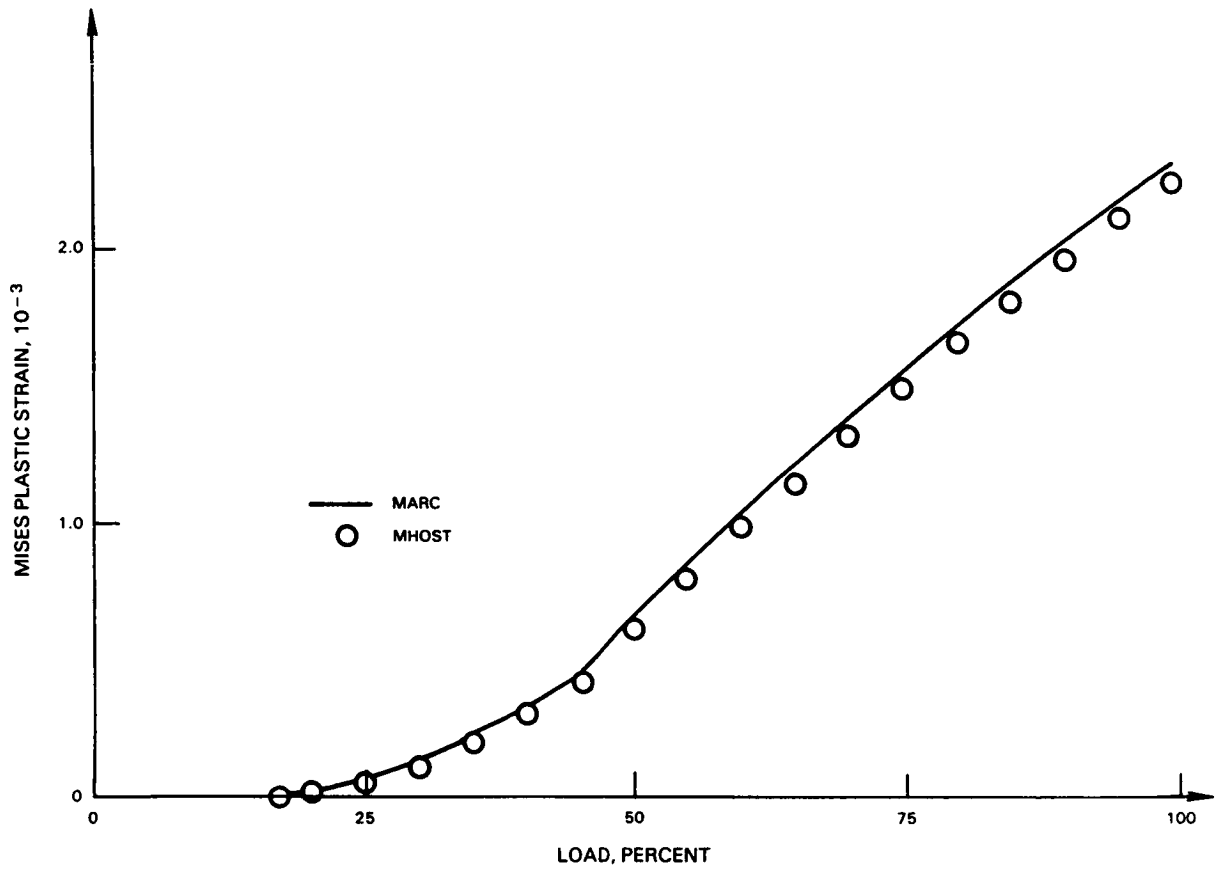


Figure 3.3-28 Mises Plastic Strain at Mid-Plane Vertex Node

Table 3.3-X

Out-of-Plane Displacement at Mid-Plane Vertex Node for 100 Percent Loading

MARC AXISYMMETRIC:	$5.0982 \times 10^{-3}$
MARC 3-D:	$1.2473 \times 10^{-3}$
MHOST 3-D:	$4.7697 \times 10^{-3}$

In general, the MHOST 3-D out-of-plane displacement values were about three or four times greater than those given by the MARC 3-D calculations, but were in quite good agreement with the MARC axisymmetric calculations, as indicated in Table 3.3-X. In fact, results from the MARC axisymmetric case showed good to excellent agreement with all corresponding MHOST 3-D results for all quantities.

It was concluded, therefore, that the MHOST code gave good to excellent results for all quantities in the three-dimensional burner blister specimen model with two three-dimensional elements through the thickness. In contrast, two three-dimensional elements through the thickness was not a fine enough breakup for MARC to generate accurate out-of-plane displacement values. It is felt that a possible cause for this poor accuracy is that the element coarseness through the thickness resulted in too high an out-of-plane stiffness for the MARC calculational procedure to be able to handle properly. It appears, therefore, that the MHOST code can handle coarser meshes better than the MARC code. The primary reasons for this advantage can be found from among the following factors: integrated use of reduced integration element technology, nodal evaluation of constitutive relationships, and equilibrium (Loubignac) iteration.

With regard to computer running times required for MHOST and MARC 3-D model calculations, MHOST appears to be somewhat faster than MARC for identical problems, geometries, loadings, etc. Time comparisons between the two programs are shown in Figure 3.3-29, where 100 percent of the load was applied in one step (increment) and the number of iterations was varied. The plots here show the MHOST code to be about 40 percent faster than the MARC code for this particular problem setup and loading. This type of time savings for MHOST over MARC (i.e., about 40 percent) is typical of the comparisons that were made, regardless of whether the loading involved one increment and a number of iterations, or vice-versa, a number of increments (adding up to 100 percent load) and zero or one iteration per increment.

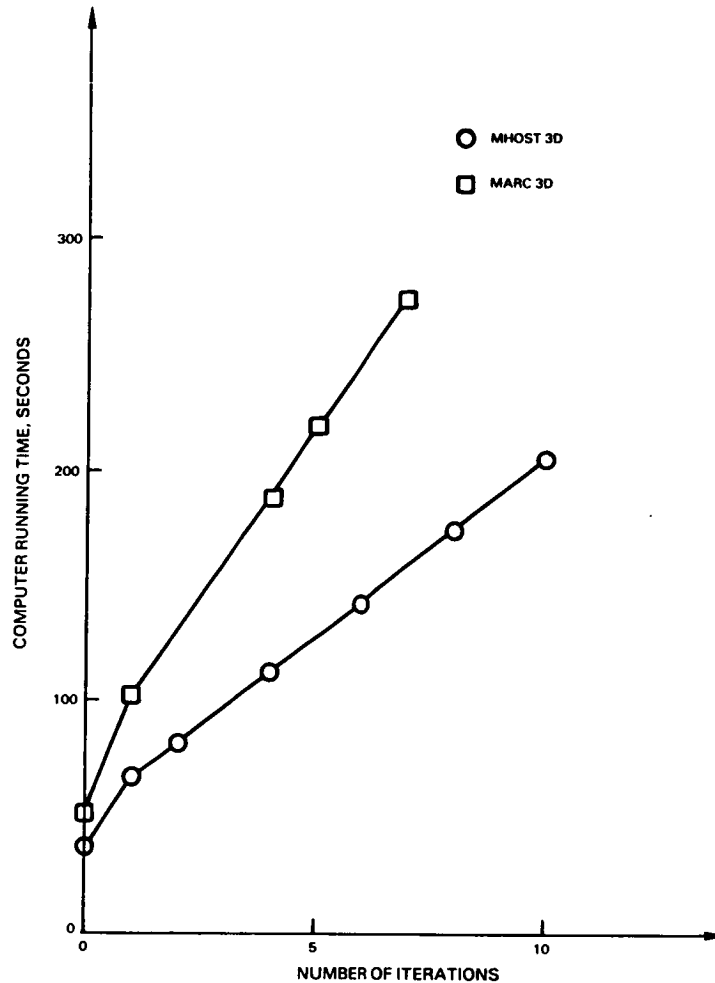


Figure 3.3-29 Computer Running Times for 100 Percent Load in One Step (Three-Dimensional Model)

From the discussion presented in the preceding paragraphs, it can be concluded that the MHOST code, when compared against the MARC code, provides significant accuracy improvement at reduced cost for applications of the blister specimen type.

#### NASA Benchmark Notch Specimen

Three-dimensional elastic-plastic analyses of the NASA Benchmark Notch Specimen have been performed using the MHOST code. In order to avoid duplication, the finite element results for this specimen are discussed together with boundary element method results in Section 3.4.5.7.

### 3.3.8 List of Symbols

<u>Alphabetical Symbol</u>	<u>Description</u>
$\tilde{a}$	Acceleration vector
$a_j$	Acceleration vector component
$\tilde{B}$	Strain-displacement matrix
$\tilde{C}$	Damping matrix
$c$	Geometric constant
$\tilde{D}$	Material modulus matrix
$D_{ijkl}$	Fourth order tensor component of material modulus
$e$	Nodal strain vector
$E$	Young's modulus
$E_R$	Prescribed surface traction vector
$\tilde{f}$	Body force vector
$\tilde{F}$	Node point force vector
$f_j$	Body force vector component
$\tilde{G}$	Gramm matrix for the finite element basis
$\tilde{g}$	Gravity acceleration vector
$h$	Thickness for plates and shells
$I$	Functional
$\tilde{J}$	Jacobian matrix for the isoparametric transformation
$\tilde{K}$	Displacement stiffness matrix
$L$	Lagrangian functional
$\tilde{M}$	Mass matrix
$\tilde{N}$	Finite element basis function

## List of Symbols (continued)

<u>Alphabetical Symbol</u>	<u>Description</u>
$\underline{n}$	Unit normal vector
$n_j$	Cartesian component of the unit normal
$\underline{p}$	Penalty matrix
$Q$	Initial strain terms
$Q'$	Nodal forces generated by initial strains
$R$	Radius
$\underline{R}$	Rotation tensor
$\underline{s}$	Nodal stress vector
$r$	Radial coordinate for the axisymmetric geometry
$\underline{t}$	Traction vector
$t_j$	Traction vector component
$\underline{U}$	Right stretch tensor
$\underline{u}$	Displacement vector
$u_j$	Displacement vector component
$V$	Space for admissible displacement variation
$\underline{v}$	Velocity vector
$\underline{v}_j$	Vector for BFGS update
$v_j$	Velocity vector component
$w$	Lateral deflection
$\underline{w}$	Vector for BFGS update
$\underline{x}$	Position vector
$x_j$	Cartesian component of the position vector

## List of Symbols (continued)

<u>Greek Symbols</u>	<u>Description</u>
$\alpha, \beta, \gamma$	Constants
$\delta$	Kronecker's delta
$\delta$	Displacement at a given point
$\epsilon_{ij}$	Infinitesimal strain tensor
$\xi, \eta, \zeta$	Isoparametric coordinates
$\theta$	Constant
$\lambda, \mu$	Lamé-Navier constants for the isotropic elasticity
$\lambda$	Load factor for the arc-length method
$\nu$	Poisson's ratio
$\rho$	Material density
$\sigma$	Stress tensor
$\sigma_{ij}$	Stress tensor component
$\zeta$	Deviatoric stress tensor
$\zeta_{ij}$	Deviatoric stress tensor component
$\emptyset$	Null set
$\Omega$	Problem domain
$\partial\Omega$	Boundary of the domain
<u>Sub- and Superscripts</u>	<u>Description</u>
e	Quantities defined on each element
h	Finite element approximation
i, j, k, ...	Indices for vector and tensor component (when used as subscripts); iteration and incrementation counter (when used as superscripts)
I, J, K, ...	Nodal point counter

## List of Symbols (continued)

<u>Sub- and Superscripts</u>	<u>Description</u>
L	Local subelement mesh
MAX	Maximum number
s	Shear and transverse shear component
S	Subelement
T (Sub)	Tangent
T (Super)	Transpose
0	Initial quantities

### 3.3.9 References

1. L. R. Herrmann, "Finite Element Bending Analysis of Plates," J. Eng. Mech. Div., ASCE, 93, No. EM-5, 1967, pp. 13-25.
2. E. S. Todd, B. N. Cassenti, S. Nakazawa and P. K. Banerjee, "3-D Inelastic Analysis Methods for Hot Section Components (Base Program) First Annual Status Report," NASA CR-174700, 1984.
3. S. Nakazawa, "Reducible and Irreducible Finite Element Forms for Linearly Constrained Problems in Mechanics," Proceeding of the Fifth Int'l. Conf. of Pres. Ves. Tech., Vol. III, ASME GB00242, 1984.
4. S. Nakazawa, "Mixed Finite Elements and Iterative Solution Procedures," Chap. 21 of Innovative Methods in Nonlinear Problems, (W. K. Liu, T. Belytschko and K. C. Park, eds.), Pineridge Press, Swansea, 1984.
5. O. C. Zienkiewicz, J. P. Vilotte, S. Nakazawa and S. Toyoshima, "Iterative Method for Constrained and Mixed Approximation. An Inexpensive Improvement of F.E.M. Performance," 1984, Institute for Numerical Methods in Engineering, Report No. C/R/489/84, University College of Swansea (to appear in Comp. Meth. Appl. Mech. Eng.).
6. O. C. Zienkiewicz, Li Xi-Kui and S. Nakazawa, "Iterative Solution of Mixed Problems and the Stress Recovery Procedures," Report No. C/R/476/84, Institute for Numerical Methods in Engineering, University College of Swansea, 1984.
7. G. Cantin, G. Loubignac and G. Touzot, "An Iterative Algorithm to Build Continuous Stress and Displacement Solutions," Int. J. Num. Meth. Eng., 12, 1978, pp. 1493-1506.
8. J. C. Simo, R. L. Taylor and K. S. Pister (1984), "Variational and Projection Methods for the Volume Constraint in Finite Deformation of Elastoplasticity," 1984, (to appear in Comp. Meth. Appl. Mech. Eng.).
9. D. S. Malkus and T. J. R. Hughes, "Mixed Finite Element Method - Reduced and Selective Integration Technique: A Unification of Concepts," Comp. Meth. Appl. Mech. Eng., 15, 1978, pp. 63-81.
10. T. J. R. Hughes and D. S. Malkus, "A General Penalty/Mixed Equivalence Theorem for Anisotropic, Incompressible Finite Elements," Chap. 25 of Hybrid and Mixed Finite Element Methods (S. N. Atluri, R. H. Gallagher and O. C. Zienkiewicz, eds.), Wiley, Chichester, 1983.
11. T. J. R. Hughes and T. E. Tezduyar, "Finite Elements Based upon Mindlin Plate Theory with Particular Reference to the Four-Node Bilinear Isoparametric Element," J. Appl. Mech. Trans. ASME, 48, 1981, pp. 587-596.

12. T. Belytschko and C. S. Tsay, "A Stabilization Procedure for the Quadrilateral Plate Element with One-Point Quadrature," Int. J. Num. Meth. Eng., 19, 1983, pp. 405-419.
13. J. T. Oden and H. J. Brauchli, "On the Calculation of Consistent Stress Distributions in Finite Element Approximations," Int. J. Num. Meth. Eng., 3, 1971, pp. 371-325.
14. J. T. Oden and J. N. Reddy, "Note on an Approximate Method for Computing Consistent Conjugate Stresses in Elastic Finite Elements," Int. J. Num. Meth. Eng., 6, 1973, pp. 55-61.
15. I. Babuska and A. Miller, "The Post-Processing Approach in the Finite Element Method - Part 1: Calculation of Displacements, Stresses, and Other Higher Derivatives of the Displacements," Int. J. Num. Meth. Eng., 20, 1984, pp. 1085-1109.
16. I. Babuska and A. Miller, "The Post-Processing Approach in the Finite Element Method - Part 2: The Calculation of Stress Intensity Factors," Int. J. Num. Meth. Eng., 20, 1984, pp. 1111-1129.
17. Y. Owa, "On Stress Recovery in Displacement Finite Element Method," M.Sc. Thesis, University College of Swansea, 1982.
18. S. Nakazawa, Y. Owa and O. C. Zienkiewicz, "On the Nodal Stress Recovery in the Displacement Finite Element Methods," Internal Report, MARC Analysis Research Corporation, 1984, (submitted for publication).
19. J. C. Simo and T. J. R. Hughes, "On the Variational Foundations of Assumed Strain Methods," 1985, (submitted for publication).
20. D. Fyhre and T. J. R. Hughes, "A Literature Survey on Finite Element Methodology for Turbine Hot Section Components," MARC Analysis Research Corporation, Palo Alto, California, 1983.
21. J. C. Nagtegaal and J. E. de Jong, "Some Computational Aspects of Elastic- Plastic Large Strain Analysis," Int. J. Num. Meth. Eng., 17, 1981, pp. 15-42.
22. H. H. Abdel Rahman, "Computational Models for the Nonlinear Analysis of Reinforced Concrete Flexural Slab System," Ph.D. Thesis, University College of Swansea, 1982.
23. H. Matthies and G. Strang, "The Solution of Nonlinear Finite Element Equations," Int. J. Num. Meth. Eng., 14, 1979, pp. 1613-1626.
24. M. Fortin and Glowinski (eds.), Methodes de Lagrangian Augmente, Dunod, Paris, 1982.

25. S. Nakazawa, J. P. Vilotte and O. C. Zienkiewicz, "Variational Formulations and Their Approximations for Incompressible Problems," presented at the Fifth Int'l. Conf. Finite Element in Flow Problems, Austin, Texas, 1984.
26. V. Girault and P. A. Raviart, "Finite Element Approximation of the Navier-Stokes Equations," Lecture Note in Mathematics, Vol. 749, Springer-Verlag, Berlin, 1979.
27. R. Teman, Navier-Stokes Equations, North Holland, Amsterdam, 1977.
28. K. Arrow, L. Hurwicz and H. Uzawa, Studies in Nonlinear Programming, Stanford University Press, Stanford, California, 1958.
29. M. A. Crisfield, "An Iterative Improvement for Non-Conforming Bending Elements," Int. J. Num. Meth. Eng., 9, 1975, pp. 641-648.
30. O. C. Zienkiewicz, The Finite Element Method, 3rd. ed., McGraw Hill, New York, 1977.
31. I. Babuska, "The Finite Element Method with Lagrange Multipliers," Numer. Math., 1973, pp. 179-192.
32. F. Brezzi, "On the Existence, Uniqueness and Approximation of Saddle-Point Problems Arising from Lagrangian Multiplier," RAIRO, R-2, 1974, pp. 129-151.
33. J. T. Oden, "Mixed Methods, Hybrid Methods, and Penalty Methods," Chap. 3 of Series of Textbooks on Finite Element Methods, Vol. 2, (J. T. Oden, et al, eds.), 1981.
34. O. C. Zienkiewicz and S. Nakazawa, "The Penalty Function Method and Its Applications to the Numerical Solution of Boundary Value Problems," AMD Vol. 51, ASME, 1982, pp. 157-179.
35. R. L. Taylor and O. C. Zienkiewicz, "Mixed Finite Element Solution of Fluid Flow Problems," Chap. 1 of Finite Elements in Fluids, Vol. 4, (R. M. Gallagher, D. H. Norrie, J. T. Oden and O. C. Zienkiewicz, eds.), Wiley, Chichester, 1982.
36. O. C. Zienkiewicz and S. Nakazawa, "On Variational Formulation and Its Modifications for Numerical Solution," 1984, (to appear in Int. J. Solid Struct.).
37. A. D. Fine, "Special Finite Element Displacement Formulations for Modeling Singularity Point Behavior," Pratt & Whitney Engineering Division, 1984.
38. B. S. Annigeri, "Surface Integral Finite Element Hybrid Method for Localized Problems in Continuum Mechanics," Ph.D. Thesis, Department of Mechanical Engineering, Massachusetts Institute of Technology, 1984.

39. J. Gago, "A Posteriori Error Analysis and Adaptivity for Finite Element Method," Ph.D. Thesis, University College of Swansea, 1982.
40. O. Axelsson, "Solution of Linear Systems of Equations: Iterative Methods, In 'Sparse Matrix Techniques'," Lecture Notes in Mathematics, Vol. 572, Springer-Verlag, Berlin, 1976.
41. O. Axelsson, "On Iterative Solution of Large Sparse Systems of Equations with Particular Emphasis on Boundary Value Problems," TICOM Report 78-4, The Texas Institute for Computational Mechanics, University of Texas at Austin, 1978.
42. A. Muller and T. J. R. Hughes, "Mixed Finite Element Methods and Iterative Solutions: An Algorithm for Structural Finite Element Analysis," (W. K. Liu, T. Belytschko and K. C. Park, eds.) Innovative Methods for Nonlinear Problems, Pineridge Press, Swansea, 1984.
43. M. A. Crisfield, "A Fast Incremental/Iterative Solution Procedure That Handles 'Snap-Through'," Computational Methods in Nonlinear Structural and Solid Mechanics, Pergamon Press, 1980, pp. 55-62.
44. L. E. Malvern, Introduction to the Mechanics of a Continuous Medium, Prentice Hall, Englewood Cliffs, New Jersey, 1969, pp. 172-174.
45. D. P. Flanagan and T. Belytschko, "A Uniform Strain Hexahedron and Quadrilateral with Orthogonal Hourglass Control," Int. J. Num. Meth. Eng., 17, 1981, pp. 679-706.
46. J. T. Oden, "Stability and Convergence of Underintegrated Finite Element Approximations," Nonlinear Structural Analysis, (ed. C. Chamis), NASA Conference Publication 2297, 1983, pp. 95-103.
47. T. Belytschko, C. S. Tsay and W. K. Liu, "A Stabilization Matrix for Bilinear Mindlin Plate Element," Comp. Meth. Appl. Mech. Eng., 29, 1981, pp. 313-327.
48. R. D. Cook, "Two Hybrid Elements for the Analysis of Thick, Thin and Sandwich Plates," Int. J. Num. Meth. Eng., 5, No. 2, 1972, pp. 277-288.
49. G. M. Lindberg and M. D. Olson, "Dynamic Analysis of Shallow Shells with a Doubly-Curved Triangular Finite Element," J. Sound and Vibration, 19, No. 3, 1971, pp. 299-318.
50. S. Ahmad, B. M. Irons and O. C. Zienkiewicz, "Curved Thick Shell and Membrane Elements with Particular Reference to Axi-symmetric Problems," Proc. 2nd Conf. Matrix Methods in Structural Mechanics, Wright-Patterson Air Force Base, Ohio, 1968.

### 3.4 BOUNDARY ELEMENT METHOD

#### 3.4.1 Overview

It is the goal of the advanced formulation development portion of this program to develop a computational technique for the solution of linear, nonlinear and transient problems in gas turbine engine hot section components. This technique is to be distinct from, and complementary to, the Finite Element Method. The existence of such a computational tool will enhance the ability to calibrate the other codes developed under this contract. In addition, it is to be expected that different techniques will prove optimal, in terms of efficiency or accuracy, for particular types of component analysis. Since almost all general purpose structural analysis computer programs presently available employ the displacement finite element method, the new program developed as part of the advanced formulation development effort can be expected to extend the ability to perform realistic analyses of hot section components.

During the first year of this program (Task IC), Pratt & Whitney and its subcontractor, the State University of New York at Buffalo (SUNY-B), developed a new general purpose structural analysis program, BEST3D (Boundary Element Stress Technology), based on the use of the Boundary Element Method (BEM). During this work, the boundary element method was implemented for very general three-dimensional geometries, for elastic, inelastic and dynamic stress analysis problems.

In the second year of the program (Task IIC), Pratt & Whitney and SUNY-B have continued the theoretical and numerical development and the computer implementation of the BEM, making very significant advances in a variety of areas. Major developments accomplished during Task IIC include:

1. Incorporation of substructuring capability in the nonlinear BEM stress analysis.
2. Algorithm development, coding and validation of an embedded time algorithm for elastodynamic problems.
3. Development of a method for representing the effects of embedded discontinuities without explicit boundary modeling.
4. Development and two-dimensional testing of an algorithm for the calculation of the natural frequencies and mode shapes of a structure, and the preliminary design for incorporating this capability in BEST3D.
5. Significant improvement in the accuracy and efficiency of many of the numerical algorithms in BEST3D.
6. Verification of the nonlinear solution capabilities of BEST3D using externally generated data.

The second year development effort is discussed in more detail below. Section 3.4.2 updates the results of the BEM literature survey originally conducted during Task IC. Section 3.4.3 summarizes new developments in the analytical and numerical formulation of the BEM for elastic, inelastic and dynamic problems in three dimensions. Modifications to the BEST3D code are discussed in Section 3.4.4. Validation/verification of BEST3D is discussed in Section 3.4.5.

### 3.4.2 Literature Survey Update

During 1984, no boundary element papers have been published that are likely to cause significant redirection of work in the Inelastic Methods Program. It appears that the boundary element technology used in BEST3D for multiregion isotropic and anisotropic elastic stress analyses, multiregion dynamic (steady-state and transient time domain) analyses and multiregion inelastic analyses under monotonic and cyclic loading remains at least current with the published literature.

A comprehensive textbook by Brebbia et al (Reference 1) and an advanced monograph edited by Banerjee and Mukherjee (Reference 2) appeared in 1984, and essentially document the state-of-the-art. Additionally, Ingrafia (Reference 3) described the use of special shape functions for fracture mechanics analysis, along lines originally explored by Cruse and Wilson (Reference 4). Rizzo et al (Reference 5) described dynamic analysis of some earth structures problems involving single homogeneous regions using the Fast Fourier Transform. Brebbia and Nardini (Reference 6) have explored the calculation of natural frequencies in single region, two-dimensional boundary element analysis.

### 3.4.3 Formulation Development

#### 3.4.3.1 Summary

Important advances have been made during Task IIC in extending the BEM formulation for three-dimensional stress analysis of gas turbine engine structures. The most significant formulation advances have been in the area of dynamic analysis, where a real variable, time embedded technique has been developed, in the calculation of natural frequencies and mode shapes, in the representation of multiple embedded discontinuities and in the basic understanding of numerical algorithms employed in the BEM. These extended or newly developed formulations are discussed in the subsections below. The basic BEM formulation is only very briefly reviewed, as full details are available in the First Annual Status Report (NASA CR-174700).

### 3.4.3.2 Linear and Nonlinear Stress Analysis

#### 3.4.3.2.1 Review

By making use of the reciprocal work theorem, the governing differential equations for a three-dimensional (homogeneous) structure under combined thermal, mechanical and body force loadings can be converted to an integral equation written on the surface of the structure. This integral equation is:

$$c_{ij} u_i = \int_S [G_{ij} t_i - F_{ij} u_i] ds + \int_V (G_{ij} f_i + \beta W_j T) dv \quad (3.4-1)$$

where  $W_j = T_{ikj} \delta_{ik}$ ,  $\beta =$  coefficient of thermal expansion,

$T_{ikj}$  = the stress  $\sigma_{ik}$  due to a point force  $e_j$ ,

$G_{ij}$ ,  $T_{ikj}$  and  $F_{ij}$  are defined in the First Annual Status Report (NASA CR-174700),

and

$$\sigma_{ij} = \int_S [D_{ijk} t_k - S_{ijk} u_k] ds + \int_V (T_{ijk} f_k + M_{ij} T) dv \quad (3.4-2)$$

allows calculation of stresses at any interior point where they are required. A similar equation for interior displacements can be obtained by setting  $c_{ij} = \delta_{ij}$  in equation (3.4-1).

In a purely elastic problem BEM stress analysis can be carried out entirely on the boundary of the structure. Once a physically reasonable set of boundary conditions has been prescribed, equation (3.4-1) can, in principle, be solved for all of the remaining boundary displacements and tractions.

It is generally impossible to solve equation (3.4-1) exactly for real structures and loading conditions. Suitable approximations of the boundary geometry, displacements and tractions must be used in order to reduce equation (3.4-1) to a system of algebraic equations. The present version of BEST3D

models boundary geometry and boundary values of field quantities using linear and/or quadratic isoparametric shape functions. The surface integrals in equation (3.4-1) are then evaluated numerically using product Gaussian quadrature rules. The numerical implementation of the BEM is discussed in detail in textbooks by Banerjee and Butterfield, and by Brebbia as well as in the First Annual Status Report (NASA CR-174700).

In the case of inelastic analysis, the volume integrals in equation (3.4-1) cannot be calculated a priori, since they require knowledge of inelastic strain, which is itself a part of the solution. In this case equations (3.4-1), (3.4-2) and the inelastic material model can be regarded as a coupled system of nonlinear equations. In the numerical implementation of the BEM equation (3.4-2) is used to calculate the stresses at interior points, and the nonlinear material model is then used to evaluate inelastic strain. Since the volume integrals of inelastic strain vanish except in regions of nonlinear material response, approximations of geometry and field quantities are required only where nonlinearity is expected. In BEST3D volume models utilize quadratic isoparametric shape functions or simple rectilinear cells. In the first case the isoparametric shape functions are also used to model inelastic strain variation. In the second case an exact solution for the uniform initial strain problem, discussed in Section 3.4.3.2.6, is used.

The remainder of Section 3.4.3.2 discusses significant new developments carried out during Task IIC.

#### 3.4.3.2.2 Redefinition of Plasticity Formulation

In the First Annual Status Report (NASA CR-174700) the plasticity formulation was defined with respect to a known distribution of initial strain. It has been found to be more convenient to define the displacement field in terms of the initial stresses defined over the volume, so that:

$$c_{ij} \dot{u}_i(x_0) = \int_S [G_{ij}(x, x_0) \dot{t}_i(x) - F_{ij}(x, x_0) \dot{u}_i(x)] d\Gamma + \int_V B_{ikj}(z, \xi) \sigma_{ik}^0(z) dv \quad (3.4-3)$$

$$\text{where } B_{ikj} = - \frac{1}{16\pi\mu(1-\nu)} \frac{1}{r^2} \left[ (1-2\nu) \left( \delta_{ik} \frac{y_j}{r} - \delta_{jk} \frac{y_i}{r} \right) - \delta_{ij} \frac{y_k}{r} + \frac{3y_i y_j y_k}{r^3} \right]$$

The stresses at an interior point can be obtained from

$$\dot{\sigma}_{ijk} = \int_S [D_{ijk} \dot{t}_i - S_{ijk} \dot{u}_i] ds + \int_V E_{ipjk} \dot{\sigma}_{ip}^0 dv + J_{ipjk} \dot{\sigma}_{ip}^0 \quad (3.4-4)$$

where the last term on the right-hand side of equation (3.4-4) is the principal value. The kernels D and S are defined in Banerjee and Butterfield and

$$E_{ipjk} = \frac{C_3}{(\alpha-1)r^\alpha} [C_4(\delta_{ip} \delta_{jk} - \delta_{ij} \delta_{kp} - \delta_{ik} \delta_{jp} - \alpha \delta_{jk} y_i y_p) - \alpha \delta_{ip} y_j y_k - \alpha v(\delta_{ij} y_k y_p + \delta_{ik} y_j y_p + \delta_{jp} y_i y_k + \delta_{kp} y_i y_j) + \alpha(\alpha+2) y_i y_j y_k y_p]$$

$$C_3 = -1/4\pi (1-\nu)$$

$$J_{ipjk} = \frac{C_4}{\alpha(\alpha+2)} \left[ [(\alpha^2 - 2) - \nu(\alpha^2 - 4)] \delta_{ij} \delta_{kp} + [1 - \nu(\alpha + 2) \delta_{ip} \delta_{jk}] \right]$$

$$C_4 = -1 / (1 - \nu) , \quad \alpha = 3$$

Equations (3.4-3) and (3.4-4) provide the formal basis for developing the plasticity algorithm. The initial stresses  $\sigma_{ij}^0$  defined in equations (3.4-3) and (3.4-4) include the effects of all inelastic strains (thermal, plastic and creep). The magnitude of the initial strain, however, is not known a priori (except for the thermo-elastic problem) and must be determined by satisfying the constitutive relations.

### 3.4.3.2.3 Plasticity Solution Sequence

The displacement and stress equations at the boundary (equations 3.4-3 and 3.4-4) and interior points can be assembled to arrive at the system equations as:

$$U^b \dot{t}^b - T^b \dot{u}^b + E^b \dot{\sigma}^{o(b+i)} = 0$$

$$\dot{u}^i = U^i \dot{t}^b - T^i \dot{u}^b + E^i \dot{\sigma}^{o(b+i)} \quad (3.4-5)$$

$$\dot{\sigma} = U^\sigma \dot{t}^b - T^\sigma \dot{u}^b + E^\sigma \dot{\sigma}^{o(b+i)}$$

where  $\dot{u}$  ,  $\dot{t}$  ,  $\dot{\sigma}^0$  are the displacement, traction and initial stress increment vectors. The superscripts b, i in the above equations indicate reference to boundary and interior node related equations.

By collecting the known (y) and unknown (x) values of traction and displacement rates and their coefficients together, the above equations can be recast as:

$$A^b \dot{x} = B^b \dot{y} + C^b \dot{\sigma}^0 = \dot{b}^b + \dot{b}^{ob}$$

$$\dot{u}^i = A^i \dot{x} + B^i \dot{y} + C^i \dot{\sigma}^0 = A^i \dot{x} + \dot{b}^i + \dot{b}^{oi} \quad (3.4-6)$$

$$\dot{\sigma} = A^\sigma \dot{x} + B^\sigma \dot{y} + C^\sigma \dot{\sigma}^0 = A^\sigma \dot{x} + \dot{b}^\sigma + \dot{b}^{o\sigma}$$

The algorithms described yield the solution of the system defined by (3.4-6) together with the constitutive model. This includes complete knowledge of the initial stress distribution  $\dot{\sigma}^0$  within the yielded region. Since  $\dot{\sigma}^0$  is not known a priori for a particular load increment and since the complete system is nonlinear, an iterative process is employed within each loading stage.

An important feature incorporated in all the iterative algorithms in the present work is the utilization of the initial stresses generated by the past history. In this procedure, the path followed by the previous load increment is used to extrapolate the initial stresses at the beginning of the current increment before the iterative operations. This substantially reduces the computer time.

The incremental algorithm can be described as follows:

- (a) Obtain the elastic solution for an arbitrary increment of boundary loading  $\dot{y}$  from

$$\dot{x} = [A^b]^{-1} \dot{b}^b$$

$$\dot{u}^i = A^i \dot{x} + \dot{b}^i$$

and

$$\dot{\sigma} = A^\sigma \dot{x} + \dot{b}^\sigma$$

- (b) Scale the elastic solution such that the highest stressed node is at yield.
- (c) Impose a small load increment  $\dot{y}$  (usually about five percent of the yield load) and an initially estimated value  $\dot{\sigma}^0$  based on the previously generated history of initial stress and evaluate

$$\dot{x} = [A^b]^{-1} \dot{b}^b + \dot{b}^{0b}$$

and

$$\dot{\sigma} = A^\sigma \dot{x} + \dot{b}^\sigma + \dot{b}^{0\sigma}$$

It should be noted that at the first load step, the initial stresses are zero since no prior plastic history exists.

- (d) Accumulate all incremental quantities computed in the previous step.
- (e) Evaluate the current constitutive matrix using the new history and incremental values and calculate the initial stress rates and accumulate them.

- (f) Return to step (c) and apply the next load step with non-zero  $\dot{b}^0$ , if the current increments of initial stresses are less than a suitable error norm (normally 0.005 times the yield stress).
- (g) Return to step (c) and compute the incremental quantities due to initial stress only (i.e., boundary loading change is zero).

If the number of iterations executed is greater than a specified limiting value (usually 50), the system is assumed to have reached the state of collapse.

The plastic solution algorithm is summarized in Figure 3.4-1.

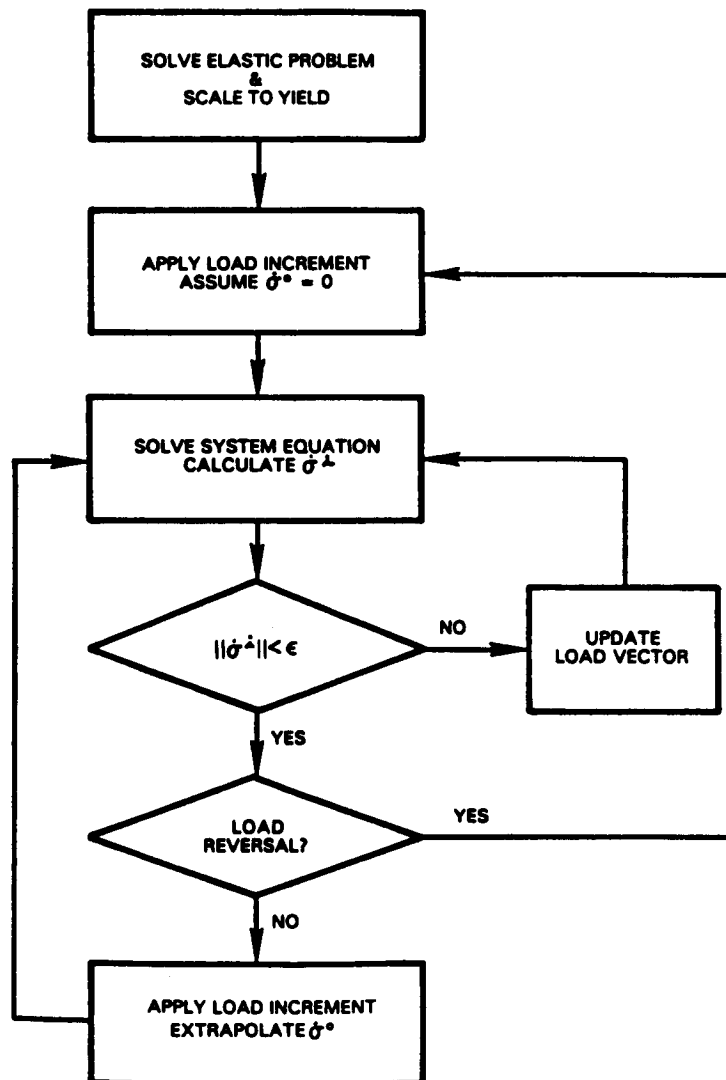


Figure 3.4-1 Plasticity Solution Sequence

#### 3.4.3.2.4 Inelastic Material Models

The three constitutive models which are presently included in BEST3D are:

- (a) Von Mises model with isotropic variable hardening
- (b) Two-surface model for cyclic plasticity
- (c) Combined plasticity and creep model of Walker.

Of these, the models (a) and (c) are described in the earlier sections of this report. The two-surface model used here is similar to that described by Krieg except that a new form of hardening function has been introduced.

In the two-surface model, it is assumed that during loading in the plastic state the stress state remains in contact with the inner yield surface, known as the loading surface. The outer surface, known as the limiting or bounding surface, is allowed to follow hardening rules identical to those of elastic, linearly hardening isotropic or kinematic plastic theory.

The hardening of the loading surface depends on a distance vector that joins the stress state to the bounding surface such that the system is very stiff when the stress state is remote from the bounding surface and assumes essentially the hardening values of the bounding surface when the stress state is in the proximity of this surface. This variation of stiffness from large to small asymptotic values allows a smooth transition while the stress state moves through three distinct zones: an elastic region which is associated with recoverable strains when the stress state is within the loading surface, a plastic region where the system adopts the stiffness of the bounding surface, and an in-between metaelastic region when the stress state is on the loading surface but inside the bounding surface.

The behavior in the elastic and plastic region is governed by the stress strain relations:

$$d\underset{\sim}{\sigma} = \left[ \underset{\sim}{D}^e - \frac{\underset{\sim}{D}^e \left( \frac{\partial F}{\partial \underset{\sim}{\sigma}^*} \right) \left( \frac{\partial F}{\partial \underset{\sim}{\sigma}^*} \right)^T \underset{\sim}{D}^e}{H_p + H_e} \right] d\underset{\sim}{\epsilon} \quad (3.4-7)$$

where  $\underset{\sim}{\sigma}^*$  is the reference point on the boundary surface corresponding to the stress point  $\underset{\sim}{\sigma}$  (as defined by Mroz in 1967). The function  $F$  used in this development is the standard yield function of Von Mises.

In equation (3.4-7) the terms  $H_p$  and  $H_e$  are defined as:

$$H_e = \left( \frac{\partial F}{\partial \underset{\sim}{\sigma}^*} \right)^T \underset{\sim}{D}^e \left( \frac{\partial F}{\partial \underset{\sim}{\sigma}^*} \right)$$

and

$$H_p = h \left( \frac{\bar{\sigma}}{\sigma_{ref}} \right)^n, \quad h, n \text{ and } \sigma_{ref} \text{ are material parameters}$$

$\bar{\sigma}$  is the distance (in six-dimensional stress space) between the current stress point and the last elastic location of the loading surface center.

Any unloading during the deformation is indicated by

$$dL = \underset{\sim}{n}^T d\underset{\sim}{\sigma} < 0 \text{ where } \underset{\sim}{n} \text{ is the unit normal at } \underset{\sim}{\sigma}^*$$

$$\underset{\sim}{n} = \left( \frac{\partial F}{\partial \underset{\sim}{\sigma}^*} \right) / \left[ \left( \frac{\partial F}{\partial \underset{\sim}{\sigma}^*} \right)^T \left( \frac{\partial F}{\partial \underset{\sim}{\sigma}^*} \right) \right]^{1/2}$$

which leads to a purely elastic response until the loading path touches the loading surface when once again a new reference point  $\underset{\sim}{\sigma}^*$  is established.

### 3.4.3.2.5 Multi-GMR (Generic Modeling Region) Plasticity Algorithm

In the case of a multiregion problem, the system matrices for the boundary nodes for each region are organized as:

$$\underset{\sim}{A}x + \underset{\sim}{B}y + \underset{\sim}{C}\sigma^0 = 0$$

$$\text{or } \underset{\sim}{A}x = -(\underset{\sim}{B}y + \underset{\sim}{C}\sigma^0) = \underset{\sim}{b} \quad (3.4-8)$$

Equation (3.4-8) is identical in nature to the corresponding system equations for the multi-GMR elastic problem and therefore can be used in the multiregion assembly and solution scheme without any change. The iterative process used does require an efficient process for the repeated solution of the algebraic system (3.4-8).

### 3.4.3.2.6 Embedded Hot Spots and Discontinuities

An exact solution for the case of uniform initial stress or initial strain in a rectilinear cell of dimensions  $a \times b \times c$  has been derived, based on the stress solution in Reference 7. This solution can be expressed as:

$$u_j(\xi) = B_{ikj}^0(x, \xi) \sigma_{ik}^0(x) \quad (3.4-9)$$

$$\text{and } \sigma_{jl}(\xi) = M_{ijk1}(x, \xi) \sigma_{ik}^0(x) \quad (3.4-10)$$

It is important to note the following features of the above equations for displacements and stresses:

- (a) there is no integration required
- (b) equations (3.4-9) and (3.4-10) can be added directly to the respective boundary integral equations for the displacements at the boundary and interior points and for the stresses at interior points.

For a hot spot equations (3.4-9) and (3.4-10) simplify to:

$$u_i(\xi) = H_i(x, \xi) T(x) \quad (3.4-11)$$

$$\sigma_{ij}(\xi) = J_{ij}(x, \xi) T(x) \quad (3.4-12)$$

where  $T(x)$  is the temperature of a hot spot of volume  $a \times b \times c$ . In the presence of hot spots equation (3.4-8) is modified to

$$\underset{\sim}{A}x + \underset{\sim}{B}y + \underset{\sim}{C}\sigma^0 + \underset{\sim}{H}T = 0 \quad (3.4-13a)$$

$$\text{or } \underset{\sim}{A}x = -(\underset{\sim}{B}y + \underset{\sim}{C}\sigma^0 + \underset{\sim}{H}T) = \underset{\sim}{b} \quad (3.4-13b)$$

Equation (3.4-13) can be formed for each generic modeling region (GMR) and used in the solution. Discontinuities are allowed without having any formal discretization by simply assuming that the stresses within the volume occupied by it are zero. Thus, for example, in an elastic system if we introduce an arbitrary initial stress system  $\sigma^0$  within the discontinuities, then the boundary displacement equations and the interior stress equations at a point within a discontinuity can be written as:

$$\underset{\sim}{A}x + \underset{\sim}{B}y + \underset{\sim}{C}\sigma^0 = 0 \quad (3.4-14a)$$

$$\underset{\sim}{\sigma} = 0 = \underset{\sim}{A}^\sigma x + \underset{\sim}{B}^\sigma y + \underset{\sim}{M}\sigma^0 \quad (3.4-14b)$$

By eliminating  $\sigma^0$  between equations (3.4-14a) and (3.4-14b),

$$\underset{\sim}{A}x + \underset{\sim}{B}y - \underset{\sim}{C}M^{-1}(\underset{\sim}{A}^\sigma x + \underset{\sim}{B}^\sigma y) = 0$$

$$\text{or } (\underset{\sim}{A} - \underset{\sim}{C}M^{-1}\underset{\sim}{A}^\sigma) x = (\underset{\sim}{C}M^{-1}\underset{\sim}{B}^\sigma - \underset{\sim}{B}) y$$

$$\text{or } \underset{\sim}{\bar{A}}x = \underset{\sim}{\bar{b}} \quad (3.4-15)$$

Equation (3.4-15) can be formed for each GMR and solved as before.

It should be noted that displacements and stresses near the void change significantly as a result of its presence. This is due to the fact that both the boundary solution ( $\underline{x}, \underline{y}$ ) and the initial stress ( $\sigma_0$ ) occur in both equations (3.4-14a) and (3.4-14b).

#### 3.4.3.2.7 Anisotropic Elastic Materials

The ability to perform stress analysis for materials whose elastic behavior is anisotropic is of considerable importance in the study of hot section components. Such anisotropy can occur in three ways:

- (1) Because processing (such as rolling or forging) induces anisotropic behavior in an originally isotropic alloy.
- (2) Because cast components are subjected to a cooling sequence designed to produce an anisotropic (single crystal or transversely isotropic alloy).
- (3) Because a material can exhibit elastic anisotropy due to prior non-linear deformation.

The application of the boundary element method to such materials requires a number of modifications. In particular, the following items require attention:

- (1) The point load solution for the (generally oriented) anisotropic material must be available analytically and calculable numerically.
- (2) Modifications must be made to the surface stress calculation.
- (3) New particular integrals for centrifugal body forces are required.

Substantial progress was made during Task IIC in extending BEST3D to include anisotropic materials.

It has long been known that the point load solution for a general anisotropic material can be represented in terms of a line integral,

$$U_{ij}(\underline{x} - \underline{y}) = \frac{1}{8\pi^2 |\underline{x} - \underline{y}|} \oint K_{ij}^{-1}(\xi) ds \quad (3.4-16)$$

where,

$$K_{ij}(\xi) = C_{ijkl} \xi_k \xi_l$$

$$C_{ijkl} = \text{elastic constants}$$

and the integration path lies on the unit sphere and is perpendicular to the vector  $(\underline{x} - \underline{y})$ .

In an earlier program (Reference 8), a technique was developed to tabulate the point load functions for directionally solidified (transversely isotropic) and eutectic (single crystal) materials. The tabulated results were then numerically interpolated within a boundary element method code whenever kernel function values were required. It was found that this method allowed accurate solution of stress analysis problems for both material types. The numerical evaluation of the kernel function was, however, considerably more expensive than the evaluation of the isotropic Kelvin solution, and led to an increase in solution time of about 100 percent.

It is not known for exactly what forms of anisotropy equation (3.4-16) has a closed form solution. A condition for the existence of such a solution based on the root structure of a sixth degree polynomial involving the elastic constants has been conjectured (Reference 9), but not yet published. At present the only known closed form solutions are those for the isotropic (Kelvin solution) and transversely isotropic cases.

The transversely isotropic solution (Reference 10) was derived using stress functions involving complex variables. The original formulation was reviewed and considerably simplified before incorporation in BEST3D. In particular, the general form of Reference 10 includes within it a number of special cases,

only one of which is relevant to directionally solidified alloys presently in use in gas turbine engines. This fact was used to reduce significantly the amount of calculation required.

The case of the single crystal material must still be handled using an approximate representation of equation (3.4-16). New methods for this approximation, requiring less storage and calculation than the technique reported in Reference 8 are being developed as part of Tasks IVC and VC.

In Task IC the effect of a centrifugal load on an isotropic material was evaluated using a particular solution of the equilibrium equations. The particular solution has now been generalized for an arbitrary anisotropic material. If a body rotates about an axis passing through an origin, then the equilibrium equations are:

$$\tau_{ij,j} = f_i \quad (3.4-17)$$

where

$$\underline{f} = (\rho\omega^2x, \rho\omega^2y, 0)$$

$\rho$  = density

$\omega$  = speed of rotation.

For simplicity in the presentation, the axis of rotation has been taken to be the z-axis. The problem can always be transformed to this case within the code. Such a transformation requires a corresponding transformation of the  $C_{ij}$  matrix, which can then become a full, symmetric matrix, even for transversely isotropic or single crystal materials.

By analogy with the known particular solution for the isotropic case, the displacements of the anisotropic particular solution are assumed to have cubic variation in the Cartesian coordinates, for example:

$$U_1 = A_1x_1^3 + A_2x_1^2x_2^2 + A_3x_1x_3^2 \quad (3.4-18)$$

where the coefficients are to be determined. Differentiation of (3.4-18) allows the determination of the strains (quadratic functions of the coordinates). The stresses are then determined, using the transformed Hooke's law, and a further differentiation allows the evaluation of the left-hand side of (3.4-17) in terms of the undetermined coefficients. Equation (3.4-17) is linear in the Cartesian coordinates, and must be satisfied for an arbitrary choice of coordinates. This condition leads to a set of nine linear equations in the nine undetermined coefficients. This determination of coefficients is done only once for each subregion within a multiregion structure. Once the coefficients in (3.4-17) have been determined, the anisotropic particular solution is used in exactly the same manner as the isotropic solution.

### 3.4.3.3 Transient and Dynamic Stress Analysis

#### 3.4.3.3.1 Review

One of the goals of the advanced formulation development portion of the inelastic methods program is the development of a three-dimensional boundary element capability for transient and dynamic analysis. Several different problem types are of interest in the dynamic and transient analysis of gas turbine engine hot section components. The primary areas of interest are:

- (1) Determination of natural frequencies, and corresponding mode shapes, for geometrically complex structures.
- (2) Evaluation of the response of a structure to a periodic loading (particularly near a natural frequency).
- (3) Determination of the time history of the response to a transient, nonperiodic loading.

The first two problem types are related primarily to the avoidance of structural problems due to forced vibration. The final type of analysis is normally used to predict the effect of unusual, and potentially very damaging, events such as impact by foreign objects.

During Task IC, the problem of dynamic/transient response was attacked by applying the boundary element method (BEM) to a transformed (Laplace or Fourier) form of the governing differential equations. Since a point load solution exists for the transformed equations, the overall framework of the static elastic solution could also be employed for the solution of dynamic/transient problems. The version of BEST3D delivered at the end of Task IC included the capability for this transform domain solution. The proper execution and accuracy of this approach was demonstrated using a number of test problems. The analytical and numerical development of this capability are discussed in considerable detail in the First Annual Status Report (NASA CR-174700).

While the transform approach is capable of providing accurate solutions to dynamic/transient problems, it suffers from serious defects as a practical analysis method for complex structures. The most serious of these are:

- (1) Since the Laplace/Fourier transform casts the entire problem in the complex domain, the storage and computer time requirements are considerably increased. Typically, the solution for a single value of the transform parameter will cost two to four times a single static analysis for the same boundary mesh.
- (2) Any problem with nonperiodic loads must be solved by taking transforms of the loads, solving the transformed BEM problem for multiple values of the transform parameter, and then numerically inverting to reconstruct the time domain solution. Since the transform parameter is embedded nonlinearly in the point load solution, the BEM solution for each transform parameter value requires a complete reconstruction of the system equations, leading to extremely long computing times.
- (3) Since the frequency is involved nonlinearly, natural frequencies can be determined only through some form of a search procedure, a very expensive technique.

It was clear that, while the transform/complex variable method did solve the mathematical problem, new techniques would be required for a practical extension of the BEM method to dynamic and transient problems. Very significant progress has been made in this area during Task IIC. In particular:

- (1) A real variable technique for the calculation of natural frequencies and mode shapes, originally developed for single region, two-dimensional analysis has been significantly improved, and tested in a two-dimensional BEM program. An extension of the method to multiregion three-dimensional problems has been developed.
- (2) A real variable, time embedded formulation for the transient elastic problem has been developed and implemented in BEST3D.

These developments are discussed in the following sections.

#### 3.4.3.3.2 Calculations of Natural Frequencies and Mode Shapes

The governing differential equation is

$$(\lambda + \mu) \frac{\partial^2 u_i}{\partial x_i \partial x_j} + \mu \frac{\partial^2 u_j}{\partial x_i \partial x_i} + \rho \omega^2 u_j = 0$$

which can be written in operator notation as

$$L(u_j) + \rho \omega^2 u_j = 0 \quad (3.4-19)$$

The solution can be formally represented as the sum of a complementary function  $w_j$  satisfying

$$L(w_j) = 0 \quad (3.4-20)$$

and a particular integral  $v_j$  satisfying

$$L(v_j) + \rho \omega^2 u_j = 0 \quad (3.4-21)$$

This equation, however, still contains the unknown displacement field  $u_j$ , which must be eliminated by a suitable approximation. Representing  $u_j$  as

$$u_j(x) = \sum_{m=1}^{\infty} c_{jk}(x, \xi^m) \phi_k(\xi^m) \quad (3.4-22)$$

where  $c_{jk}$  is a function (like a kernel function) and  $\phi_k^m$  are a family of known functions, equation (3.4-21) can be modified to give

$$L(v_j) + \rho\omega^2 \sum_{m=1}^{\infty} c_{jk}(x, \xi^m) \phi_k(\xi^m) = 0 \quad (3.4-23)$$

The function  $c_{jk}(x, \xi^m)$  is then chosen as

$$c_{jk}(x, \xi^m) = A \delta_{jk} (1 - r^m/A) \quad (3.4-24)$$

where  $A$  is a constant and  $r^m$  is the distance between a boundary point and a set of reference points  $m$  on the boundary or in the interior.

A particular integral can then be obtained in the form

$$v_j(x) = \rho\omega^2 \sum_{m=1}^{\infty} D_{jk}(x, \xi^m) \phi(\xi^m) \quad (3.4-25)$$

to satisfy equation (3.4-23). For the boundary points, the particular integral can be expressed as

$$\underset{\sim}{v} = \rho\omega^2 \underset{\sim}{D} \underset{\sim}{\phi} \quad (3.4-26)$$

Once the displacement field due to the particular integral is known, the surface traction due to this displacement field can be expressed as

$$\underset{\sim}{t}^v = \rho\omega^2 \underset{\sim}{T} \underset{\sim}{\phi}$$

The final system of equations for the eigenvalue problem can be then constructed using the particular solution (3.4-26) and the standard boundary element formulation as:

$$\underline{\underline{G}} \underline{\underline{t}} - \underline{\underline{F}} \underline{\underline{u}} = \rho \omega^2 [\underline{\underline{G}} \underline{\underline{T}} \underline{\underline{\phi}} - \underline{\underline{F}} \underline{\underline{D}} \underline{\underline{\phi}}] = \rho \omega^2 [\underline{\underline{G}} \underline{\underline{T}} - \underline{\underline{F}} \underline{\underline{D}}] \underline{\underline{\phi}} \quad (3.4-27)$$

$\underline{\underline{\phi}}$  can be eliminated from equation (3.4-27) by invoking the matrix form of equation (3.4-22), i.e.,

$$\underline{\underline{u}} = \underline{\underline{C}} \underline{\underline{\phi}} \quad \text{or} \quad \underline{\underline{\phi}} = \underline{\underline{C}}^{-1} \underline{\underline{u}} \quad (3.4-28)$$

Substituting (3.4-28) in (3.4-27), leads to:

$$\underline{\underline{G}} \underline{\underline{t}} - \underline{\underline{F}} \underline{\underline{u}} = \rho \omega^2 [\underline{\underline{G}} \underline{\underline{T}} - \underline{\underline{F}} \underline{\underline{D}}] \underline{\underline{C}}^{-1} \underline{\underline{u}} = \rho \omega^2 \underline{\underline{M}} \underline{\underline{u}} \quad (3.4-29)$$

By incorporating the known and unknown boundary values, equation (3.4-29) can be recast into:

$$\underline{\underline{A}} \underline{\underline{x}} + \rho \omega^2 \underline{\underline{B}} \underline{\underline{x}} = 0 \quad (3.4-30)$$

where  $\underline{\underline{x}}$  is the vector of unknown boundary displacements and tractions, and  $\underline{\underline{A}}$  and  $\underline{\underline{B}}$  are two nonsymmetric fully populated matrices. It should be noted that the matrix  $\underline{\underline{A}}$  is identical to the system matrix of an ordinary elastic problem.

#### 3.4.3.3.3 Time Embedded Transient Dynamic Formulation

The boundary integral formulation at boundary point  $\xi$  for a general transient elastodynamic problem is given by

$$[\delta_{ij} - c_{ij}] u_j(\xi, t) = \int_S [G_{ij}^* t_i - F_{ij}^* u_i] ds(x) \quad (3.4-31)$$

where

$$G_{ij}^* t_i = \int_0^t G_{ij}(x, t; \xi, \tau) t_i(x, \tau) d\tau$$

$$F_{ij}^* u_i = \int_0^t F_{ij}(x, t; \xi, \tau) u_i(x, \tau) d\tau$$

are Riemann convolution integrals where the body has been assumed to have been excited from rest. The functions  $G_{ij}$  and  $F_{ij}$ , which represent the displacements and surface tractions at a point  $(x,t)$  due to a unit force vector acting at a point  $\xi$  at a time  $\tau$  within a three-dimensional solid of infinite extent, are analytically too complex to reproduce here (see Banerjee and Butterfield).

Equation (3.4-31) represents an exact formulation involving integrations over the surface as well as the time history. Equation (3.4-31) is an implicit time domain formulation since the displacements at a time  $t$  are calculated taking account of the history of surface tractions and displacements up to and including the time  $t$ . Therefore, if grossly simplified assumptions are not made in the time variations of quantities, the stability problems encountered in the finite difference and the finite element methods should not arise.

If the response at a time  $t$  is to be determined and the time domain has been represented by  $N$  nodes (with the node 1 at time  $t = 0$  and the node  $N$  at time  $t$ ), equation (3.4-31) can be rewritten as

$$\begin{aligned}
 [\delta_{ij} - c_{ij}] u_j(\xi, t_N) - \int_{t_{N-1}}^{t_N} \int_S [G_{ij} t_i - F_{ij} u_i] ds \\
 = \int_0^{t_{N-1}} \int_S [G_{ij} t_i - F_{ij} u_i] ds d\tau \\
 = \int_{t_1=0}^{t_2} \int_S [***] ds d\tau + \int_{t_2}^{t_3} \int_S [***] ds d\tau + \dots \\
 + \int_{t_{N-2}}^{t_{N-1}} \int_S [***] ds d\tau
 \end{aligned} \tag{3.4-32}$$

where  $[***]$  denotes  $[G_{ij} t_i - F_{ij} u_i]$ .

It is of interest to note that equation (3.4-32), like equation (3.4-31), is still an exact formulation of the problem since no approximation has yet been introduced.

By integrating analytically over the time intervals and introducing a spatial discretization in the usual manner, (3.4-32) can be expressed as

$$\underline{\underline{A}}x(t) = \underline{\underline{B}}y(t) - \sum [\underline{\underline{A}}^N \underline{\underline{x}}^N - \underline{\underline{B}}^N \underline{\underline{y}}^N] \quad (3.4-33)$$

where the terms involved in the indicated sum include the effects of past dynamic excitation history on the boundary (i.e., from times  $t = 0$  to  $t = t_{N-1}$ ).

If the time steps are kept constant, the left-hand side of the system equation needs to be generated only once, while the right-hand side is newly calculated for each time step, up to a maximum time. After this maximum time is reached no further integration is required, no matter how many time steps are taken. The maximum time can be calculated based on the wave speeds of the material and the dimensions of the structure. Equation (3.4-33) can be written formally for each generic modeling region (GMR) as:

$$\underline{\underline{A}}x(t) = \underline{\underline{b}}(t) \quad (3.4-34)$$

which can be assembled for each GMR and solved for a multi-GMR problem in the usual manner.

### 3.4.4 Computer Program Development

#### 3.4.4.1 Introduction

The computer program BEST3D was developed during Task IC to provide a tool for applying the three-dimensional boundary element method (BEM) to the elastic, inelastic and dynamic structural analysis of gas turbine engine hot section components.

The program, described in detail in the First Annual Status Report (NASA CR-174700), was designed to accommodate structures with very general geometry and loading. Further, it was clear that additional capabilities would be developed for BEST3D over a period of several years. For this reason the program was designed so that the anticipated capabilities could be incorporated within the original framework and data structure of BEST3D, without requiring major re-coding of already existing capabilities.

During Task IIC, a number of new and enhanced capabilities were developed and installed in BEST3D. The basic structure of the program remains, however, very similar to that of the original version. The major changes and additions made to the code during Task IIC are described in the following sections. A full description of BEST3D may be found in the First Annual Status Report.

Finally, it should be noted that development of BEST3D is carried out at Pratt & Whitney on an IBM 3084, in both batch and interactive modes, and on an HP9000 minicomputer at SUNY-B. The program is installed on the CRAY computer at NASA-Lewis Research Center. It can therefore be anticipated that BEST3D can be installed, with relatively little difficulty, on most commonly available computer systems.

#### 3.4.4.2 Global Program Structure

The major changes in the overall structure of BEST3D are:

- (1) The incorporation of a branch for the time embedded transient solution.
- (2) Deletion of the complex variable option for transient analysis. The capability for complex variable analysis of forced response at a given frequency has been retained.
- (3) A branch has been designed for natural frequency/mode shape calculations, and will be incorporated as part of Task IVC.

The overall structure of BEST3D at the end of Task IIC is shown in Figure 3.4-2. The program consists of a common input section, followed by three branches, for static, forced response and transient analysis. The static analysis branch is the model for the entire code, since the other branches largely employ generalized forms of the same algorithms used in the static analysis. The branch designed for natural frequency/mode shape calculation is actually part of the static analysis loop.

The transient and natural frequency/mode shape branches will be discussed separately. Other modifications, not visible at the level of the overall program structure (particularly in the plasticity analysis), will also be described.

#### 3.4.4.3 Program Input

The input to BEST3D is essentially unchanged. The discussion contained in the First Annual Status Report (NASA CR-174700) remains accurate. In particular, the library of surface elements has not been changed during Task IIC. The input changes made during Task IIC include:

- (1) Very minor changes to provide the time step definition required for the time embedded transient analysis.
- (2) Simplification of the input used to describe nonlinear material models.
- (3) Inclusion of flags and (when required) additional input for embedded discontinuities, hot spots and rectilinear volume cells.

Program input is fully described in the BEST3D Users' Manual.

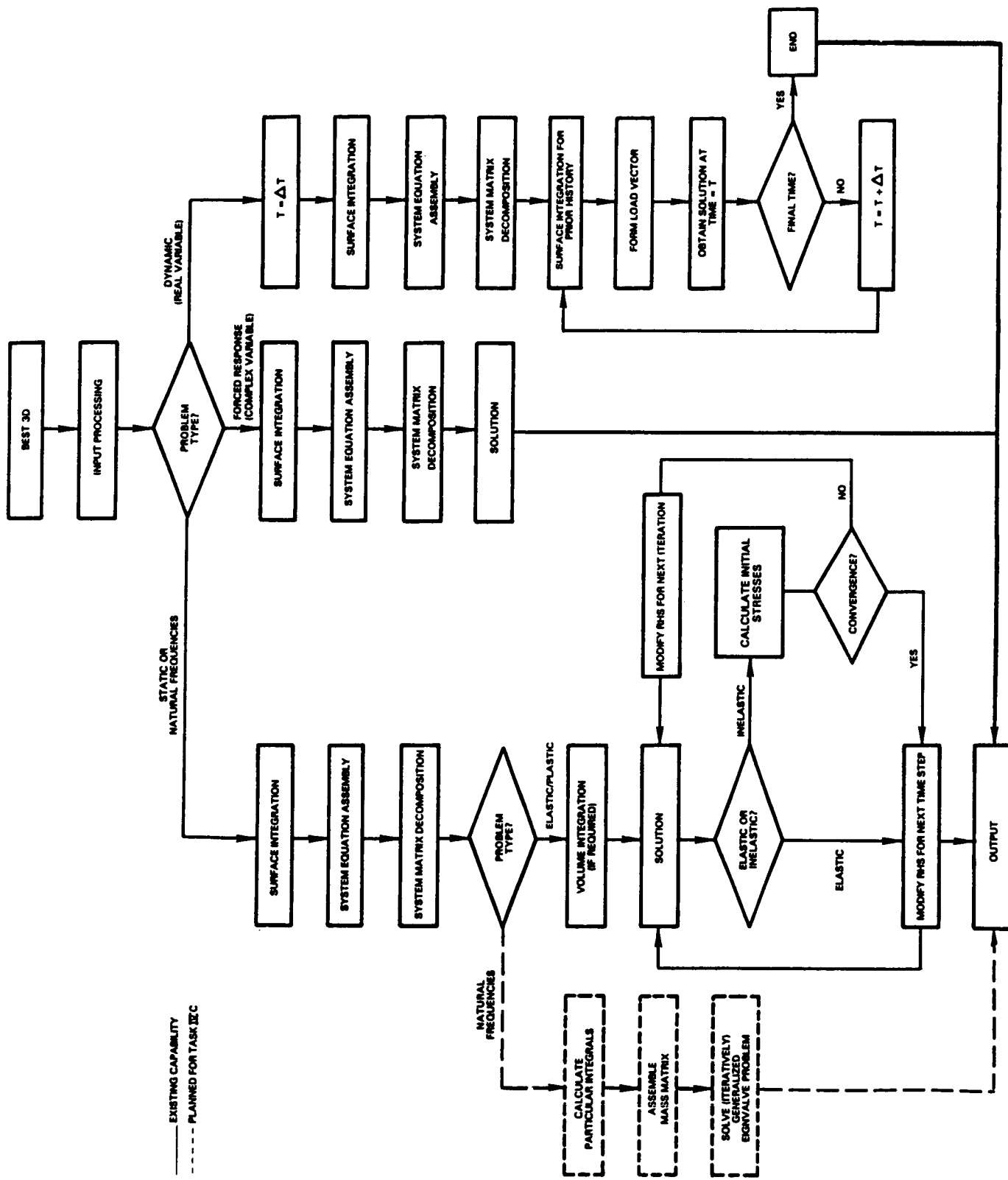


Figure 3.4-2 BEST3D - Overall Program Structure

#### 3.4.4.4 Surface Integral Calculation

The most time consuming portion of an elastic or elastodynamic analysis is the numerical evaluation of surface integrals. BEST3D uses product Gaussian quadrature rules to calculate these integrals. Considerable improvement has been made during Task IIC in the efficiency and accuracy of these calculations. In addition, a fundamental difference between surface integration in the static and in the transient analyses has been clarified.

##### 3.4.4.4.1 Integration in the Static Case

In the original version of BEST3D, 4 x 4 product Gauss rules were used for all of the nonsingular surface integral calculations. Error estimates based on the one-dimensional estimates of Stroud and Secrest (Reference 11) were used to estimate truncation error in the integration. In the event that the requested error tolerance could not be met over the full element, a weighted rectangular subdivision of the element was used. During Task IIC, two things became clear:

- (1) A very large proportion of the time spent in numerical surface integration was used in 'near singular' integrations, that is, cases in which the source point was very close to, but not on, the element being integrated.
- (2) The (analytically derived) error estimates could sometimes be anti-conservative for low integration orders. They also tended to underestimate the benefit of increased integration order.

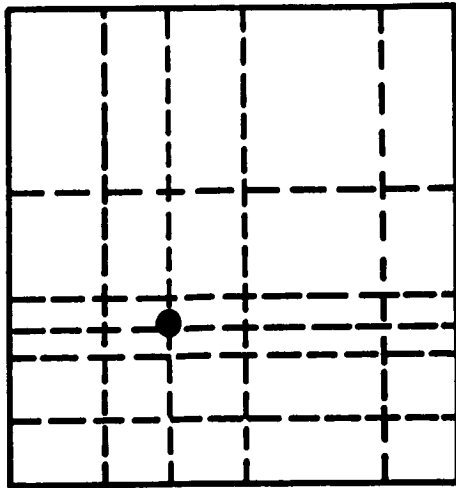
Based on these observations, studies were begun to improve the error estimates for the Gaussian quadrature. The objectives were first to develop more uniformly accurate error estimates and then to employ these new estimates to reduce the computational effort required to carry out the numerical surface integration.

The new error estimates were developed by:

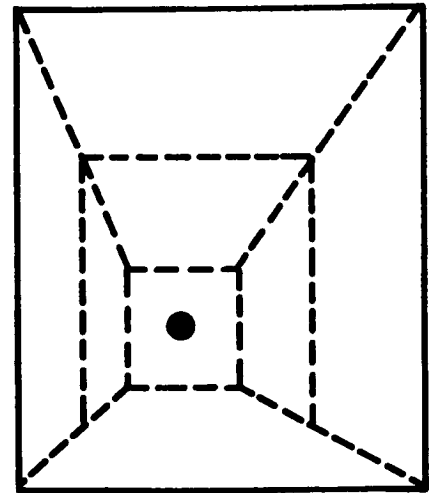
- (1) Noting that the error in the two-dimensional integration can be expressed in terms of appropriate one-dimensional error estimates.
- (2) Carrying out the integration of traction kernel-shape function products over a variety of randomly oriented source point-line segment pairs.
- (3) Fitting the results of these numerical experiments to a functional form based on the analytical error estimates and using statistical techniques to adjust the error equation so that the probability of exceeding the input error tolerance is less than 0.001.

Comparison of the new and old error estimates led to several interesting conclusions:

- (1) Higher order Gauss rules were found to be considerably more effective than previously thought. As a result, the library of integration rules in BEST3D was expanded to include orders two through thirteen, inclusive. This allows many more source point-element pairs to be integrated without subdivision.
- (2) The ability to estimate error more accurately has allowed creation of a more effective algorithm for element subdivision. The original subdivision algorithm always performed a rectangular subdivision, using a 4 x 4 Gauss rule on each subelement. The new algorithm, in the most general case, uses a single central subelement surrounded by rings, each containing at most four subelements (Figure 3.4-3). The order of integration on each subelement, in each direction, is independently set to meet the requested tolerance.



ORIGINAL ALGORITHM



REVISED ALGORITHM

Figure 3.4-3 Subdivision Strategy for Nonsingular Surface Integration

The incorporation of the revised error estimate and subdivision algorithm in BEST3D has led to a reduction in computing time averaging 35 percent for elastic analyses, relative to the original version of the code. In addition, solution accuracy is now much more closely related to the input error tolerance.

#### 3.4.4.4.2 Surface Integration in the Transient Algorithm

The development of the embedded time algorithm for transient elastic analysis during Task IIC has led to a greatly improved understanding of fundamental numerical differences between the static and dynamic cases. In the static case it was found that improvement in integration accuracy and efficiency could be obtained by incorporating higher order Gaussian quadrature rules in BEST3D. It was originally anticipated that a similar improvement would result from incorporating higher order rules in the transient branch of the code. It was found, however, that the introduction of the higher order rules led to greatly increased run times with little improvement in accuracy.

Further study clarified the fundamental difference involved. In the static case the integrands in all of the nonsingular surface integrals are infinitely differentiable and solution accuracy can, therefore, always be improved by the use of increased integration order. In the time embedded case, however, the point load solutions are only continuous. Physically this corresponds to the fact that the disturbance due to an impulse applied to a given time and spatial location is nonzero, at some later time, in only a finite portion of space. This means that the kernel function may be nonzero over only part of a given surface element. While the integrand is infinitely differentiable within both the zero and nonzero regions considered separately, its overall continuity over the entire element is only  $C^0$ . The use of higher order quadrature rules is, therefore, of little use in improving accuracy.

Based on these observations, a revised integration strategy was adopted for the transient branch of BEST3D. The surface elements are subdivided into a relatively large number of subelements, and relatively low (usually 2nd or 3rd) order quadrature rules are used over each subelement. This has led to much improved accuracy in the transient analysis.

#### 3.4.4.5 Volume Integrals

No additional changes were introduced to the volume integration scheme described in First Annual Status Report (NASA CR-174700).

#### 3.4.4.6 System Matrix Assembly for Multiregion Plasticity

For the single region inelastic problem the system equation can be expressed as:

$$\begin{array}{c} Ax = b \\ \sim \quad \sim \end{array}$$

where  $b$  contains the total effects of the boundary loading as well as the non-linearity. Since this final system matrix is algebraically identical to that for a single region elastic problem, the multi-GMR (generic modeling region) plasticity problem can use the same code for the assembly of the multi-GMR system equations.

#### 3.4.4.7 System Equation Solution

The solution of the system equations is essentially unchanged from the initial version of BEST3D. The only major change was provision of a capability for more efficient solution process for problems involving multiple loads. This was primarily required for efficiency in inelastic analyses.

#### 3.4.4.8 Inelastic Solution Process for a Multi-GMR (Generic Modeling Region) Problem

The inelastic solution algorithm has been developed in such a manner that the existing coding for the multiregion elastic problems is utilized without modification. This essentially requires that the system matrix  $A$  and the right-hand side  $b$  be individually formed for each GMR and supplied to the solver for assembly and solution. The process of determining  $b$  of course requires the initial volume integration of a number of algebraically complex kernels as well as the definition of the inelastic states via the various constitutive models. This requires multiple solutions of the same system equations to satisfy the state dependent constitutive equations at all boundary and interior nodal points of cells.

#### 3.4.5 Validation/Verification

##### 3.4.5.1 Summary

During Task IIC, significant new capabilities were added to BEST3D. The validation and evaluation of these new capabilities and the continuing verification of BEST3D is discussed in the subsections which follow. Attention in this report is directed particularly to the validation and verification of the non-linear analysis capability and to the evaluation of the time embedded dynamic formulation.

A very large set of test cases was constructed during Task IC to validate BEST3D's ability to represent properly complex geometries and boundary conditions and to carry out accurately elastic stress analysis. Many of these test cases were executed again during Task IIC in order to verify the continuing correct operation of already existing capabilities. These test cases were discussed in the First Annual Status Report (NASA CR-174700), and are not discussed further in this report unless they have been modified to demonstrate a newly implemented capability.

### 3.4.5.2 Validation of Elastic Capabilities

Two major modifications were made to the elastic capabilities of BEST3D during Task IIC. First, the closed form point load solution for a transversely isotropic material was recast in a computationally efficient form and coded. Additionally, the required modifications to allow calculation of elastic stresses and strains at boundary nodes and to account for centrifugally loaded anisotropic materials were carried out. Second, a new error estimate for non-singular surface integration and a more efficient subdivision algorithm based on this estimate were coded and incorporated in BEST3D. The validation of these capabilities is discussed below.

#### Transversely Isotropic Cube in Tension

A unit cube was modeled using six linear surface elements, one for each face of the cube. The beam was loaded along the x-axis, parallel to one of the secondary material axes. The axis of isotropy was aligned with the z-axis. The displacements and stresses from the BEST3D analysis are compared to the exact solution in the table below.

	BEST3D	Exact
$U_x$ - elongation	.0010003 in.	.0010003 in.
$U_y$ - Poisson contraction	-.00014321	-.00014318
$U_z$ - Poisson contraction	-.0050946	-.00050942
$\sigma_x$	21201 psi	21200 psi
All other stresses	0	<1

It is clear that the boundary element method (BEM) results are essentially exact, validating the correct operation of the anisotropic capability. The analysis time for the transversely isotropic case is approximately 22 percent higher than that for the isotropic case. This is due to the fact that the transversely isotropic point load solution is computationally much more complex than the isotropic solution.

The same geometry was also analyzed using two GMRs (generic modeling regions) in order to demonstrate the correct operation of the multi-GMR capability for anisotropic materials.

#### Validation of Surface Integration Algorithm

The new surface integration algorithm was evaluated using the slab shown in Figure 3.4-4. Six boundary elements were used to model the slab. Although geometrically simple, the problem fully exercises the integration algorithm because of the large variation in the ratio of element size to the source point - element distance.

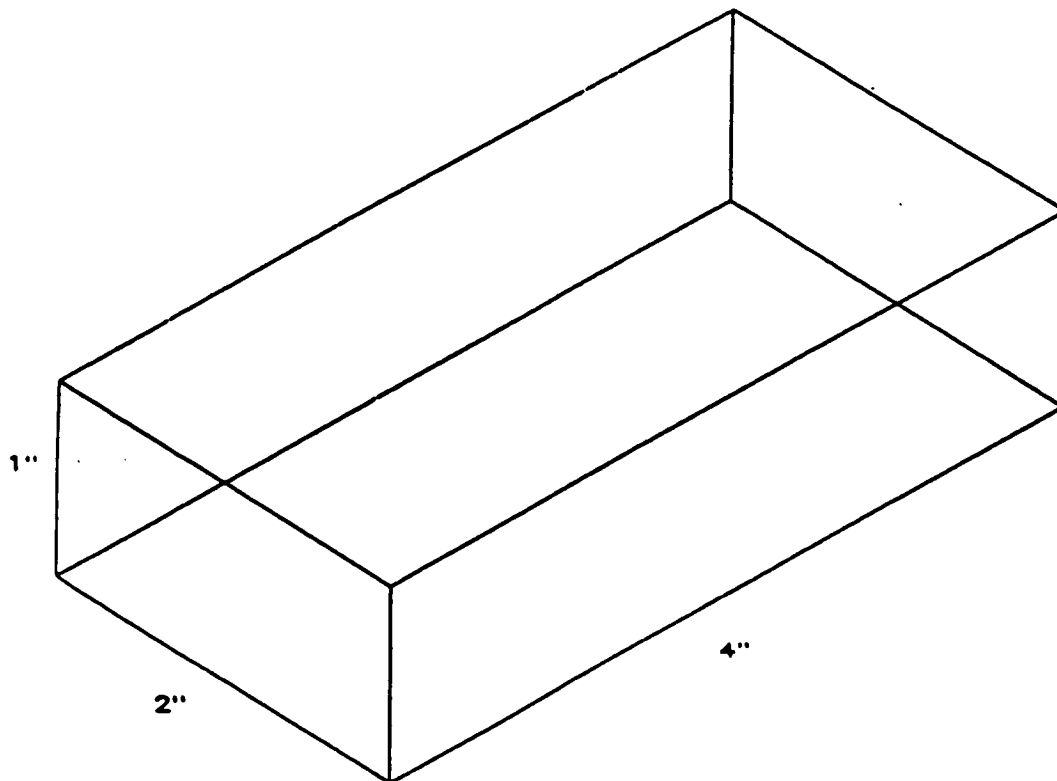


Figure 3.4-4 Test Geometry for Surface Integration Algorithm

The variation of solution error (measured in terms of the reactions at the restrained end of the slab) with the allowable relative error in the numerical integration is shown in Figure 3.4-5. It is clear that the solution error is very directly related to the integration tolerance specified, which was not the case with the estimates used in the original version of BEST3D. As shown in Figure 3.4-6, it is also clear that the computational effort required to achieve a given level of solution accuracy grows very rapidly if very small tolerances are imposed. For this reason a default tolerance was set which attempts to optimize the relationship between accuracy and cost.

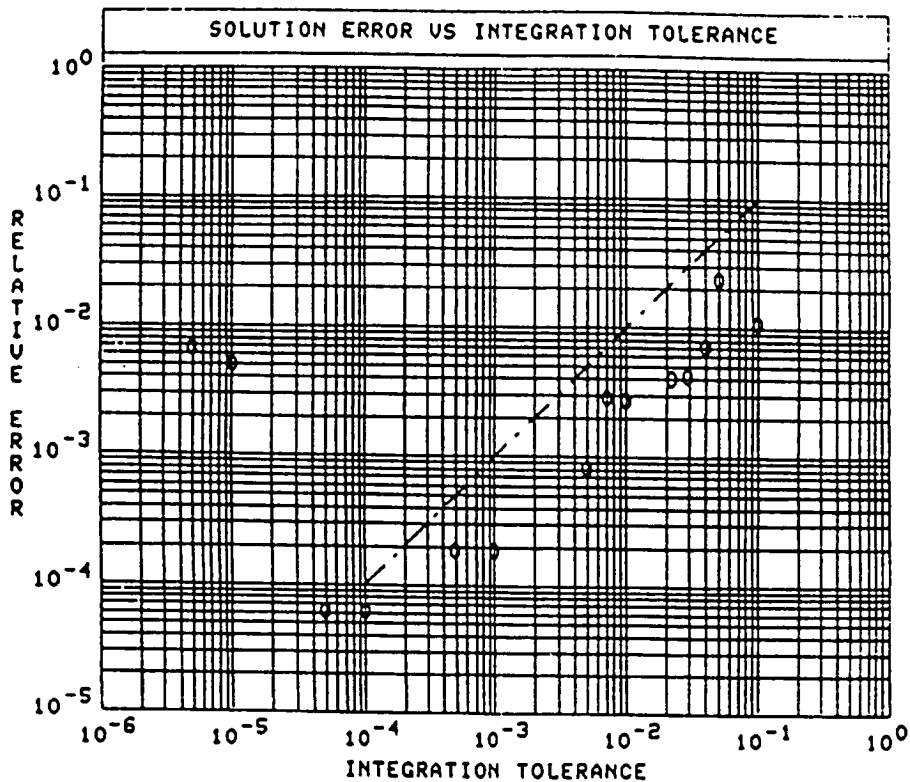


Figure 3.4-5 Solution Error Vs. Integration Tolerance

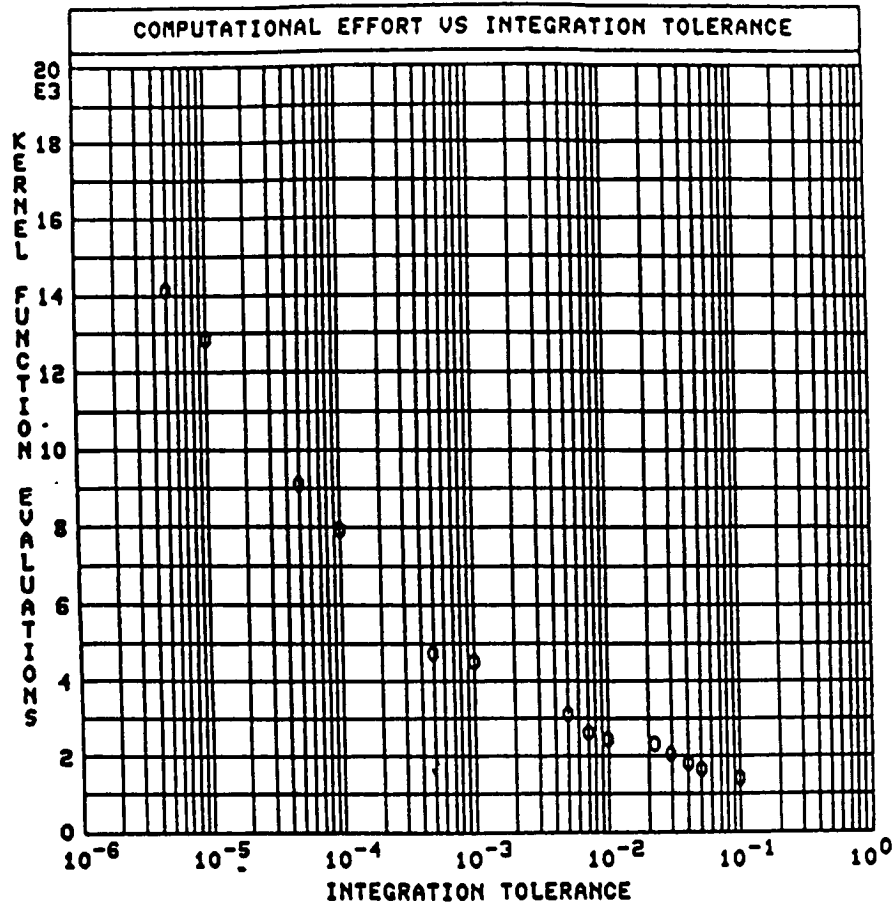


Figure 3.4-6 Computational Effort Vs. Integration Tolerance

### 3.4.5.3 Multi-region Nonlinear Analysis

The multi-GMR nonlinear capability of BEST3D has been evaluated using an extensive set of analyses of pressurized thick shells and disks. The results of these very demanding analyses, involving large-scale plasticity, were used both to validate the multi-GMR plasticity capability and to develop an understanding of proper volume cell definition. The problems were run using an elastic-perfectly plastic material model and plane strain boundary conditions in order to allow comparison to an analytical solution.

## Thick Cylinder

The first problem discussed is that of a thick cylinder (outer radius/inner radius = 2) subject to steadily increasing internal pressure. A  $22.5^\circ$  sector of the cylinder was modeled (Figure 3.4-7). Two boundary and volume discretizations, employing quadratic variation, were used. For both meshes the analysis was carried to collapse, that is, to the load at which BEST3D could no longer converge to a solution.

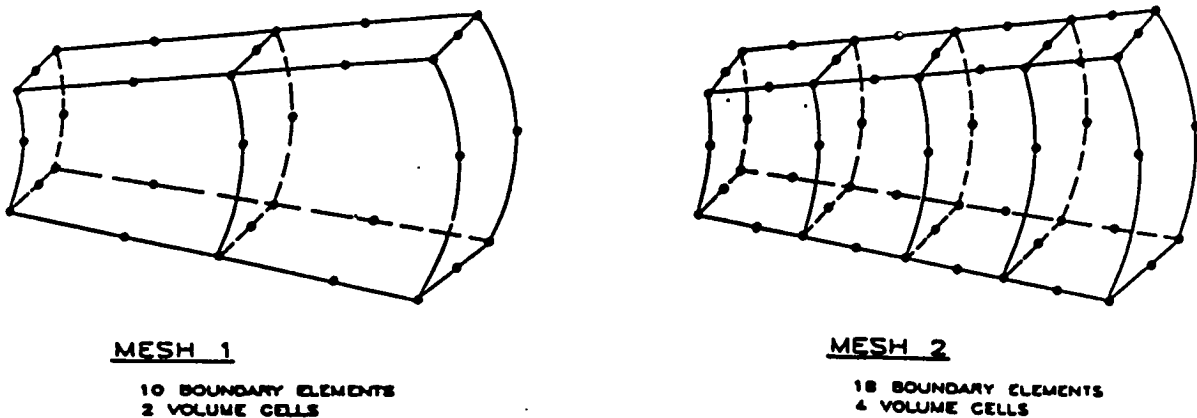


Figure 3.4-7 BEST3D Models for Thick Cylinder

The normalized load - deflection response of the cylinder is shown in Figure 3.4-8. Even Mesh 1, with only two volume cells gives a good representation of the solution, while Mesh 2 converges and gives an accurate displacement value up to 92 percent of the theoretical collapse load. The BEST3D results for the stress variation in the cylinder are also very accurate, as shown in Figure 3.4-9.

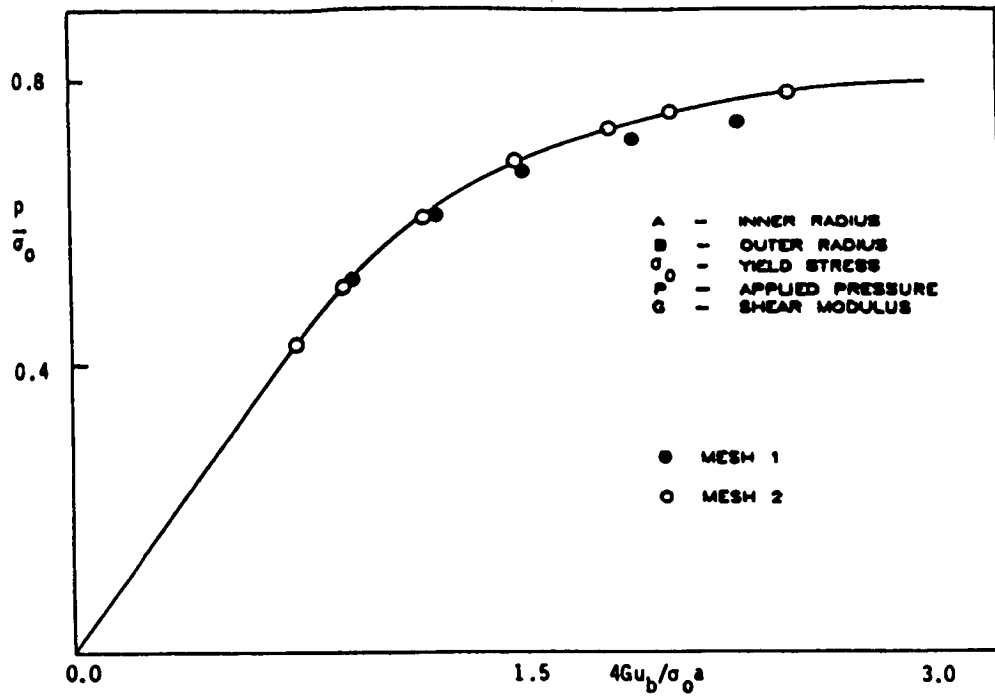


Figure 3.4-8 Normalized Radial Expansion at Outer Radius of Cylinder

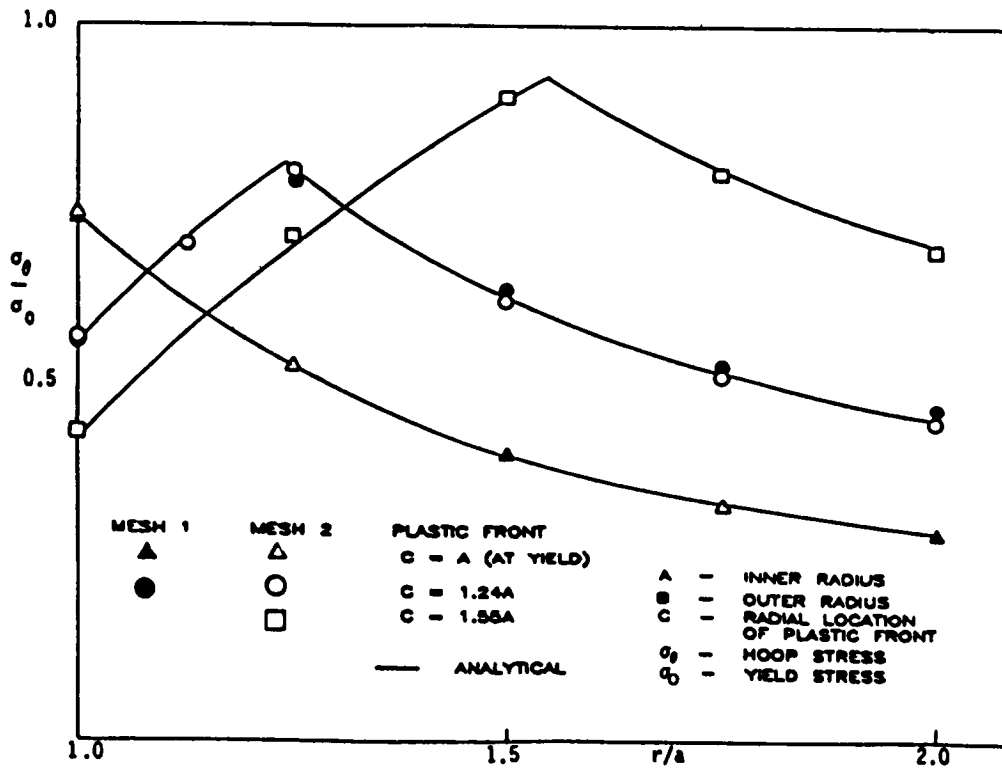


Figure 3.4-9 Radial Variation of Hoop Stress in Thick Cylinder

The BEST3D analyses for this problem were carried out using both one and two region models (with the interface located at a radius of 1.5a). The results were identical. It should also be noted that, in these analyses, the boundary elements and volume cells were equally spaced in the radial direction. Experience in other problems indicates that convergence even closer to the theoretical collapse load can be achieved by weighting the volume cells towards the inner radius of the cylinder.

### Disk

The second problem is that of a disk (outer radius/inner radius = 5) subject to pressure at the inner radius. This geometry is typical of that encountered in high-pressure turbine disks. Experience with the cylinder analyses, discussed above, indicated that at least four volume cells would be required for this analysis. It was also expected that an appropriate weighting of the cell discretization would prove desirable. The three meshes used (Figure 3.4-10) all consist of twenty quadratic boundary elements (including the interface elements) and four volume cells.

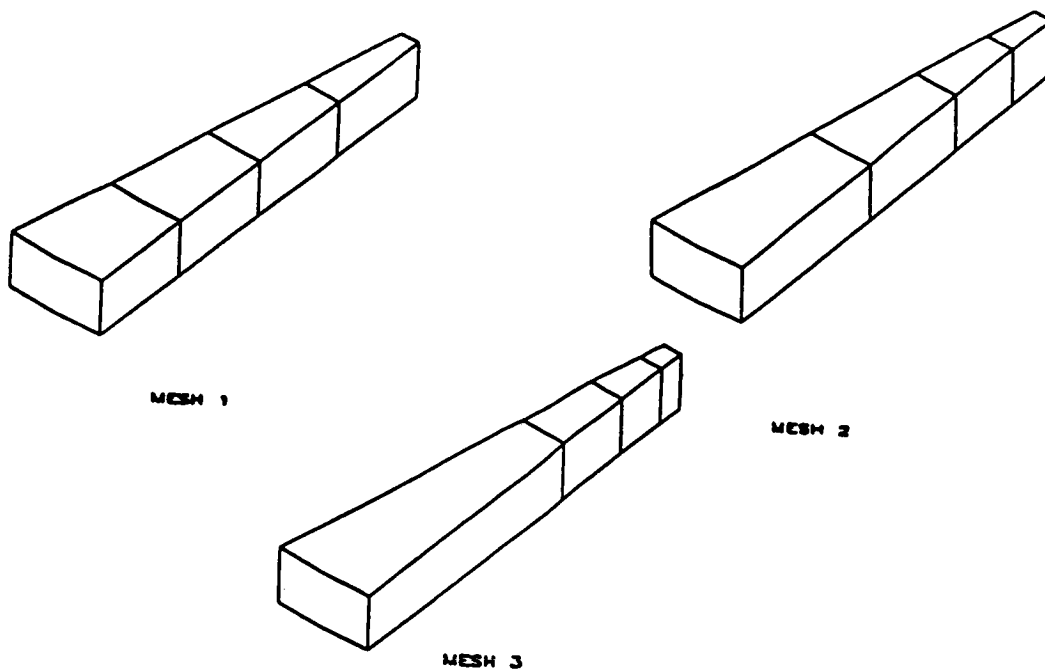


Figure 3.4-10 BEST3D Models for Inelastic Analysis of Disk

As anticipated, the weighting of the volume cells toward the inner radius leads to increasingly good agreement of the BEST3D results with the analytical solution (Figure 3.4-11). It is clear that more volume cells would be required to carry the analysis to collapse. In practice this would not be needed, since plastic deformation is normally limited to the inner 20 percent to 30 percent of a disk.

It is clear (Figure 3.4-12) that all three meshes provide an accurate elastic solution. It is, therefore, of considerable interest to study the optimization of the volume discretization for a fixed boundary model. This study is now being conducted.

The analysis of the disk was repeated using a single region with cyclic boundary conditions. The results were unchanged from those discussed above.

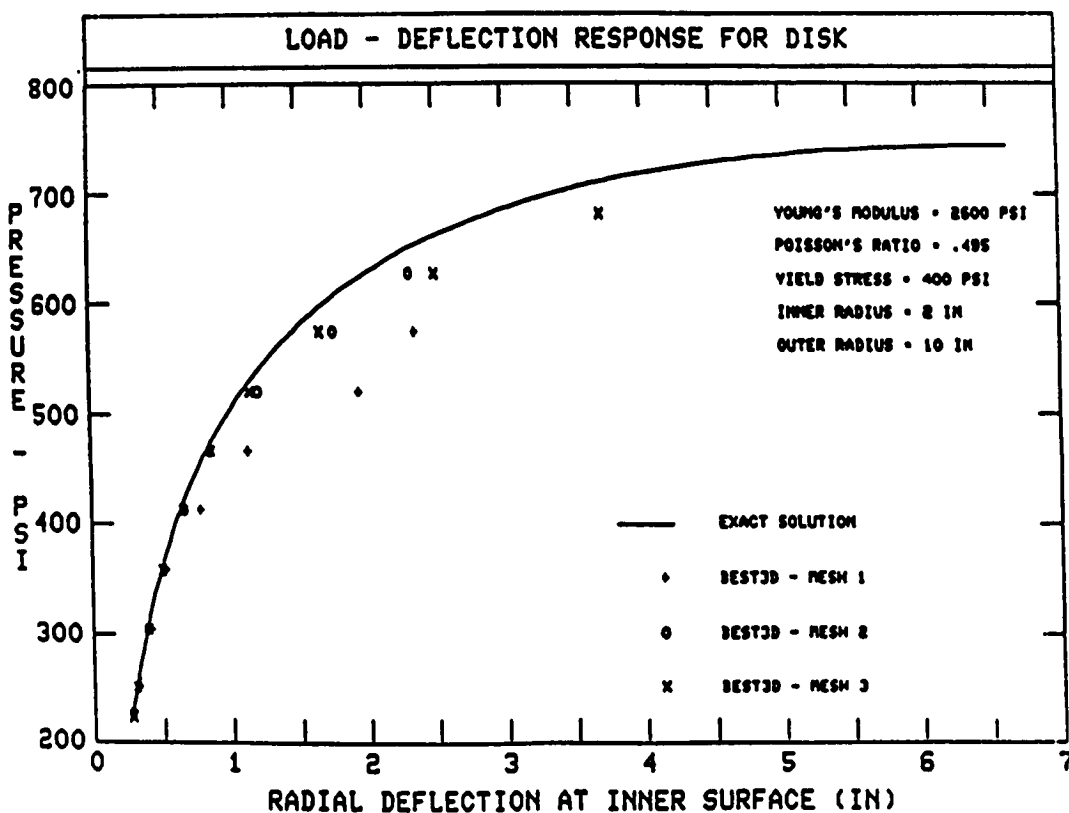


Figure 3.4-11 Load - Deflection Response for Disk

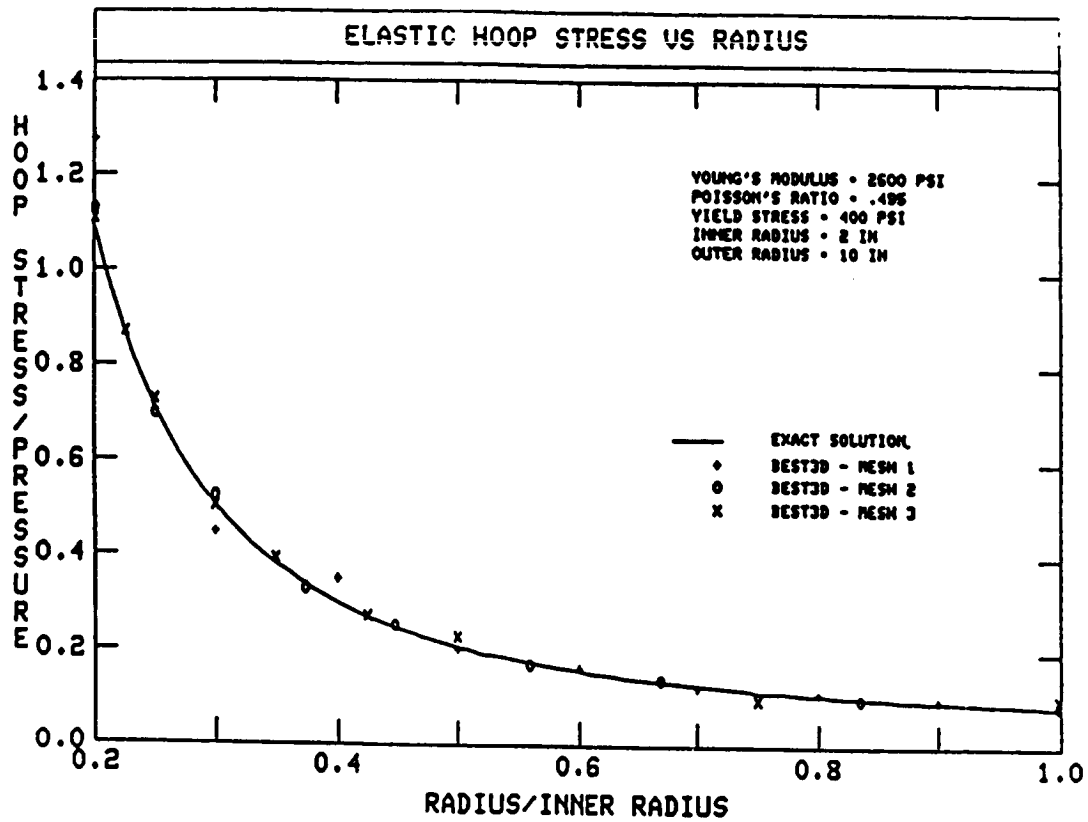


Figure 3.4-12 Elastic Hoop Stress Vs. Radius

#### 3.4.5.4 Application of Exact Initial Strain Solution

The exact solution for the stress and displacement due to a uniform state of initial strain (or stress) in a rectangular parallelepiped (discussed in Section 3) has been exploited in three different areas. A test case for one of these applications is discussed below.

The capability to include the effects of embedded holes without explicit modeling has been incorporated in BEST3D. Up to ten such discontinuities may be included in each generic modeling region (GMR). In order to evaluate the effectiveness of this technique, for both elastic and plastic analysis, a test problem was defined in which a slot with rounded ends is embedded in a tension strip (Figure 3.4-13). In the BEST3D analysis the slot is represented as a rectilinear cell, without explicit modeling.

The BEST3D elastic results, for the stress variation between the free surface and the slot surface, are compared with a plane strain solution (using modeled slots) in Figure 3.4-14. The stresses show good agreement except near the slot surface, where the actual surface geometry of the slot becomes important.

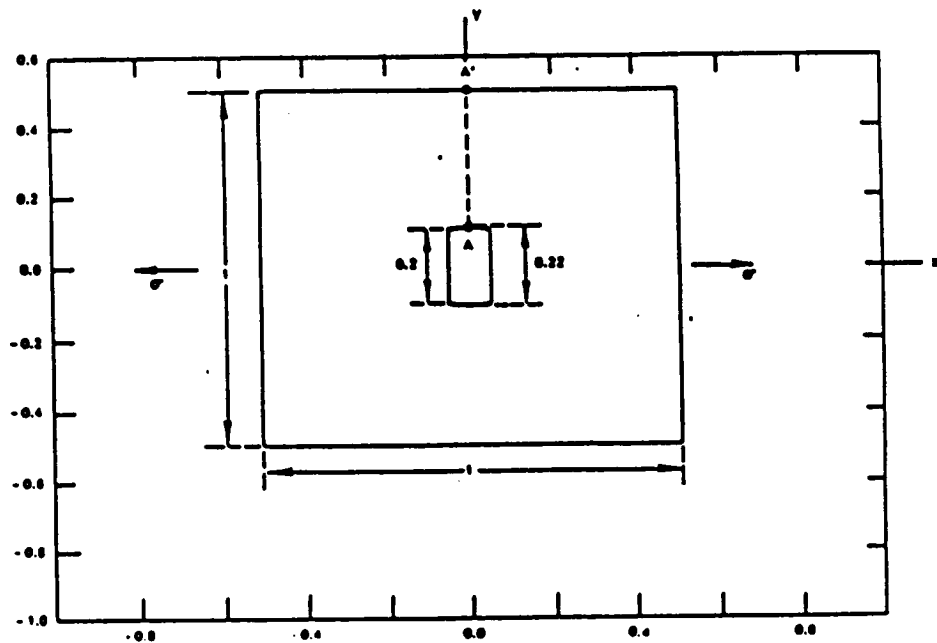


Figure 3.4-13 Constant Thickness Plate With Through Thickness Slot

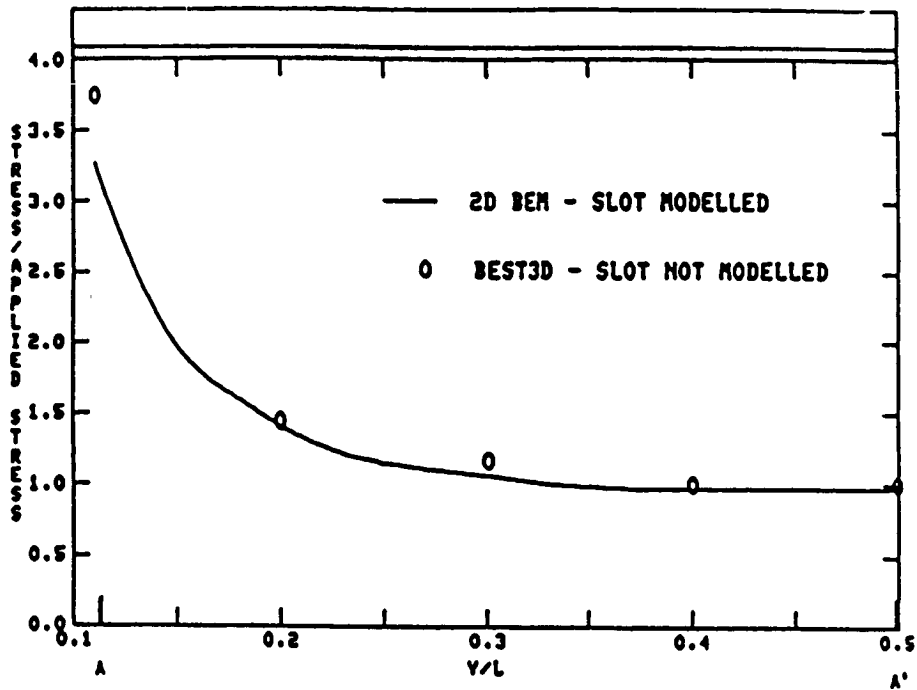


Figure 3.4-14 Stress Variation in Plate With Slot

#### 3.4.5.5 Embedded Time Dynamic Analysis

##### Explosion in a Spherical Cavity

The time embedded transient solution was exhaustively tested using the problem of a spherical cavity in an elastic space, subjected to a suddenly applied pressure load. Three boundary meshes (Figure 3.4-15) were used for the solution of this problem.

This problem was chosen for detailed study because the existence of an exact solution allows precise evaluation of the accuracy of the numerical solution and, in particular, the effects of time step size and boundary mesh refinement. Figure 3.4-16 compares the results of a BEST3D analysis, using Mesh 1 and a time step of 0.00035 second, with the analytical solution. The boundary element method (BEM) results show good qualitative agreement with the exact solution, but underestimate the peak deflection by about 12 percent, due primarily to an overly crude boundary mesh. This is demonstrated in Figure 3.4-17, where the dynamic magnification factors (transient/steady state displacement) for the exact and numerical results are compared and quite good agreement is apparent.

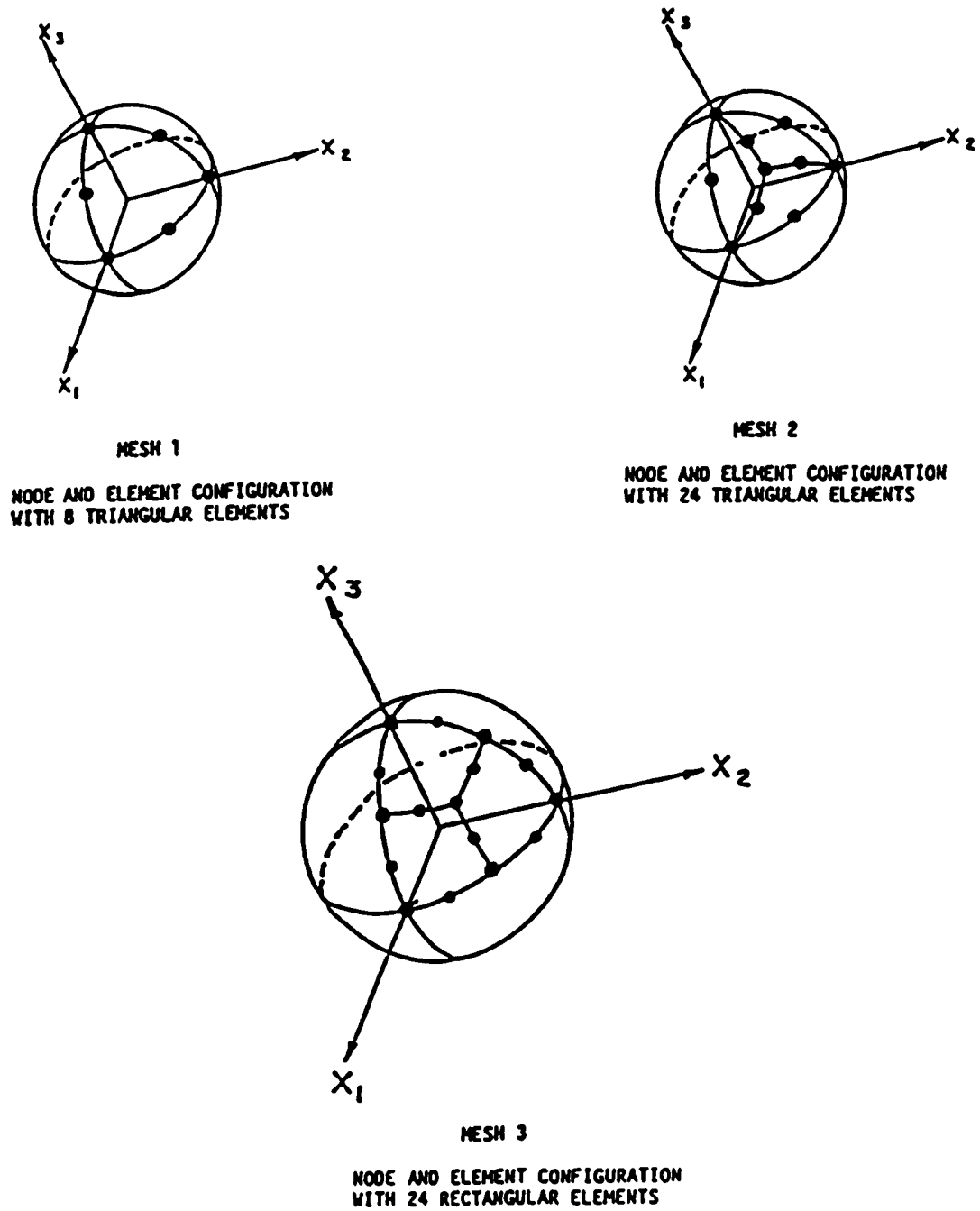


Figure 3.4-15 BEST3D Models for Spherical Cavity

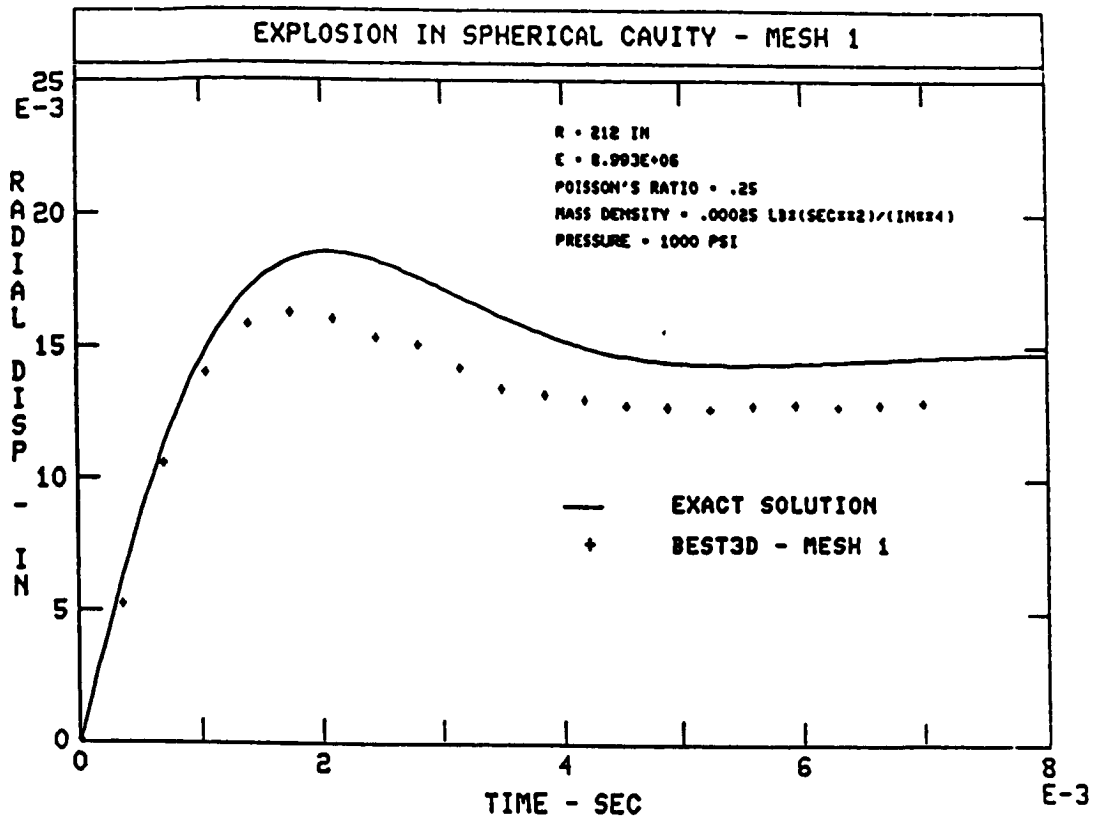


Figure 3.4-16 Explosion in Spherical Cavity - Mesh 1

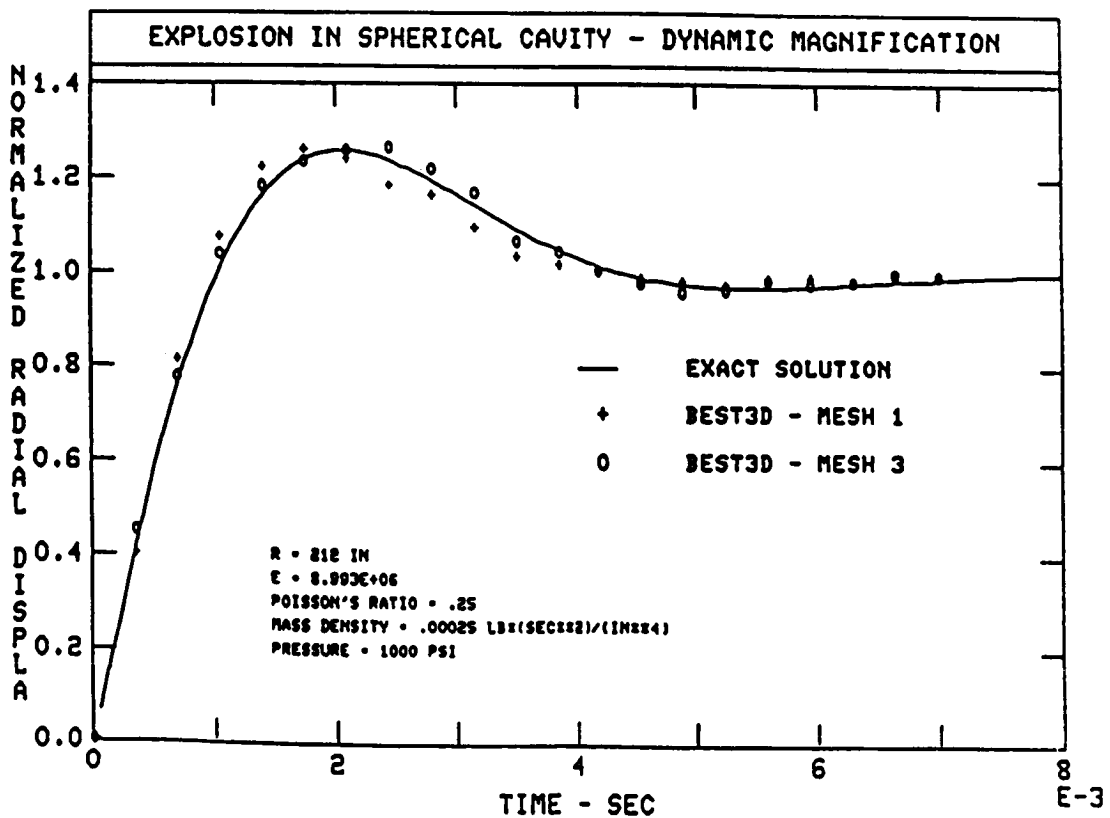


Figure 3.4-17 Explosion in Spherical Cavity - Dynamic Magnification

The question of sensitivity to time step size is always of importance in transient analysis. Mesh 1 was also used to examine this question by calculating the solution for a variety of step sizes (0.0002 second to 0.0007 second). The results show almost no sensitivity to step size.

Based on the experience with Mesh 1, it was concluded that a more refined surface mesh, capable of giving a more accurate result for the static problem, would also be suitable for the transient analysis. Mesh 2 and Mesh 3 were used to confirm this, although only the results for Mesh 3 are presented in the report. The dynamic magnification factors obtained with Mesh 3 are slightly improved relative to Mesh 1. The absolute displacement - time response, however, is dramatically improved (Figure 3.4-18).

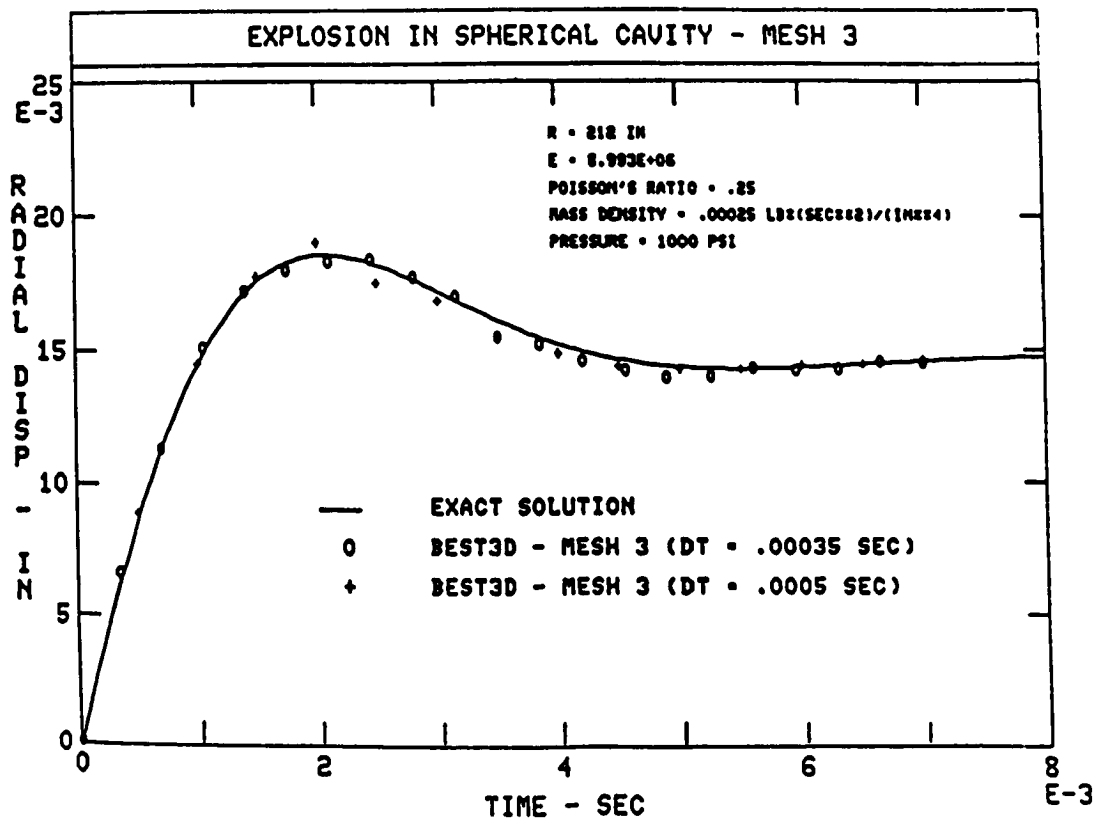


Figure 3.4-18 Explosion in Spherical Cavity - Mesh 3

### 3.4.5.6 Calculation of Natural Frequencies and Mode Shapes

A number of two-dimensional test problems were solved in order to validate the algorithm designed for natural frequency and mode shape calculations in BEST3D. One of these problems, which was also solved using the MHOST finite element code, is described below.

The first four bending modes for a cantilever beam were calculated using both a two-dimensional BEM code and the MHOST finite element code. The beam has a length of 6.5 units and a square (1x1) cross section. The meshes used for the two analyses were very similar, with fourteen nodes along the beam length for the finite element model and thirteen for the BEM model. The calculated eigenvalues agree well.

Natural Frequencies (Hz) of Cantilever

Mode	2-D BEM	MHOST
1st bending	0.368	0.378
2nd bending	2.214	2.188
3rd bending	5.591	5.583
4th bending	9.986	9.908

Further, the mode shapes calculated using the two techniques are indistinguishable. The first and fourth modes are shown in Figure 3.4-19. It should be noted that the fourth mode displays a nonzero slope at the fixed end. This is a real feature of the two-dimensional solution which is not present in a beam theory analysis, since it is suppressed by the fixed end boundary conditions normally used in beam theory.

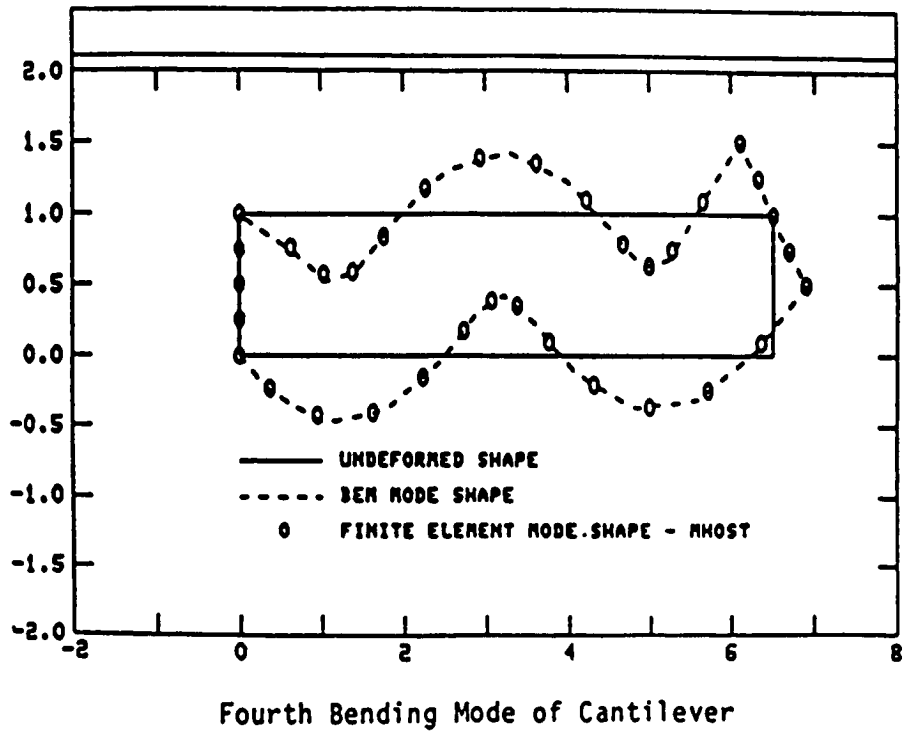
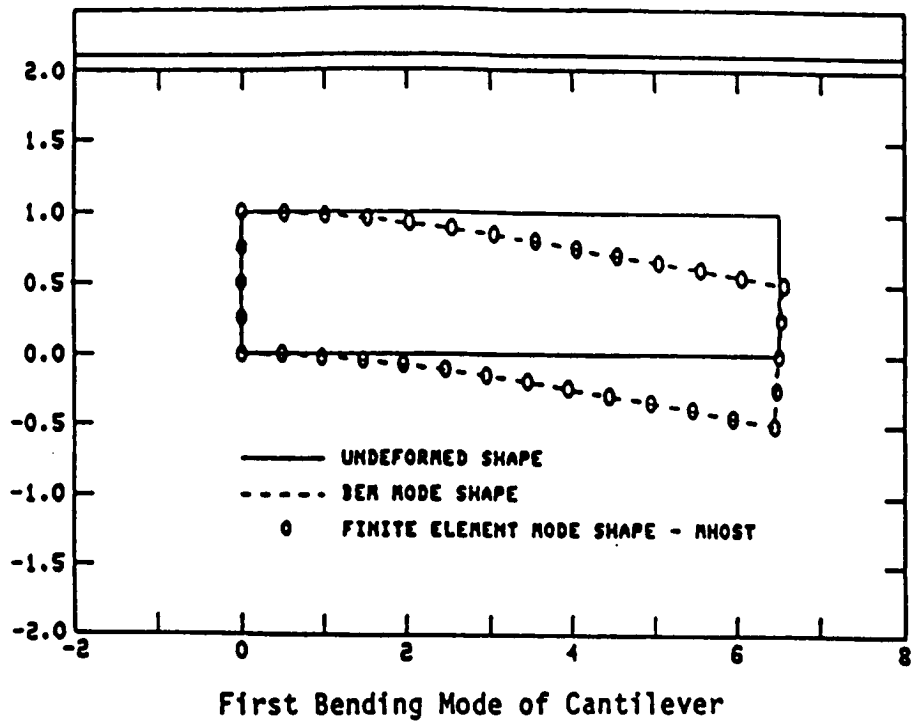


Figure 3.4-19 Comparison of Finite Element and Boundary Element Mode Shapes

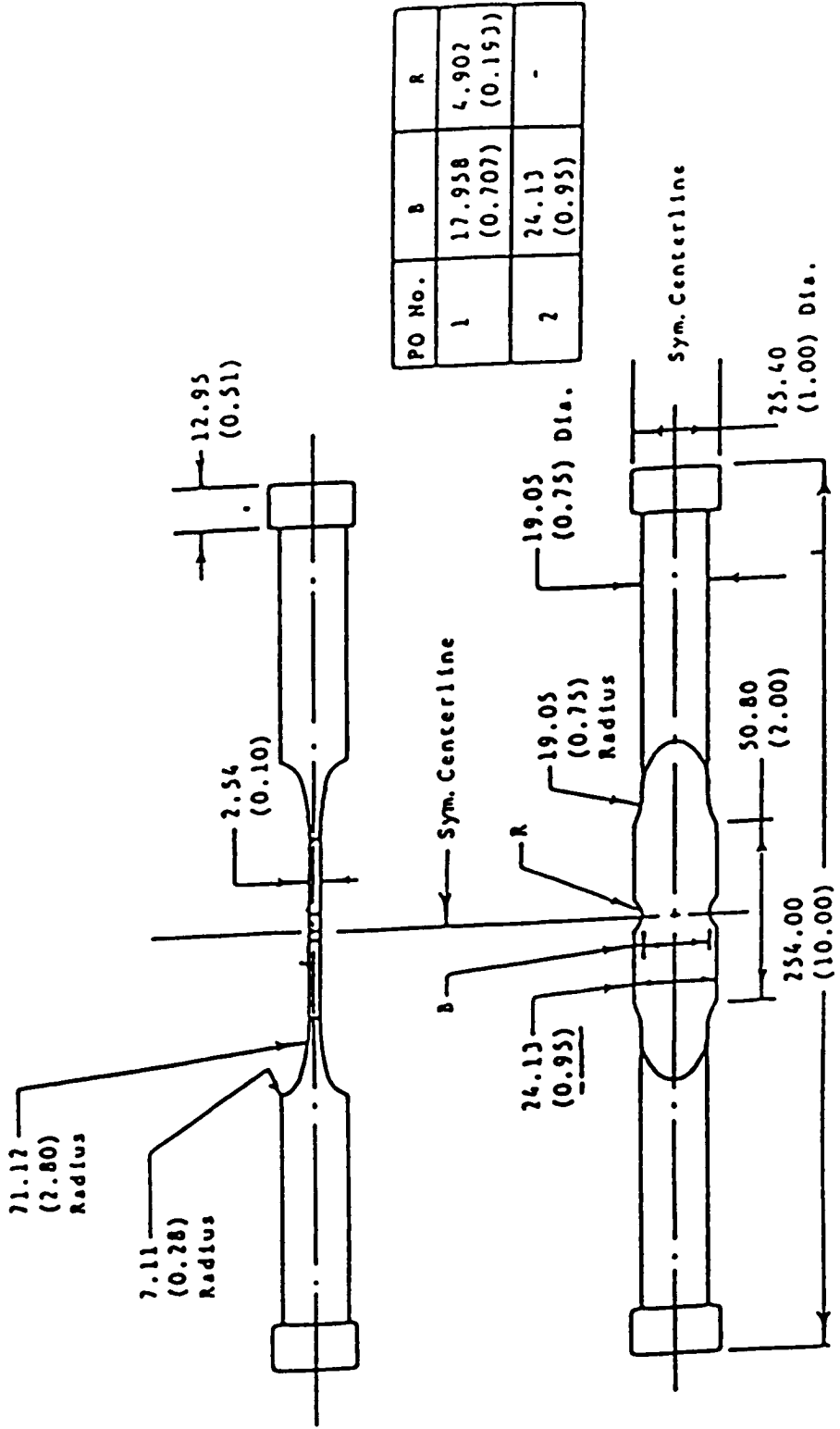
#### 3.4.5.7 Inelastic Analysis of the Benchmark Notch Specimen

The Benchmark Notch Specimen is a double edge notch specimen developed by General Electric/Louisiana State University (GE/LSU) under NASA-Lewis Contract NAS3-22522. A significant volume of well documented data was provided as part of the contract report (Reference 12). These data were used during Task IC to verify the elastic capabilities of BEST3D. During Task II, the inelastic data from this program have been used to verify the nonlinear capabilities of both BEST3D and MHOST.

The specimen geometry is defined in Figure 3.4-20. Stress analysis was carried out for the gage section only, a procedure already known to be satisfactory. The specimen models used are shown in Figure 3.4-21 (for BEST3D) and Figure 3.4-22 (for MHOST). In both cases it was found that selective mesh refinement and weighting of elements toward the notch were required in order to obtain acceptable accuracy with reasonable computing times. It should be especially noted that the MHOST models use eight node elements. This means that the MHOST "fine mesh" and "intermediate mesh 2" provide the same through-thickness displacement variation as the quadratic BEST3D elements. This refinement was needed to obtain accurate finite element results.

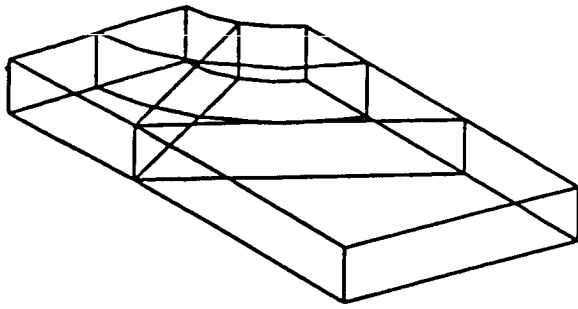
In Figures 3.4-23 and 3.4-24, the calculated strains at the notch root are compared to a regression fit to the GE/LSU data. It is clear that, with an appropriate choice of mesh, both BEST3D and MHOST accurately predict the measured strains.

In addition to the monotonic loading results discussed above, the cyclic plasticity model in BEST3D was used to predict specimen response over a more complex loading sequence (no load --> max load --> min load --> max load). The results of the cyclic calculation for Test 7 are shown in Figure 3.4-25. Again, excellent agreement with the GE/LSU data was obtained.

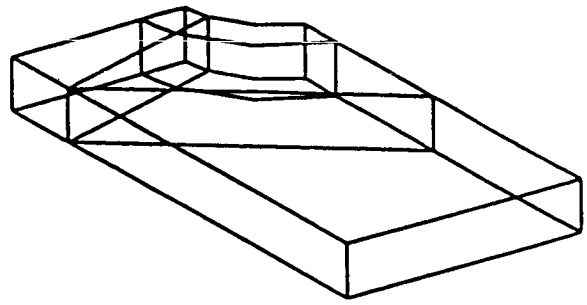


Dimensions in mm (Inches)

Figure 3.4-20 Double Edge Notch Specimen Used In Contract NAS3-22522

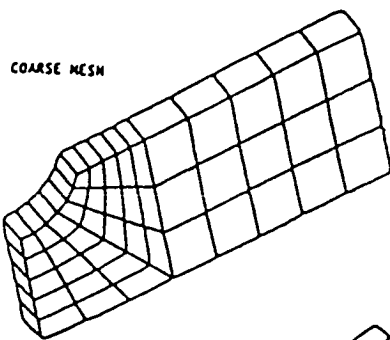


EQUALLY SPACED MESH

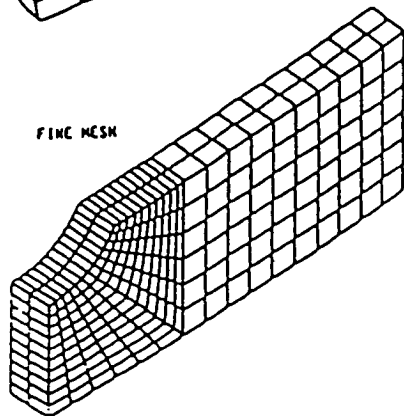


WEIGHTED MESH

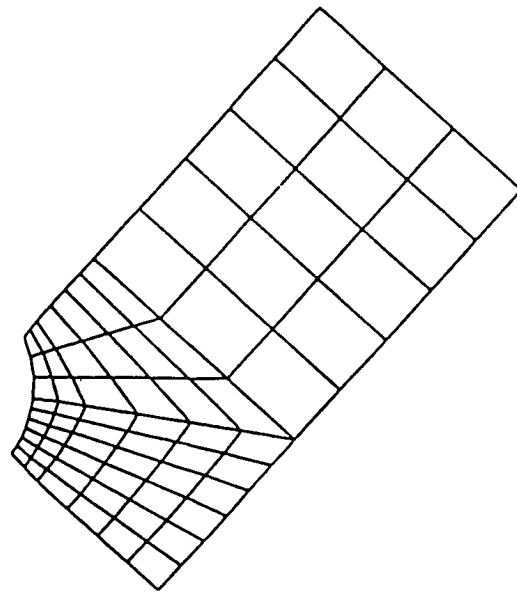
Figure 3.4-21 Boundary Element Models for Benchmark Notch Analysis



COARSE MESH



FINE MESH



INTERMEDIATE MESH

TWO VERSIONS USED:

- 1 - ONE ELEMENT THROUGH THICKNESS
- 2 - TWO ELEMENTS THROUGH THICKNESS

Figure 3.4-22 Finite Element Models for Benchmark Notch Analysis

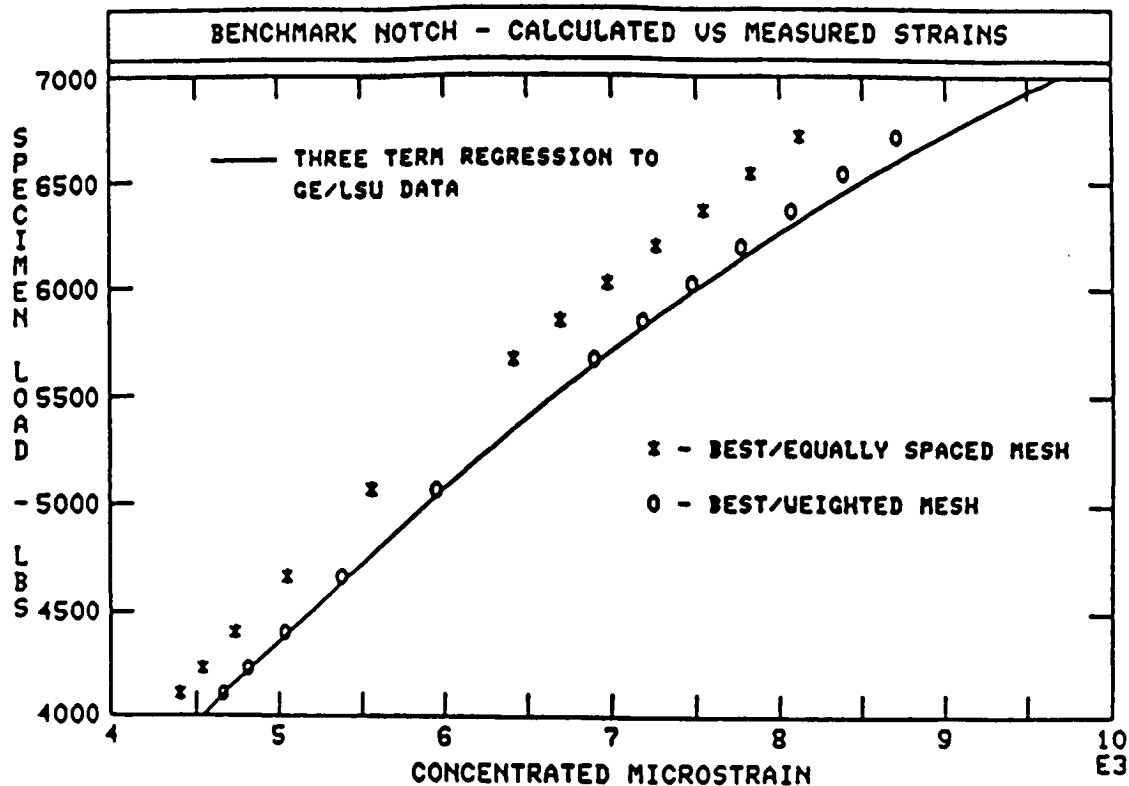


Figure 3.4-23 Benchmark Notch - BEST3D Vs. Measured Strains

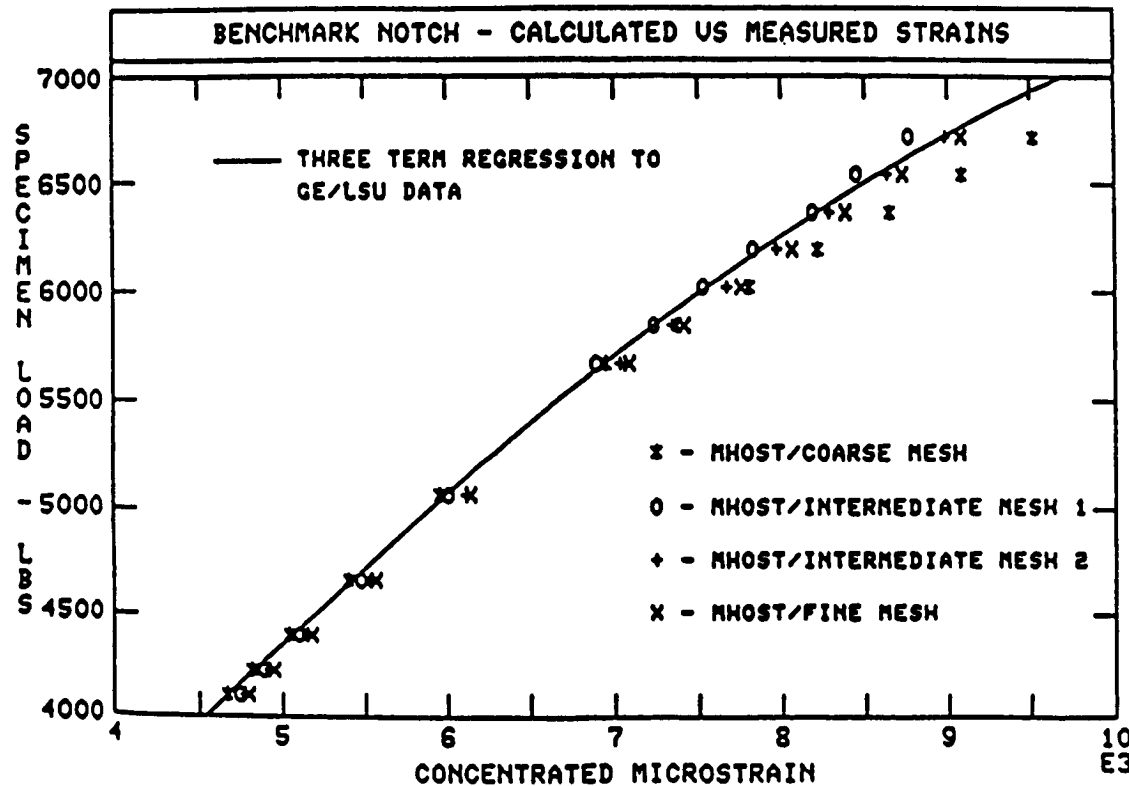


Figure 3.4-24 Benchmark Notch - MHOST Vs. Measured Strains

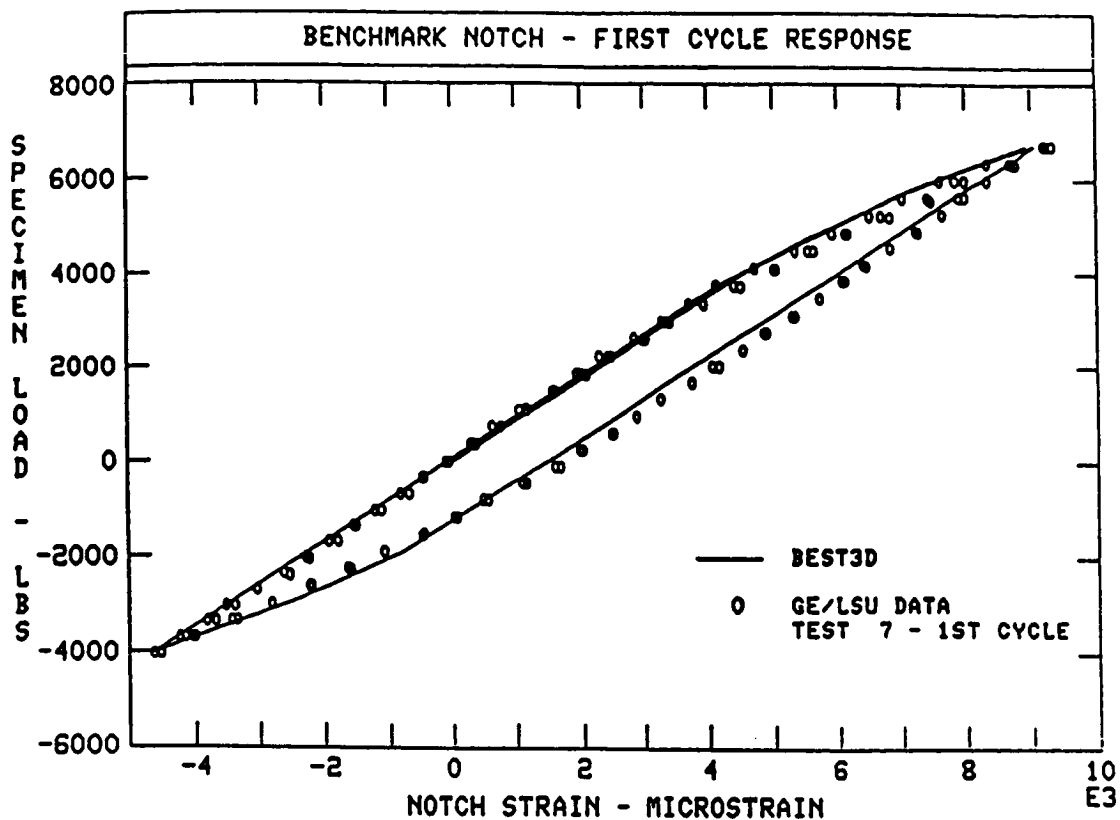


Figure 3.4-25 Benchmark Notch - First Cycle Response

#### 3.4.5.8 Component Analysis

Further elastic analysis has been done for the turbine blade (Figure 3.4-26) originally discussed in the First Annual Status Report (NASA CR-174700). The blade was analyzed under centrifugal load using both BEST3D and MARC (three-dimensional finite element). The evaluation of the results was greatly simplified through the use of an in-house program providing (color) deflected shape and iso-stress plots. It is a relatively straightforward task to link BEST3D to such a tool.

In Task IC the intent of the turbine blade analysis was primarily to verify the correct operation of the code for this highly complex problem. The intent in Task IIC was to verify BEST3D's ability to calculate correctly the peak stress in the blade and determine the degree, if any, of mesh refinement needed for this calculation.

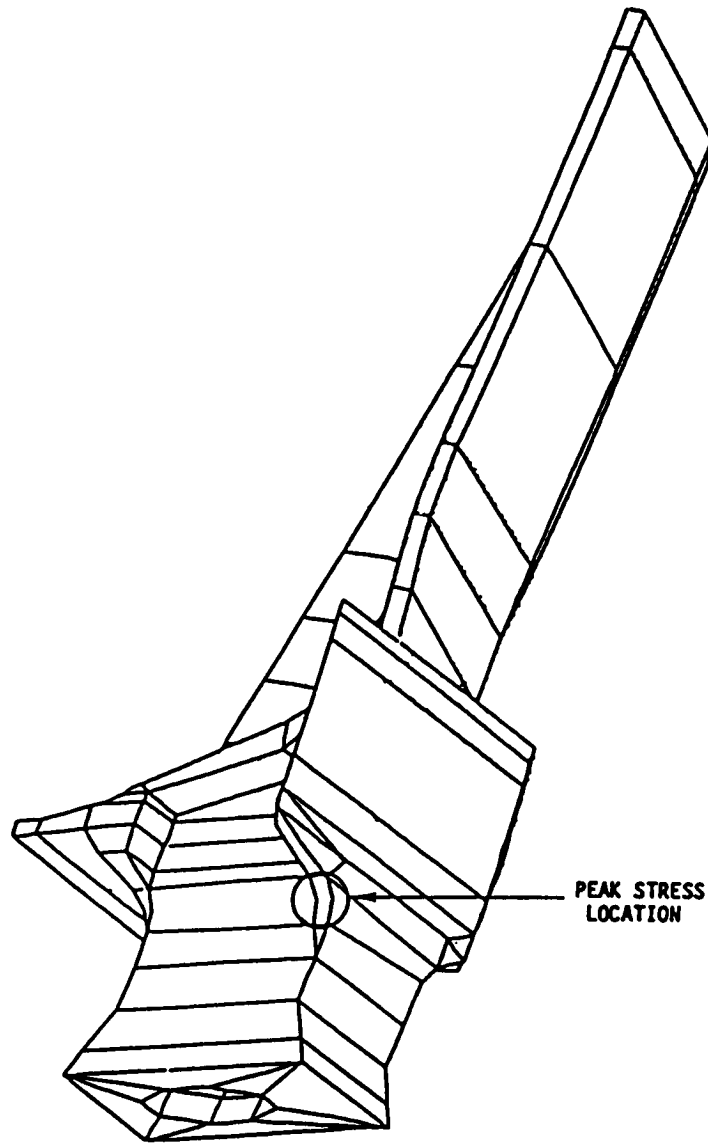


Figure 3.4-26 BEST3D Model of Cooled High-Pressure Turbine Blade

A fully linear BEST3D analysis correctly predicted the peak stress location and gave a peak (maximum principal) stress of 146 ksi, significantly lower than the MARC result of 169 ksi. Experience with other problems indicated that the use of limited quadratic variation near the peak stress location should lead to considerable improvement with a very limited increase in computing cost.

In order to test this supposition, the BEST3D analysis was repeated using eighteen quadratic elements. The extent of quadratic variation is indicated in Figure 3.4-27. This led to an increase in the peak stress to 174 ksi, in excellent agreement with the MARC result (which is calculated at an element integration point somewhat below the surface). The increase in computer time was only 7 percent, i.e., from 890 to 952 central processing unit (CPU) seconds. By comparison the MARC analysis required over 2700 CPU seconds to obtain equivalent results.

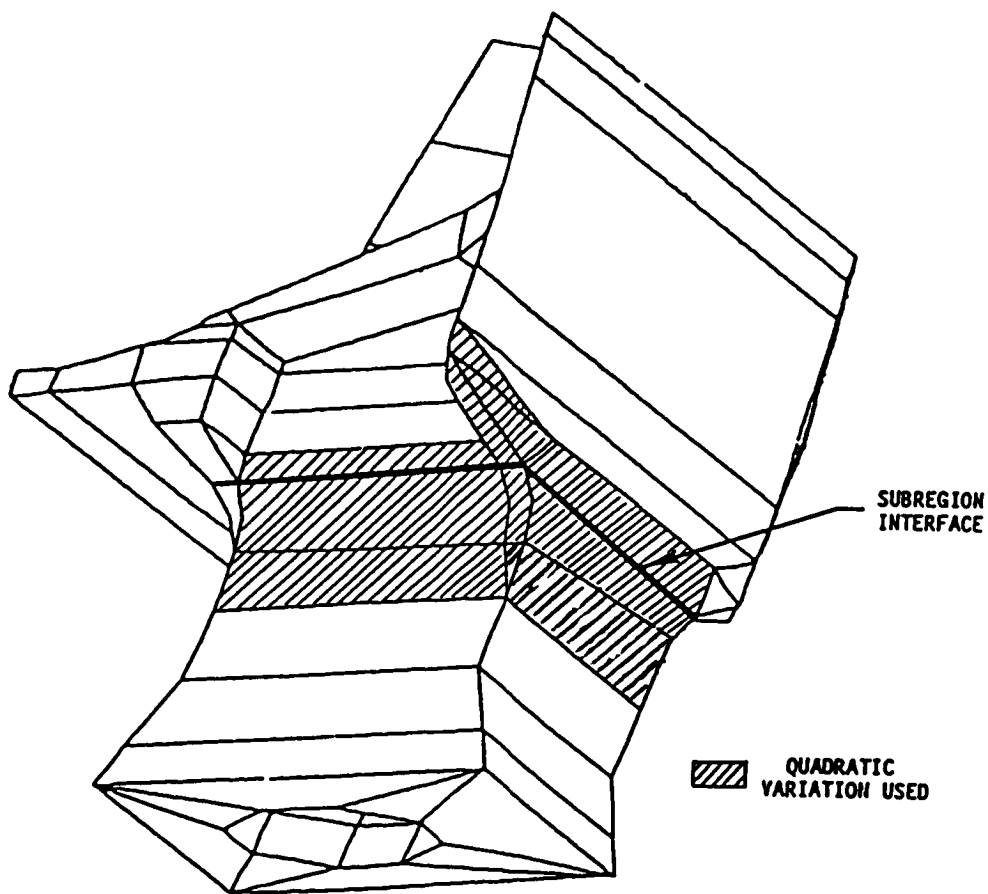


Figure 3.4-27 Extent of Quadratic Variation Used in BEST3D Turbine Blade Analysis

### 3.4.6 List of Symbols

#### List of Symbols Referenced Within Section 3.4

<u>Symbol</u>	<u>Description</u>	<u>Page</u>
$x_j$	Cartesian coordinates	132
$\dot{\sigma}_{ij}^0$	Initial stress rate	133
$\lambda, \mu$	Lame constants	133
$u_j$	Displacement rate	133
$\delta_{ij}$	Kronecker delta	133
$E$	Young's modulus	146
$\alpha$	Coefficient of thermal expansion	133
$T$	Temperature	131
$f$	Body forces loading	131
$S$	Boundary of body to be analyzed	131
$\xi$	Point on boundary $S$	132
$x$	Integration point	132
$y_i$	$= x_j - j$	132
$r$	$= y$	132
$V$	Interior of body to be analyzed	131
$G_{ij}$	Kelvin solution	131
$T_{ijk}$	Stresses derived from $G_{ij}$	131
$F_{ij}$	Tractions derived from $T_{ijk}$ and surface normal	131
$C_{ij}$	$1/2 \delta_{ij}$ if $S$ is smooth at $j$ ; otherwise depends on surface geometry at	131

List of Symbols  
Referenced Within Section 3.4 (continued)

<u>Symbol</u>	<u>Description</u>	<u>Page</u>
$t_j$	Tractions	131
$\sigma_{jk}$	Stress rate	131
$D_{ijk}$ $S_{ijk}$ $E_{ipjk}$	Higher order kernels derived from $G_{ij}$ by differentiation and use of Hooke's Law	131
$\underline{\dot{x}}$	Vector of all unknown freedoms (displacements and tractions)	134
$\underline{\dot{y}}$	Vector of all known freedoms (displacements and tractions)	134
$\rho$	Mass density	143
$\omega$	Frequency	143

### 3.4.7 References

1. C. A. Brebbia, J. C. Telles and L. C. Wrobel, Boundary Element Technique, Springer-Verlag, 1984.
2. P. K. Banerjee and S. Mukherjee (ed.), Developments in Boundary Element Methods, Elsevier Applied Science Publishers, 1984.
3. R. Perucchio and A. R. Ingraffea, "An Integrated Boundary Element Analysis System with Interactive Computer Graphics for Three-Dimensional Linear-Elastic Fracture Mechanics," Computers and Structures, Vol. 20, Nos. 1-3, 1985, pp. 157-171.
4. T. A. Cruse and R. B. Wilson, "Boundary-Integral Equation Methods for Elastic Fracture Mechanics Analysis," AFOSR-TR-78-0355, 1978.
5. F. J. Rizzo, D. J. Shippy and M. Rezayat, "A Boundary Integral Equation Method for Radiation and Scattering of Elastic Waves in Three Dimensions," Int. J. Num. Meth. Eng., 21, 1985, pp. 115-129.
6. D. Nardini and C. A. Brebbia, "A New Approach to Free Vibration Analysis Using Boundary Elements," Proceedings of Fourth International Seminar on Boundary Element Methods in Engineering, Springer-Verlag, 1982, pp. 312-326.
7. Y. P. Chiu, "On the Stress Field Due to Initial Strains in a Cuboid Surrounded by an Infinite Elastic Space," Transactions of the ASME, JAM, 44, 1977, Dec. 1977, pp. 588-594.
8. R. B. Wilson and T. A. Cruse, "Efficient Implementation of Anisotropic Three-dimensional Boundary Integral Equation Stress Analysis," Int. J. Num. Meth. Eng., 12, 1978, pp. 1383-1397.
9. D. M. Barnett, "The Precise Evaluation of Derivatives of the Anisotropic Elastic Green's Functions," Phys. Stat. Sol. (b), 49, 1972, pp. 741-748.
10. Y. C. Pan and T. W. Chou, "Point Force Solution for an Infinite Transversely Isotropic Solid," JAM, 43, 1976, pp. 608-612.
11. A. H. Stroud and D. Secrest, Gaussian Quadrature Formulas, Prentice Hall, New York, 1966.
12. P. A. Domas, et al, "Benchmark Notch Test for Life Prediction," NASA CR-165571, June 1982.

DISTRIBUTION LIST FOR CONTRACTOR REPORT  
 NASA CR 175060  
 3-D INELASTIC ANALYSIS METHODS FOR HOT SECTION COMPONENTS (BASE PROGRAM)  
 SECOND ANNUAL STATUS REPORT  
 CONTRACT NAS 3-23697

	<u>Mail Stop</u>	<u>Copies</u>
NASA Lewis Research Center		
21000 Brookpark Road		
Cleveland, OH 44135		
Attn: Contracting Officer	500-312	1
Technical Report Control Officer	5-5	1
Technology Utilization Office	3-16	1
AFSC Liaison Office	501-3	1
Structures Division Contract File	49-7	2
Library	60-3	1
L. Berke	49-7	1
R. H. Johns	49-8	1
D. A. Hopkins	49-8	1
C. C. Chamis	49-8	4
M. S. Hirschbein	49-8	1
L. J. Kiraly	23-2	1
G. R. Halford	49-7	1
D. J. Gauntner	49-8	1
A. Kaufman	49-8	1
R. C. Bill	49-7	1
D. Spera	49-8	1
D. E. Sokolowski	49-7	1
National Aeronautics & Space Administration		
Washington, DC 20546		
Attn: NHS-22/Library		1
RTM-6/M. A. Greenfield		1
NASA-Ames Research Center		
Moffett Field, CA 94035		
Attn: Library	202-3	1
NASA-Goddard Space Flight Center		
Greenbelt, MD 20771		
Attn: 252/Library		1
NASA-John F. Kennedy Space Center		
Kennedy Space Center, FL 32931		
Attn: Library	AD-CSO-1	1
NASA-Langley Research Center		
Hampton, VA 23665		
Attn: Library	185	1
M. F. Card	244	1
J. Starnes		1

	<u>Mail Stop</u>	<u>Copies</u>
NASA-Lyndon B. Johnson Space Center Houston, TX 77001 Attn: JM6/Library		1
NASA-George C. Marshall Space Flight Center Marshall Space Flight Center, AL 35812 Attn: AS61/Library		1
L. Kiefling		1
R. Ryan		1
Jet Propulsion Laboratory 4800 Oak Grove Drive Pasadena, CA 91103 Attn: Library		1
B. Wada		1
NASA S&T Information Facility P. O. Box 8757 Baltimore-Washington Int. Airport, MD 21240 Attn: Acquisition Division		10
Air Force Aeronautical Propulsion Laboratory Wright Patterson AFB, OH 45433 Attn: Z. Gershon		1
Air Force Systems Command Aeronautical Systems Division Wright-Patterson AFB, OH 45433 Attn: Library		1
C. W. Cowie		1
R. J. Hill		1
Aerospace Corporation 2400 E. El Segundo Blvd. Los Angeles, CA 90045 Attn: Library-Documents		1
Air Force Office of Scientific Research Washington, DC 20333 Attn: A. K. Amos		1
Department of the Army U.S. Army Material Command Washington, DC 20315 Attn: AMCRD-RC		1
U.S. Army Ballistics Research Laboratory Aberdeen Proving Ground, MD 21005 Attn: Dr. Donald F. Haskell	DRXBR-BM	1

	<u>Mail Stop</u>	<u>Copies</u>
Mechanics Research Laboratory Army Materials & Mechanics Research Center Watertown, MA 02172 Attn: Dr. E. M. Lenoë		1
U.S. Army Missile Command Redstone Scientific Information Center Redstone Arsenal, AL 35808 Attn: Document Section		1
Commanding Officer U.S. Army Research Office (Durham) Box CM, Duke Station Durham, NC 27706 Attn: Library		1
Bureau of Naval Weapons Department of Navy Washington, DC 20360 Attn: RRRE-6		1
Commander U.S. Naval Ordnance Laboratory White Oak Silver Springs, MD 20910 Attn: Library		1
Director, Code 6180 U.S. Naval Research Laboratory Washington, DC 20390 Attn: Library		1
Denver Federal Center U.S. Bureau of Reclamation P. O. Box 25007 Denver, CO 80225 Attn: P. M. Lorenz		1
Naval Air Propulsion Test Center Aeronautical Engine Department Trenton, NJ 08628 Attn: Mr. James Salvino		1
Federal Aviation Administration Code ANE-214, Propulsion Section 12 New England Executive Park Burlington, MA 01803 Attn: Mr. Robert Berman		1

	<u>Mail Stop</u>	<u>Copies</u>
Federal Aviation Administration DOT Office of Aviation Safety, FOB 10A 800 Independence Ave., S.W. Washington, DC 20591 Attn: Mr. John H. Enders		1
FAA, ARD-520 2100 2nd Street, S.W. Washington, DC 20591 Attn: Commander John J. Shea		1
National Transportation Safety Board 800 Independence Ave., S.W. Washington, DC 20594 Attn: Mr. Edward P. Wizniak	TE-20	1
Northwestern University Dept. of Civil Engineering Evanston, IL 60201 Attn: T. Belytschco		1
Rockwell International Corporation Los Angeles International Airport Los Angeles, CA 90009 Attn: Mr. Joseph Gausselin	D422/402 AB71	1
Rensselaer Polytechnic Institute Troy, NY 12181 Attn: R. Loewy E. Kreml		1 1
Cleveland State University Department of Civil Engineering Cleveland, OH 44115 Attn: Dr. P. Bellini		1
M. I. T. Cambridge, MA 02139 Attn: K. Bathe J. Mar E. A. Witmer T. H. H. Pian		1 1 1 1
University of Illinois at Chicago Circle Department of Materials Engineering Box 4348 Chicago, IL 60680 Attn: Dr. Robert L. Spilker		1

	<u>Mail Stop</u>	<u>Copies</u>
Allison Gas Turbine Division General Motors Corporation Speed Code T3, Box 894 Indianapolis, IN 46206 Attn: Mr. William Springer Mr. L. Snyder		1 1
General Motors Corporation Warren, MI 48090 Attn: R. J. Trippet		1
Arthur D. Little Acorn Park Cambridge, MA 02140 Attn: P. D. Hilton		1
AVCO Lycoming Division 550 South Main Street Stratford, CT 06497 Attn: Mr. Herbert Kaehler		
Beech Aircraft Corporation, Plant 1 Wichita, KA 67201 Attn: Mr. M. K. O'Connor		1
Bell Aerospace P. O. Box 1 Buffalo, NY 14240 Attn: R. A. Gallatly S. Gellin		1 1
Boeing Aerospace Company Impact Mechanics Lab P. O. Box 3999 Seattle, WA 98124 Attn: Dr. R. J. Bristow		1
Boeing Commercial Airplane Company P. O. Box 3707 Seattle, WA 98124 Attn: Dr. Ralph B. McCormick		1
Boeing Commercial Airplane Company P. O. Box 3707 Seattle, WA 98124 Attn: Dr. David T. Powell	73-01	1

	<u>Mail Stop</u>	<u>Copies</u>
Boeing Commercial Airplane Company P. O. Box 3707 Seattle, WA 98124 Attn: Dr. John H. Gerstle Mr. C. F. Tiffany		1 1
McDonnell Douglas Aircraft Corporation P. O. Box 516 Lambert Field, MO 63166 Attn: Library		1
Douglas Aircraft Company 3855 Lakewood Blvd. Long Beach, CA 90846 Attn: Mr. M. A. O'Connor, Jr.	36-41	1
Garrett AiResearch Manufacturing Co. 111 S. 34th Street P. O. Box 5217 Attn: L. A. Matsch		1
General Dynamics P. O. Box 748 Fort Worth, TX 76101 Attn: Library		1
General Dynamics/Convair Aerospace P. O. Box 1128 San Diego, CA 92112 Attn: Library		1
General Electric Company Aircraft Engine Business Group Cincinnati, OH 45215 Attn: Dr. L. Beitch Dr. M. Roberts Dr. R. L. McKnight	K221 K221 K221	1 1 1
General Electric Company Aircraft Engine Group Lynn, MA 01902 Attn: Mr. Herbert Garten		1
Grumman Aircraft Engineering Corp. Bethpage, Long Island, NY 11714 Attn: Library H. A. Armen		1 1

	<u>Mail Stop</u>	<u>Copies</u>
IIT Research Institute Technology Center Chicago, IL 60616 Attn: Library		1
Lockheed California Company P. O. Box 551 Dept. 73-31, Bldg. 90, PL. A-1 Burbank, CA 91520 Attn: Mr. D. T. Pland		1
Lockheed California Company P. O. Box 551 Dept. 73-31, Bldg. 90, PL. A-1 Burbank, CA 91520 Attn: Mr. Jack E. Wignot		1
Northrop Space Laboratories 3401 West Broadway Hawthorne, CA 90250 Attn: Library		1
North American Rockwell, Inc. Rocketdyne Division 6633 Canoga Avenue Canoga Park, CA 91304 Attn: K. R. Rajagopal F. Nitz J. F. Newell		1 1 1
North American Rockwell, Inc. Space & Information Systems Division 12214 Lakewood Blvd. Downey, CA 90241 Attn: Library		1
Norton Company Industrial Ceramics Division Armored & Spectramic Products Worcester, MA 01606 Attn: Mr. George E. Buron		1
Norton Company Industrial Ceramics Division 1 New Bond Street Worcester, MA 01606 Attn: Mr. Paul B. Gardner		1

	<u>Mail Stop</u>	<u>Copies</u>
Solar Turbine Inc. P. O. Box 80966 San Diego, CA 92138 Attn: G. L. Padgett		1
Southwest Research Institute 6220 Culebra Road San Antonio, TX 78284 Attn: T. A. Cruse		1
Lockheed Palo Alto Research Labs Palo Alto, CA 94304 Attn: D. Bushnell R. F. Hurtung		1 1
Lockheed Missiles and Space Company Huntsville Research & Engineering Center P. O. Box 1103 Huntsville, AL 18908 Attn: H. B. Shirley W. Armstrong		1 1
MacNeal-Schwendler Corporation 7442 North Figueroa Street Los Angeles, CA 90041 Attn: R. H. MacNeal		1
MARC Analysis Research Corporation 260 Sheridan Avenue, Suite 314 Palo Alto, CA 94306 Attn: P. V. Marcel		1
United Technologies Research Center East Hartford, CT 01608 Attn: Dr. A. Dennis		1
Georgia Institute of Technology School of Civil Engineering Atlanta, GA 30332 Attn: S. N. Atluri		1
Georgia Institute of Technology 225 North Avenue Atlanta, GA 30332 Attn: G. J. Semetsis R. L. Calson		1 1

	<u>Mail Stop</u>	<u>Copies</u>
United Aircraft Corporation Pratt & Whitney Group Government Products Division P. O. Box B2691 West Palm Beach, FL 33402 Attn: Library		1
R. A. Marmol		1
United Aircraft Corporation Pratt & Whitney Aircraft Group 400 Main Street East Hartford, CT 06108 Attn: Library		1
E. S. Todd		1
United Aircraft Corporation Hamilton Standard Division Windsor Locks, CT 06096 Attn: Dr. R. A. Cornell		1
Aeronautical Research Association of Princeton, Inc. P. O. Box 2229 Princeton, NJ 08540 Attn: Dr. Thomas McDonough		1
Republic Aviation Fairchild Hiller Corporation Farmington, Long Island, NY Attn: Library		1
Rohr Industries Foot of H Street Chula Vista, CA 92010 Attn: Mr. John Meaney		1
TWA, Inc. Kansas City International Airport P. O. Box 20126 Kansas City, MO 64195 Attn: Mr. John J. Morelli		1
State University of New York at Buffalo Dept. of Civil Engineering Buffalo, NY 14214 Attn: R. Shaw		1

	<u>Mail Stop</u>	<u>Copies</u>
University of Arizona College of Engineering Tucson, AZ 87521 Attn: H. Kamel P. H. Wirsching		1 1
University of California Department of Civil Engineering Berkeley, CA 94720 Attn: E. Wilson		1
University of Kansas School of Engineering Lawrence, KS 66045 Attn: R. H. Dodds		1
University of Texas at Austin Dept. of Aerospace Engineering & Engineering Mechanics Austin, TX 78712 Attn: J. T. Oden		1
Westinghouse R&D Center 1310 Beulah Road Pittsburgh, PA 15235 Attn: N. E. Dowling		1
Westinghouse Advanced Energy Systems Div. Waltz Mill P. O. Box 158 Madison, PA 15663 Attn: P. T. Falk		1

1. REPORT NO. NASA CR-175060	2. GOVERNMENT AGENCY	3. RECIPIENT'S CATALOG NO.
4. TITLE AND SUBTITLE 3-D INELASTIC ANALYSIS METHODS FOR HOT SECTION COMPONENTS (BASE PROGRAM)	5. REPORT DATE February 1986	6. PERFORMING ORG. CODE
	8. PERFORMING ORG. REPT. NO. PWA-5940-36	
7. AUTHOR(S) R. B. Wilson, M. J. Bak, S. Nakazawa and P. K. Banerjee	9. PERFORMING ORG. NAME AND ADDRESS UNITED TECHNOLOGIES CORPORATION Pratt & Whitney, Engineering Division 400 Main St., East Hartford, CT 06108	10. WORK UNIT NO.
12. SPONSORING AGENCY NAME AND ADDRESS National Aeronautics and Space Administration Lewis Research Center Project Manager, C. C. Chamis, MS 49-6 21000 Brookpark Road, Cleveland, OH 44135	11. CONTRACT OR GRANT NO. NAS3-23697	13. TYPE REPT./PERIOD COVERED Second Annual Status Report
	14. SPONSORING AGENCY CODE RTOP 533-04-1A	
15. SUPPLEMENTARY NOTES		

~~16. ABSTRACT~~

eps

A 3-D Inelastic Analysis Methods program is described. This program consists of a series of new computer codes embodying a progression of mathematical models (mechanics of materials, special finite element, boundary element) for streamlined analysis of: (1) combustor liners, (2) turbine blades, and (3) turbine vanes. These models address the effects of high temperatures and thermal/mechanical loadings on the local (stress/strain) and global (dynamics, buckling) structural behavior of the three selected components. Three computer codes, referred to as MOMM (Mechanics of Materials Model), MHOST (MARC-Hot Section Technology), and BEST (Boundary Element Stress Technology), have been developed and are briefly described in this report.

*QABA Author*

17. KEY WORDS (SUGGESTED BY AUTHOR(S)) -D Inelastic Analysis, Finite Elements, Boundary Elements, High Temperature, Creep, Vibration, Buckling, Solution Methods, Constitutive Modeling	18. DISTRIBUTION STATEMENT Unclassified Unlimited		
19. SECURITY CLASS THIS (REPT) Unclassified	20. SECURITY CLASS THIS (PAGE) Unclassified	21. NO. PGS 194	22. PRICE *

\* For sale by the National Technical Information Service, Springfield, VA 22161